Student thesis series INES nr 370

Snow and sea ice temperature profiles from satellite data and ice mass balance buoys

Isabella Grönfeldt

2015
Department of
Physical Geography and Ecosystem Science
Lund University
Sölvegatan 12
S-223 62 Lund
Sweden

Isabella Grönfeldt (2015). ***Snow and sea ice temperature profiles from satellite data and ice mass balance buoys***
Master degree thesis, 30 credits in *Physical Geography & Ecosystems Analysis*
Department of Physical Geography and Ecosystem Science, Lund University

Level: Master of Science (MSc)

Course duration: *January* 2015 until *June* 2015

Disclaimer

Snow and sea ice temperature profiles from satellite data and ice mass balance buoys

---

Isabella Grönfeldt

Master thesis, 30 credits, in *Physical Geography & Ecosystems Analysis*

Paul Miller
Department of Physical Geography and Ecosystem Science, Lund University

Gorm Dybkjær
Climate and Arctic, Danish Meteorological Institute

Leif Toudal Pedersen
Climate and Arctic, Danish Meteorological Institute

Rasmus Tonboe
Climate and Arctic, Danish Meteorological Institute

Exam committee:
Harry Lankreijer
Department of Physical Geography and Ecosystem Science, Lund University
Niklas Ohlén
Department of Physical Geography and Ecosystem Science, Lund University

-This page has intentionally been left blank.-

Abstract

The sea ice covers approximately 5% of the Earth's surface at any given time and it plays an important role in the polar climate system affecting the heat, mass and momentum exchange between the atmosphere and the ocean. The snow cover on top of the sea ice affects its insulating and reflective properties and thus key figures in the climate system feedback loop.

Sea ice and snow is of significant importance for our global climate system. However, it is difficult to effectively and accurately access data relating to snow and sea ice properties in the vast and remote Arctic region, especially during the winter, and snow is poorly constrained in current climate models. Improved information on snow and sea ice properties and thermodynamics from satellite observations could give valuable information in the process of validating, optimizing and improving these sea ice models and thereby the future predictions of sea ice growth and related climate variables.

This project examines the possibility of deriving the temperature profile through the snow and ice layers, from the surface down to 0.5 m into the ice, from a combination of available satellite data. Satellite data used are thermal infrared (TIR) and microwave radiation at different wavelengths and polarisations. The satellite data are compared with coincident data from ice mass balance buoys (IMB) and numerical weather prediction (NWP) data. This combined dataset are analysed for possible and theoretically derived relationships between the satellite measurements and different snow and ice parameters.

Different empirical models are used in this study to derive the mean snow temperature, snow density and snow and ice thickness, with various degree of success. It is clear that more advanced models are needed to accurately predict the observed variations of the snow and ice parameters. From the analysis it is clear that the satellite channels of lower frequencies are able to retrieve temperature measurements from deeper levels in the snow and ice than the higher frequencies. It is also clear that the satellite sensors are sensitive to changes in snow emissivity, associated with melting processes initiated by surface air temperatures around the freezing point, as the penetration depth is significantly decreased.

The models derived in the multiple regression analysis, performed on one of the four IMB buoys available, show a higher level of confidence for the deeper levels in the sea ice. When the models are tested on the remaining three IMB buoys the correlation for the lower levels in the sea ice are stronger. The comparisons between measured and theoretically derived temperatures show a generally strong correlation with R^2-values ranging from 0.43 to 0.90. It is evident that the models without TIR are superior to those including TIR measurements. The differences in correlation between the IMB buoys indicate a spatial dependency, as well as a strong dependency on differences in snow and ice thickness. The models derived in this study are based on conditions with relatively thick snow and ice covers. Further studies would need to be conducted in order to improve and generalize the models derived in this project, in order to implement the empirical models in operating, global sea ice models.

-This page has intentionally been left blank.-

Table of Contents

1. Introduction 1
2. Background 4
   2.1. The Arctic 4
      2.1.1. Oceanography 5
      2.1.2. Meteorology 6
   2.2. Sea ice and snow 7
   2.3. Satellite remote sensing 10
3. Data and Methods 11
   3.1. Ice mass balance (IMB) buoys 11
   3.2. Numerical weather prediction (NWP) 14
   3.3. Satellite data 14
      3.3.1. AMSR-2 14
      3.3.2. SMOS 14
      3.3.3. TIR 15
   3.4. Match-Up dataset 15
   3.5. Data analysis and empirical models 15
      3.5.1. Emissivity, spectral gradient ration and polarization ratio 15
      3.5.2. Snow density and thickness 16
      3.5.3. Snow-ice interface temperature 17
      3.5.4. Ice thickness 17
   3.6. Multiple regression analysis 18
      3.6.1. Control 18
4. Results and Discussion 19
   4.1. Air-snow interface 20
      4.1.1. Air temperature and NWP 20
      4.1.2. AMSR2 89 GHz 22
      4.1.3. TIR 24
   4.2. Snow layer 25
      4.2.1. Snow layer temperature 25
      4.2.2. Emissivity 26
      4.2.3. Snow layer thickness 28
      4.2.4. Snow layer density and density weighted thickness 30
   4.3. Snow-ice interface 32
   4.4. Ice layer 34

4.4.1. Ice thickness and growth 34
4.4.2. Theoretical ice thickness 35
4.5. Ice-water interface 37
4.6. Multiple regression analysis 37
4.7. Model comparison 40
5. Summary and Conclusions 47
Acknowledgements 50
6. References 51
Appendix A 56
Appendix B 60
Appendix C 63
Appendix D 66
Appendix E 68
Appendix F 69

1. Introduction

The sea ice covers approximately 5% of the Earth's surface at any given time. In consequence it plays a vital role in the polar climate system as it affects the heat, mass and momentum exchange between the atmosphere and the ocean. A snow cover on top of the sea ice enhances the effects due to its insulating and reflective properties. The snow has a higher albedo than the bare sea ice, limiting the absorbed shortwave radiation. The snow also has a lower thermal conductivity, about an order of a magnitude lower than that of sea ice. It therefore works as an insulator between the ocean and the relatively cold atmosphere, restricting the bottom ice growth (Figure 1) (Massom et al., 2001; Powell et al., 2006; Lecomte et al., 2014).

Over the recent decades there has been a loss of sea ice in the Arctic region, both extent and thickness. The biggest rate of change can be seen during the summer months, but the changes are evident all year round (Solomon et al., 2007). The decrease in sea ice causes rising air temperatures not just over the ice but hundreds of kilometres inland in the perimeter of the Arctic Ocean (Bitz, 2013). This in turn, results in longer sea ice melting periods, more open water areas, additional heating through the albedo feedback process and melting of the permafrost. The decrease of sea ice changes the way of life for humans, animals and plants and further increases the Arctic amplification in the process of global warming (Solomon et al., 2007; Bitz, 2013).

The issue of global warming motivates many to understand and model the physics of the sea ice, such as Toudal Pedersen (2004), Tedesco and Kim (2006), Powel et al. (2006), (Bitz, 2009) and Lecomte et al. (2015). At a recent (spring 2015) presentation, at the Danish Meteorological Institute, Professor Jinro Ukita from Niigata University, Japan, was talking about the teleconnections between the loss of sea ice in the Arctic and the climate at mid-latitudes. The albedo feedback mechanism is a powerful mechanism involving sea ice, but Professor Jinro Ukita pointed at an additional feedback mechanism involving sea ice which is enhancing the polar cell thus exchanging heat between mid-latitudes and the Arctic. In his model simulations professor Ukita combined the albedo feedback mechanism and the effects of the enhanced polar cell, to predict future climate change and future rate of sea ice decline. The consequences of the heating at mid-latitudes were evident from northern Europe across Siberia to Japan (Ukita, 2015).

The sea ice is of significant importance for our climate system, and for the thermodynamics of sea ice snow is important (Markus et al., 2006b; Tonboe, 2010). However it is difficult to effectively and accurately access data relating to the snow and sea ice in the vast and remote Arctic region, especially during the winter. There are several different observation methods available; field studies and in situ observations from ships, airplanes and weather stations, movement of drift buoys and satellite remote sensing (Solomon et al., 2007). Satellite measurements are the most convenient observation method, since the satellites are able to cover large areas. However, at present, satellite measurements are not as accurate as actual field measurements and must be constantly confirmed by field data in order to improve. Such field studies are conducted aboard the Norwegian research vessel RV Lance. During a two week period in 2014 the ship performed measurements in the Barents Sea, covering an area of 6000 km^2, to validate SMOS and Cryo-Sat data (Drusch, 2014). At present, in 2015, the ship is frozen into the Arctic sea ice in order to work as a floating research platform for the Norwegian young sea ICE cruise (N-ICE2015). From the slowly drifting platform it is possible to conduct measurements of the prevailing conditions in the ocean and atmosphere as

well as the state of the sea ice, in order to provide accurate data for improving future climate models (Norwegian Polar Institute, 2015).

Even though the Arctic Ocean is inaccessible and a lot of the snow and ice parameters are difficult to measure accurately, the extent of the sea ice cover has been measured continuously and successfully since the launch of the first satellites carrying passive microwave radiometers in 1979 (Willmes et al., 2014). The spatial distribution and the physical properties of the snow however, make accurate data retrieval of sea ice thickness and concentration difficult. The snow is constantly changing as an effect of wind stress and a range of metamorphism processes, which disturbs the signals received by the satellites (Massom et al., 2001; Andersen et al., 2007; Willmes et al., 2014). Furthermore the snow affects the physical parameters of the sea ice itself and thereby the depth to which microwave satellites can measure (Bitz, 2009)

Today snow parameters, such as temperature, layering, grain size, roughness, density and thickness, pose a difficulty to accurate data retrieval by satellites. As the insulating and reflective snow is a key factor in the radiation balance, these snow parameters are the primary sources of error when measuring sea ice thickness and concentration with satellites (Tonboe et al., 2011). Improved information on snow surface and snow-ice interface temperatures from satellite observations could give valuable information on vertical thermodynamics in the snow and ice. This, in turn, would assist in validating, optimizing and improving current sea ice models and thereby the future predictions of sea ice growth (Tonboe et al., 2011). Accurate and precise knowledge about the natural variations of the sea ice cover are critical to be able to represent it in global climate models. One of the main uncertainties in the predictions of future temperature increase is changes in the Arctic sea ice cover and thereby changes in the ice-albedo feedback mechanism (Laxon et al., 2003; Lecomte et al. 2015).

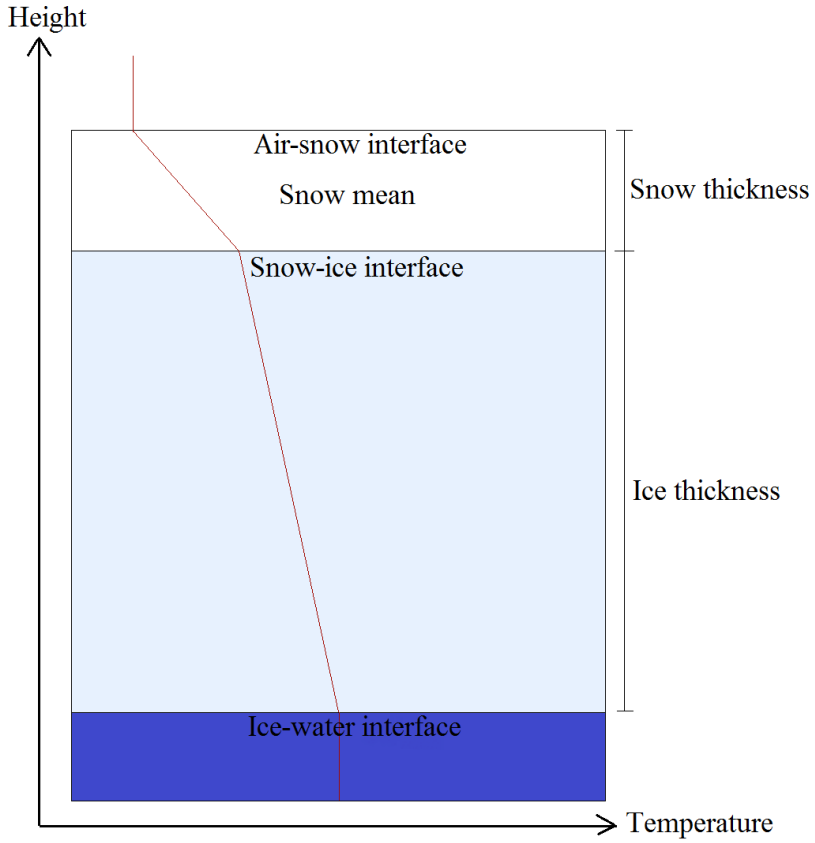

Figure 1. A conceptual model of the snow and ice layers, and the main focus points in this study, with an approximate temperature profile as a red line.

The objective of this project is to examine the possibility of deriving the temperature profile through the snow and ice layers (see Figure 1) from a combination of available satellite data, such as thermal infrared and microwave radiation at different wavelengths and polarisations. The satellite data will be compared with coincident data from ice mass balance buoys (IMB) and numerical weather prediction (NWP) data. This combined dataset will be analysed for possible and theoretically derived relationships between the satellite measurements and different snow and ice parameters. The snow and sea ice thermodynamics will be the main focus through this study.

A match-up dataset will be created; containing satellite, IMB and NWP data following the drift tracks of four IMBs northeast of Greenland during the winter period of 2012-2013, i.e. September-May as they travel south into the Fram Strait. The content of the dataset will be analysed with the goal of identifying the satellite observations best suited for retrieving the different snow parameters and sea ice thermodynamics. The surface, i.e. the air-snow interface, temperature will be studied as well as the snow cover: precipitation events, snow cover mean temperature, thickness, density and emissivity. The temperature and thickness of the sea ice cover will also be studied, at different depths. The accuracy of the satellite retrievals, of snow and ice parameters, compared to the IMB and NWP data will be discussed and the possibility of replacing climatological snow cover in sea ice models with satellite measurements will also be assessed. The final goal is to create empirical models, for one of the IMB buoys, able to reproduce the temperature profile through the snow and ice solely from satellite measurements. The accuracy and certainty of the models will be discussed as they are tested on the remaining three IMB buoys.

To be able to interpret the results of this study it is important to have some background knowledge about the study area, i.e. the Arctic region, the physics of sea ice and snow as well as the basics of satellite remote sensing. All of which are very complex and vast areas of knowledge. This master thesis provides a brief overview of the topics with focus on what is considered the key parameters for this particularly study. First of all the area of interest is presented and the main oceanographic and meteorological features are discussed, i.e. the ocean currents and dominating pressure systems. Some basics on sea ice and snow are presented, including growth, melt, distribution, thickness and heat flux. In terms of satellite remote sensing the very basics are presented and the concept of brightness temperature is discussed. The sensors and bands of radiation used in this study, i.e. passive thermal infrared and microwave sensors, are also presented.

Following the brief introduction to the background of the study comes the data description; presentation of the different data types that are combined into one large dataset, i.e. IMB, NWP and satellite data. The methodology is discussed and the steps and empirical models used in the process of validation and analysis of the dataset are presented. The result is divided according to the specified levels down through the snow and ice layers, see Figure 1. The surface parameters at the air-snow interface, the properties of the snow and the mean snow temperature, the snow-ice interface as well as the ice thickness and temperatures at different depths in the ice, i.e. 0.1, 0.3 and 0.5 m into the ice, are all discussed. After analyzing the measured properties and thermodynamics of the snow and ice layers it is possible to choose accurate variables for the multiple regression analysis, which along with the final control of the models are discussed at the end of this thesis.

2. Background

To be able to better appreciate and understand the results presented in this study it is important to have some background knowledge about the study area, i.e. the Arctic, sea ice and snow cover as well as the basics of satellite remote sensing.

2.1. The Arctic

The Arctic region is a vast and remote area, enclosing the North Pole. It consists mainly of a large ocean but also parts of the surrounding land masses. There are several different definitions regarding the Arctic; it is defined as the area above 66° 32' N, i.e. above the Arctic Circle, it is defined as the area north of the treeline and it is defined as the area where the average daily summer temperature does not exceed 283.15 K. Whichever way it is defined the Arctic is a unique region and the special conditions prevailing makes the large Arctic Ocean one of a kind (AMAP, 2012; NSIDC, 2015). This section will go through the general oceanographic and meteorological conditions for the entire Arctic region even though the main region of interest for this study is the area just north of Greenland and Fram Strait, see Figure 2.

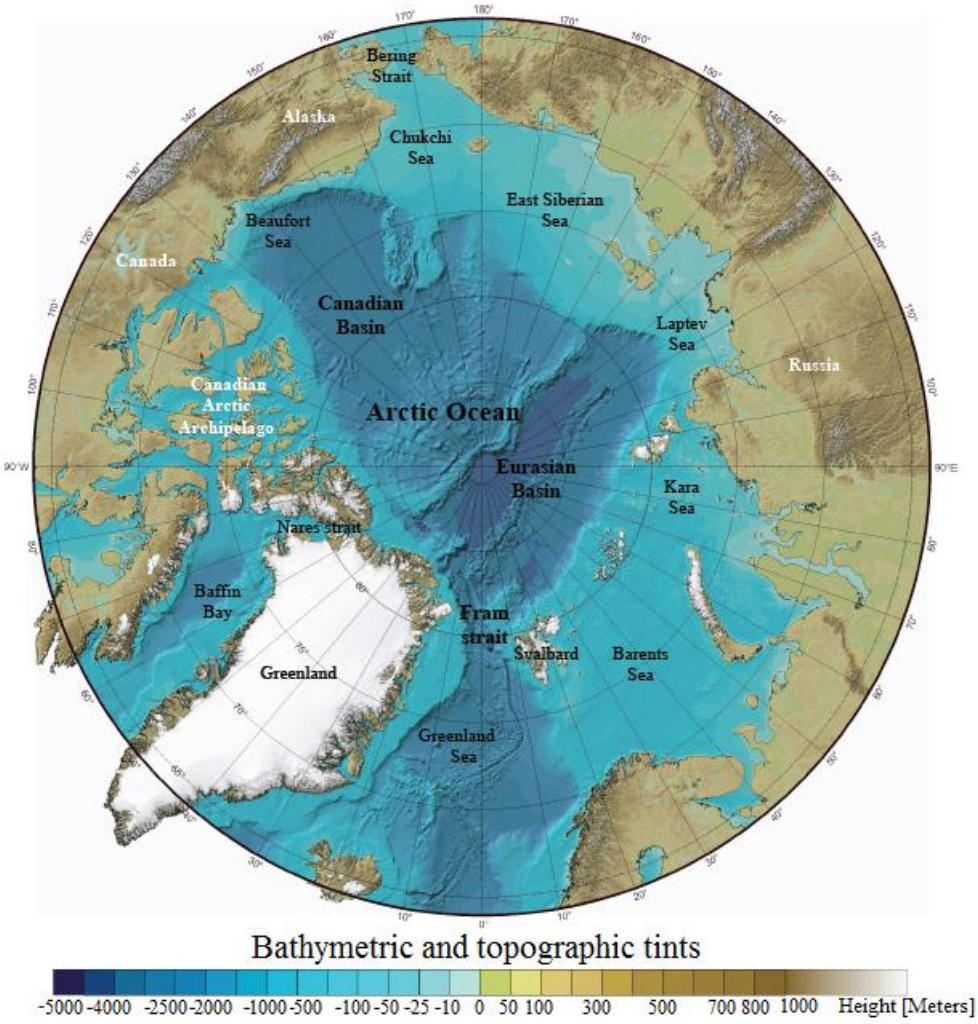

Figure 2. The International bathymetric chart of the Arctic Ocean. Source: IBCAO, 2008. Modified by Brandt Jensen, 2011.

2.1.1. Oceanography

The Arctic Ocean is a well closed off basin, by shallow shelf seas all along the Eurasian side, see Figure 2. The shallow seas limit the exchange between the Arctic Ocean and the surrounding oceans. The water can escape the Arctic Ocean through passages in the Canadian Archipelago, through the Barents Sea and through the Nares and Bering Straits. The main passage however, and that which accounts for most of the heat and water exchange for the Arctic Ocean, is the Fram Strait. Fram Strait is a deep water canal between Greenland and Svalbard, connecting the Arctic Ocean to the Atlantic Ocean. The strait is about 2600 m deep and 600 km wide (Wadhams, 2000).

The water transport in the Arctic Ocean is controlled by the wind driven surface currents, which in turn are dominated by the Beaufort Gyre and the Transpolar Drift Stream, see Figure 3. The Beaufort Gyre is an anticyclonic motion in the Arctic Ocean, slowly transporting water and ice around the basin. The Transpolar Drift Stream is the main transporter of ice and water out of the Arctic Ocean. The current is a cross-basin current, transporting water from the shallow continental shelves of Asia across the ocean towards Greenland. As parts of the Transpolar Drift Stream enter through Fram Strait the velocity increases and the current is renamed the East Greenland Current (Eicken, 2003). The cold and icy East Greenland Current is more or less delimited on the outside by branches of the North Atlantic Current moving up along the west side of Spitsbergen (Toudal Pedersen et al., 2001).

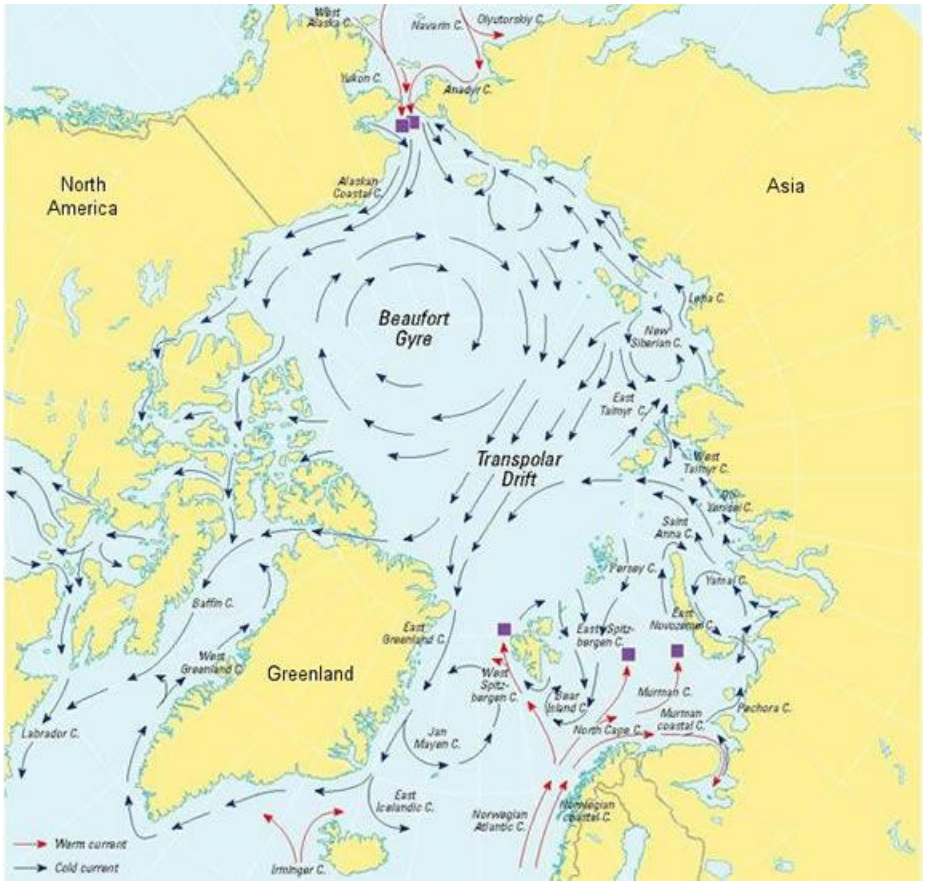

Figure 3. Arctic Ocean surface circulation, where blue arrows indicate cold polar surface water and red warmer Atlantic water. The square boxes show where the Atlantic water sinks and flows under the colder polar water (AMAP, 2008).

Relatively warm and salty water enters the Arctic Ocean through the Fram Strait as the West Spitsbergen Current as well as through the shallow Barents Sea and from the Pacific Ocean

through the Bering Strait. Large amounts of freshwater enter the ocean through river systems on the North American and Asian continents, creating layers of freshwater (Rudels et al., 1996). The different water masses accumulating in the Arctic Ocean create a very stratified water column and a strong halocline (Wadhams, 2000; Toudal Pedersen et al., 2001).

2.1.2. Meteorology

The energy balance of the Arctic is highly dependent on solar insolation. Due to the tilt of the Earth the seasonal variations in solar fluctuation are significant. The polar night results in extreme freezing conditions at the surface during winter, creating a steep temperature gradient between the surface and the relatively warm ocean beneath the insulating pack ice. The constant sunshine during spring and summer on the other hand contributes in large part to melting of the sea ice. The precipitation as well as the sunshine is sparse during winter in the central Arctic region. There is little evaporation from the sea except in cracks and leads in the pack ice and along the sea ice edge. The inner parts of the Arctic region are significantly dry and defined as being polar desert (NSIDC, 2015).

The atmospheric conditions of the Arctic region are controlled by large-scale, semi-permanent pressure systems. The pressure systems are especially prominent during the winter, see Figure 4. In the winter season the surface pressure situation is dominated by the Islandic Low, the Aleutian Low centred between North America and Asia, the relatively weak North American High, the strong Siberian High and the Beaufort High centred in the middle of the Arctic Ocean (NSIDC, 2015). The Beaufort High connects, depending on its strength, the North American High to the Siberian High and is sometimes referred to as the Arctic High. Together these pressure systems create strong surface pressure gradients, resulting in high wind speeds. The winds, which move along the isobars, generate an anticyclonic circulation around the Beaufort High and a cross basin motion from Siberia to Greenland, i.e. the Beaufort Gyre and the Transpolar Drift Stream (Eicken, 2003).

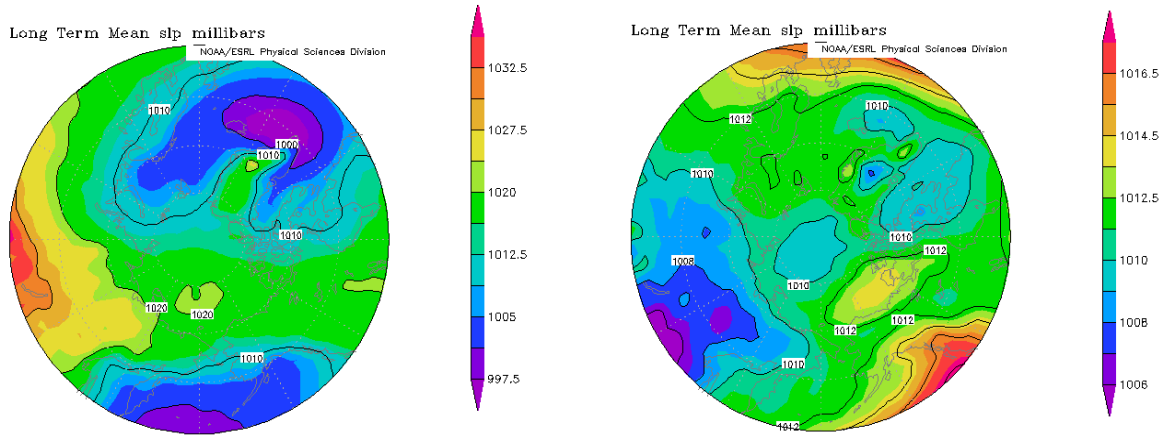

Figure 4. Mean sea level pressure situation in the Arctic region 1981-2010. To the left; mean sea level pressure December-February 1981-2010 and to the right mean sea level pressure for June-August 1981-2010 (NOAA, 2013).

The great ice mass on top of Greenland, stretching about 3000 m up into the sky, creates a local high pressure centre above the island. The vast land mass and accompanying high pressure system effectively blocks and redirects every passing cyclone and storm. The storms are forced to pass around the island instead of across it. The short lived cyclones and polar lows are frequent in the Greenland Sea, i.e. along the east coast of Greenland. The storms dominate the atmospheric conditions on shorter time scales as they transport heat, momentum

and moisture into the Arctic region (Toudal Pedersen et al., 2001). On longer time scale it is the semi-permanent pressure systems that controls the conditions in the Arctic, and atmospheric oscillations such as the North Atlantic and Arctic Oscillation. The North Atlantic and Arctic Oscillations are comparisons between the strength of the Azores High, at 45° mid-latitudes, and the strength of the Icelandic Low or the Beaufort High respectively. The oscillation can be either in a positive or negative phase and controls the strength of the Westerlies, i.e. the strong westerly winds that controls the storm trajectories as the low pressure systems travel across the Atlantic, and the level of cold/warm advection from/to the Arctic region. When the Arctic Oscillation is in a positive phase the Beaufort High is weakened, and this results in strong Westerlies. As a consequence of the strong westerly winds the cold arctic air is encircled and trapped in the Arctic. Conversely, when the Arctic oscillation is in a negative phase, the Beaufort High is strong, the Westerlies are weakened and cold arctic air leaks out to the surrounding continents. The positive or negative phases of the oscillations range on a time scale from weeks to decades (NSIDC, 2015).

2.2. Sea ice and snow

The sea ice covers approximately 5% of the Earth's surface at any given time (Lubin and Massom, 2006; Solomon et al., 2007). The sea ice is a powerful and sensitive indicator as well as modulator for the global climate system (Lubin and Massom, 2006). It controls the heat, momentum and gaseous exchange between the ocean and the atmosphere. The heat exchange via open water is twice that through thick sea ice (Sandven and Johannessen, 2006). The sea ice, and the snow on top of it, also has a much higher albedo than the open water, i.e. about 80% compared to 10-20% for open water. The snow and sea ice therefore play a major role in the global climate system through the ice albedo feedback mechanism. With increasing sea ice there is an increased amount of solar radiation reflected back into the atmosphere, instead of being absorbed by the ocean. The loss of radiation leads to lower surface temperatures and an increased rate of sea ice production (DMI, 2012). The sea ice also has a significant impact on the ocean circulation through brine rejection, i.e. a process where the salt is excluded from the forming ice crystals making the surrounding seawater saltier and denser, and through transport and input of freshwater. In the different stages of the sea ice lifecycle it binds, transports and releases brine and freshwater to the surrounding water masses creating convection in the ocean (Sandven and Johannessen, 2006).

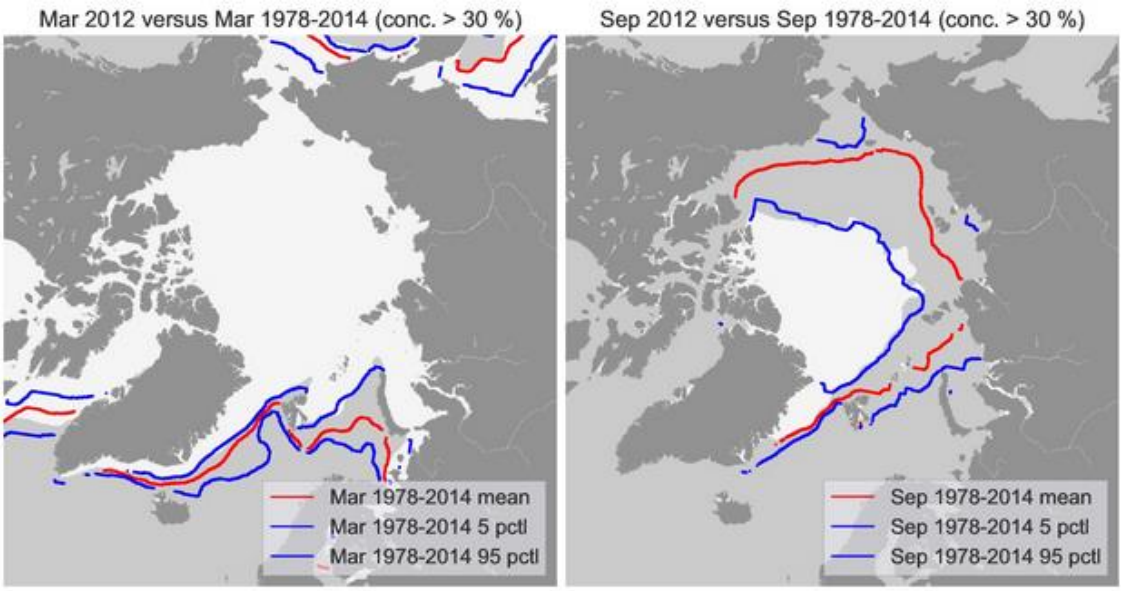

Figure 5. Maps showing the monthly mean sea ice extent (white), exceeding a concentration of 30%, in the Arctic during the maximum sea ice extent in March (left) and the minimum sea ice extent in September (right) 2012. The maps are additionally overlaid with the corresponding multi-year monthly mean of the period 1978-2014 as a red line, the blue lines are 5 and 95 percentiles (DMI, 2015).

This study focuses on the Northern Hemisphere and the Arctic region. During the annual sea ice extent maximum in March, see Figure 5, 5% of the ocean surface in the Northern Hemisphere is covered in sea ice (Lubin and Massom, 2006; Solomon et al., 2007). The inner parts of the Arctic Ocean as well as the Canadian Archipelago are annually covered in sea ice. Also the northern parts of the east coast of Greenland, where the sea ice is transported out of the Arctic through the Fram Strait, experiences an ice cover all year around. The shallower seas framing the North Pole, such as the Barents, Kara, Laptev, East Siberian and Chukchi Sea, are only ice covered during the winter season, see Figure 5 (DMI, 2012, NSIDC, 2015).

Sea ice is formed as the ocean, with a salinity of approximately 34 psu (practical salinity units), reaches a temperature of 271.29 K. The top most layer of the ocean starts to freeze, and step by step turns into solid ice. The amount of brine captured in the ice determines its thermal conductivity, since brine has a lower thermal conductivity than pure ice by a factor of four (Eicken, 2003). As the ice settles it may accumulate a snow cover, even though the precipitation in the Arctic is sparse. The snow cover has significantly stronger insulating properties than the bare ice, with an average conductivity of 0.2 $Wm^{-1}K^{-1}$ compared to 2 $Wm^{-1}K^{-1}$ for the sea ice. This means that 10 cm of snow is equivalent to 1 m of ice in terms of heat conductivity. For new freshly fallen snow the heat conductivity is even lower, and only 2 cm of snow is equivalent to 1 m of ice (Tonboe, 2010). The atmosphere is considerably colder than the ocean during winter in the Arctic and a snow cover on top of the ice can therefor lead to warmer temperatures in the ice and a steeper temperature gradient through the snow and ice layers (Eicken, 2003).

The snow has also a higher albedo than the bare ice, meaning it intensifies the albedo feedback mechanism discussed earlier. Depending on the water content of the snow it reflects more or less radiation. Newly fallen snow is often, depending on the weather conditions during the snowfall, very light and has a low density as it is full of air and has a clear snow crystal structure. This type of snow has a high reflectivity (Lubin and Massom, 2006). As the snow ages it changes through different geophysical processes; the snow increases in density

through crystal metamorphism in the snowpack, crystal settlement, melt and wind packing. The snow thickness is also reduced through sublimation, wind advection and snow-ice formation, which is more common in Antarctica (Pomeroy et al., 1998; Lubin and Massom, 2006).

The growth and melt rate of the sea ice is controlled by the heat exchange between the ocean and the atmosphere. The heat flux is controlled by the thermodynamic properties of the ice and snow layers such as the conductivity and also the thickness. The thinner the ice and/or snow layer the higher the rate of the sea ice growth. During the winter heat escapes the Arctic Ocean at a significant rate through thin ice and areas of open water, such as cracks, leads and polynyas (Lubin and Massom, 2006). The heat reenters the ocean as solar radiation and longwave radiation from the atmosphere during the summer time, and all year round heat convection in the atmosphere and in the ocean from lower latitudes (Ukita, 2015). A snow layer on top of the ice prolongs the freezing period and generally the melting of the snow cover, in the Arctic region, begins in June (Wadhams, 2000). However, as the melting snow creates ponds on the surface the albedo is significantly lowered and the melt ponds contribute to further melt the snow and ice. In the summer as much as 60% of the Arctic sea ice surface may be covered by melt ponds (Lubin and Massom, 2006).

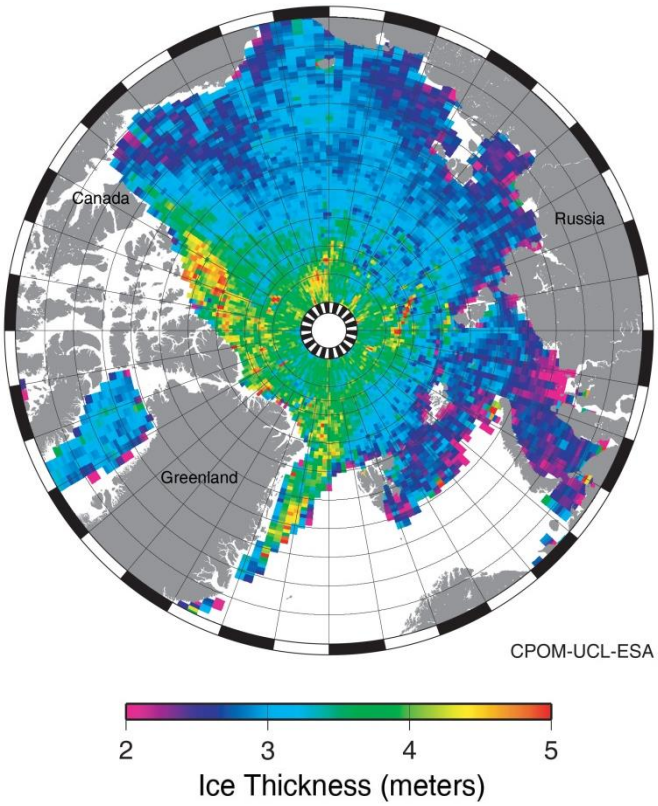

Figure 6. Arctic sea ice thickness January-February 2011, measured by the European Space Agency's (ESA) ice mission Cryosat-2. The data has been processed at the Centre for Polar Observation and Modelling (CPOM) at the University College London (UCL) (ESA, 2011; UCL, 2011).

The pack ice of the Arctic Ocean is never still, it is constantly moving and changing. The sea ice drifts and deforms in response to the synoptic-scale changes in wind, ocean currents, tidal forcing and internal stress (NSIDC, 2015). The forces acting on the ice can be convergent or divergent, i.e. creating ridges and ice floes piled on each other, or creating leads and openings in the ice. The ice transport in the Arctic Ocean is dominated by the already discussed

Beaufort Gyre and Transpolar Drift Stream (see Section 2.1). The Beaufort Gyre slowly transports the sea ice anticyclonically in the ocean. The Transpolar Drift Stream, which has a significantly higher velocity, transports the ice produced in the shallow seas along the Asian continent across the ocean and pushes it against the Canadian Archipelago and the northern coast of Greenland. The stacked ice mass north of Greenland accounts for the thickest ice in the Arctic Ocean, see Figure 6 (Haas, 2003).

2.3. Satellite remote sensing

The information in this section is exclusively from Lubin and Massom, 2006.

Satellite remote sensing is currently the most effective way of measuring the large scale changes of the sea ice variability in the Arctic Ocean. The satellite sensors orbiting the Earth are sensitive to radiation from different parts of the electromagnetic spectrum, such as the visible, infrared and microwave spectra. The radiation interacts with the emitting or reflecting surface and is measured by the sensor as an average intensity. The measured radiation is dependent on the surface and instrument characteristics, i.e. the surface roughness and topography as well as wavelength, polarization and incidence angle of the sensor. The energy intensity is converted into a brightness temperature, from which it is possible to derive information about the sea ice surface properties, such as roughness, emissivity and thereby the type of ice and its estimated thickness. To get the actual surface temperature, the brightness temperature has to be divided by the surface emissivity. The emissivity is a measurement of the radiation capacity of the snow layer, which is dependent on the microphysics of the snow, i.e. parameters such as snow density, grain size and snow thickness.

There are a number of different satellite sensors, both passive and active, measuring in all the bands of the electromagnetic spectrum. The focus for this section will be on the sensors specifically used in this study, that is passive thermal infrared and microwave radiometer sensors. Passive sensors receive emitted (or reflected) radiation from the Earth's surface within the specific bands of radiation. The different wavelengths penetrate the sea ice surface to various depths, providing information from different vertical locations in the snow and ice system. Lower frequencies penetrate the surface more than higher frequencies. The thermal infrared radiation does not penetrate the surface more than a couple of mm, while the low frequency microwave radiation can penetrate deep into the ice layer.

Infrared and microwave radiation are constantly being emitted from the surface, day and night. However, the infrared radiation is sensitive to clouds and can't penetrate a cloudy sky. Microwave radiation has the ability and the advantage of moving through the clouds. Sensors operating in the microwave band of the electromagnetic spectrum can therefore operate regardless of the weather conditions and thereby provide an uninterrupted view of the measured surface. Even though the microwave sensors can penetrate clouds they are sensitive to water content in the atmosphere and the measured surface. With high amounts of water the penetration depth for the radiation will decrease. The penetration depth will also decrease for high air and surface temperatures, and conversely low temperatures result in deep radiation penetration.

3. Data and Methods

In this study several types of data sources are used and combined to get as precise measurements as possible, and to be able to perform an extensive and accurate analysis. Data measurements are assembled from drifting ice mass balance buoys, numerical weather predictions and different forms of satellite data. The data are then collocated to the temporal and spatial location of the buoy measurements and combined into one complete match-up dataset. The combined dataset will be analysed for possible and theoretically derived relationships between the satellite measurements and different snow and ice parameters. The methods and empirical models used will be presented in this chapter.

3.1. Ice mass balance (IMB) buoys

Ice mass balance (IMB) buoys (Figure 7) are a low-cost and effective way of measuring the sea ice heat flux, location and movement of the ice, the snow and ice thickness and potentially, with the use of new techniques, also additional information on air and water currents (Jackson et al., 2013). IMB buoys are presently the most suitable technique for monitoring the internal evolution of the snow and ice layers over a longer period of time (Jackson et al., 2013). In this study data from the Scottish Association for Marine Science (SAMS) IMB buoys are used. A SAMS IMB buoy consists of a long chain of sensors, one every 2 cm (Figure 8). The thermometer chain is connected by a cable to a logging controller and a battery power source in an enclosure stationed on the ice surface, see Figure 7. When deployed the chain of sensors is fastened to a pole of low conductivity material. The pole is lowered into a drilled hole in the sea ice, with one end of the chain sticking up above the snow layer (see Figure 9). The sensors can then register the temperature profile all through the snow and ice layers, including the air and water temperatures (Figure 8). For each sensor there is an additional heating element, making it possible for the sensor to temporarily heat its surroundings. This is done so that by registering the rate and level of temperature change the sensor is able to deduce what medium it is in. This way the interfaces, i.e. the air-snow, snow-ice and ice-water interfaces, can be determined with an accuracy of 2 cm. The registered results are regularly transmitted back to the receiver using Iridium satellites (SAMS, 2012).

Figure 7. A deployed IMB buoy on the Arctic sea ice. The buoy consists of a long chain of sensors (one the left hand side in the picture), one every 2 cm, with the ability to measure the temperature profile down through the snow and ice layers. The sensor chain is connected by a cable to a logging controller and a battery power source in an enclosure (yellow in picture) stationed on the ice surface (Dybkjær, 2015).

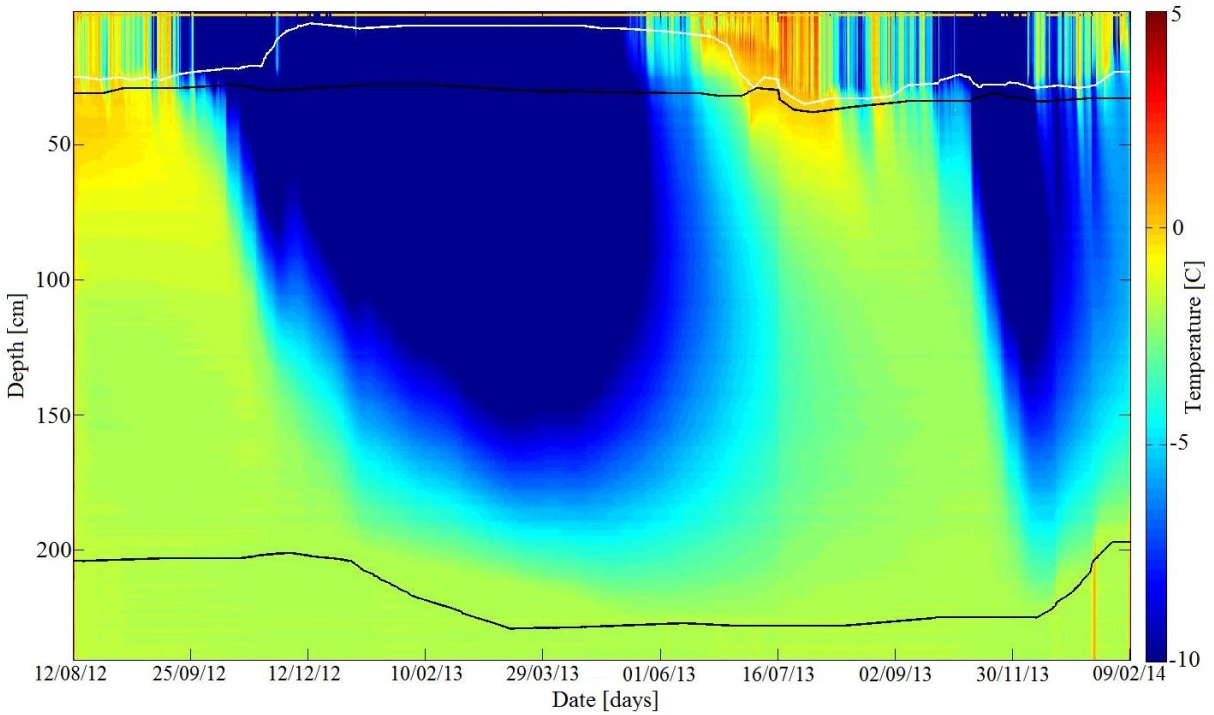

Figure 8. The measured temperature profile in degrees Celsius through the snow and ice layers over time, from one of the IMB buoys used in this study (buoy 3). Blue indicates low temperatures while red indicates high temperatures. The air-snow interface is marked by a white line and the snow-ice and ice-water interfaces are marked by black lines. The measuring period ranges over almost two winter periods, from the 12th of August 2012 until the 9th of February 2014 (DMI, 2015)

In August 2012 a total of 8 SAMS IMB buoys were deployed on multiyear ice north of Greenland (see Figure 7 and 10) by staff from the Danish Meteorological Institute (DMI). The buoys were deployed during the LOMROG-3 expedition with the Swedish icebreaker Oden as research platform, as part of the NAACOS project (Polarforskningssekretariatet, 2012; DTU, 2013). The buoys were to send back data continuously every 6h hours but due to different complications some of them sent data very sporadically or completely stopped transmitting for a period of time. There were large differences in the lifespan of the buoys, some transmitting for two full years while other only lasted a couple of months.

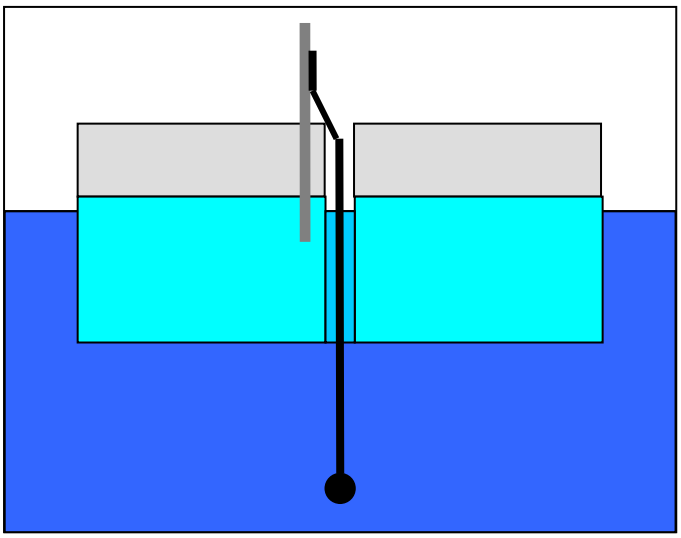

Figure 9. Sketch of a typical deployment for a SAMS IMB buoy (SAMS, 2012)

4 out of the 8 deployed buoys are chosen for this study, to have a manageable amount of data, see Figure 10 and Appendix A. The 4 buoys, numbered 3-6, are chosen based on continuity of the data, lifespan and risk of land contamination. The analysis and comparison of buoy and satellite data is simplified if the area considered is a homogenous area of ice, which requires the chosen area not to change too much within the specified time frame. A spatial limit has to be set at 80°N to avoid land contamination, ice divergence, i.e. open water inside the footprint of the satellite data which is a risk especially for the applied passive microwave data of lower frequencies and spatial resolution, and mixing of ice types which occurs at a high rate in Fram Strait. The focus in this study is on the winter period, which is defined as September-May, to avoid water contamination from melt ponds and atmospheric water vapour and initial melt processes that inhibits microwave penetration into the ice.

The obtained buoy dataset contains date, time, GPS position [latitude/longitude], measurements of air temperature [K], i.e. the median value of temperature sensor 1-5, estimated sensor number for the air-snow, snow-ice and ice-water interfaces, the water temperature, i.e. the median value for the lower most sensors (230-240) as well as the temperature value for every single sensor (1-240). The IMB buoy dataset also contains measurements of the snow and ice thickness [m] as well as the change in thickness [m] for each time step.

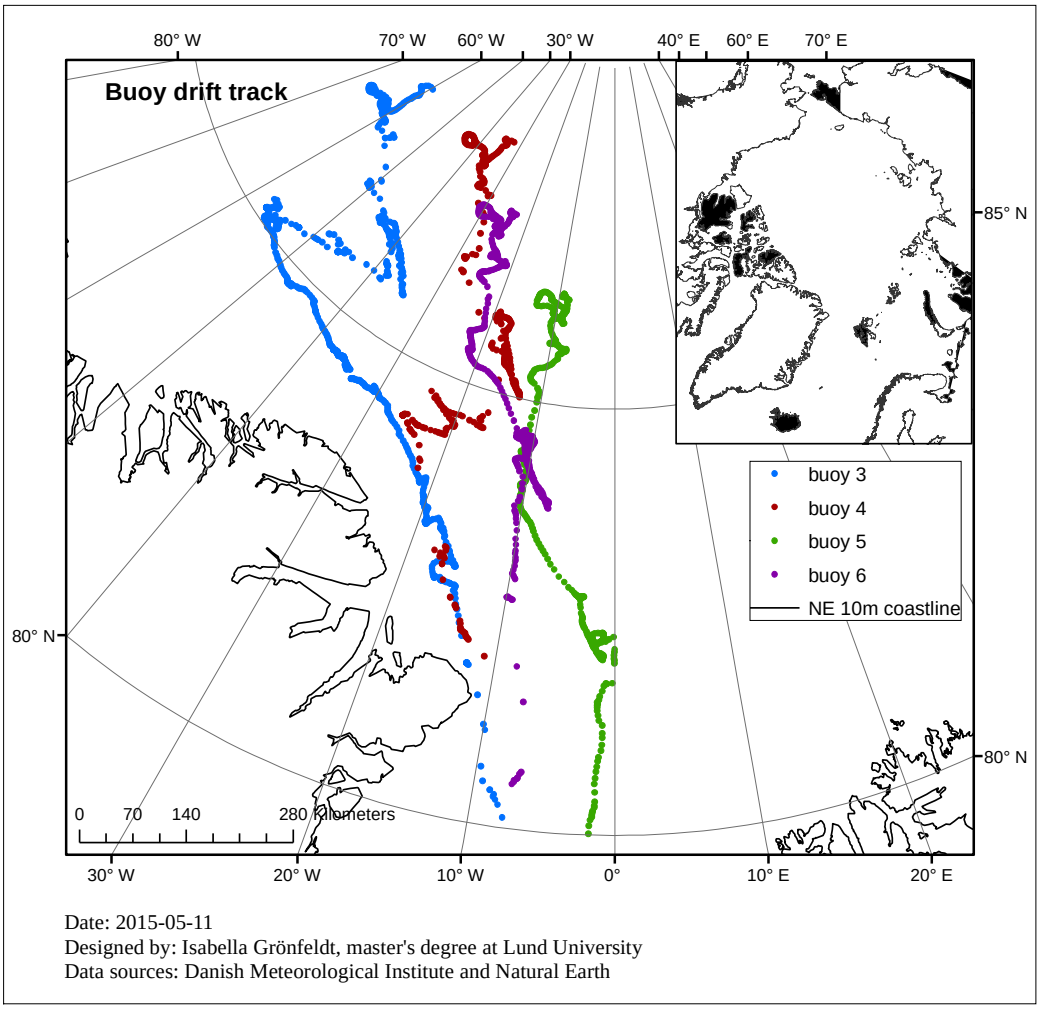

Figure 10. Buoy drift tracks for 4 of the ice mass balance buoys deployed in August 2012, north of Greenland, by staff from the Danish Meteorological Institute. The buoys drifted down along the east coast of Greenland and transmitted data until they for various reasons stopped transmitting and were lost. This map shows the drift tracks of the buoys from the 1st of September 2012 until they reached 80° north.

3.2. Numerical weather prediction (NWP)

Numerical weather prediction (NWP) data is achieved by taking observation data of the current state of the atmosphere which is then run through integrated computer models. The outcome will be the future state of the atmosphere, described at a series of grid points by different meteorological parameters such as temperature, pressure and precipitation (Buizza, 2000; NOAA, 2015). The European Centre for Medium-Range Weather (ECMWF) also uses its models to rerun archived observations to create reanalysis. Reanalyses are global datasets where the old observations and new models are combined (assimilated) to recreate a more accurate description of the state of the atmosphere for the recent history. ECMWF's ERA Interim is such a climate reanalysis, ranging from 1979 to present. ERA Interim describes global atmospheric and surface parameters at a spatial resolution of 80 km. The parameters are described every 6 hours, at 0 UTC, 6 UTC, 12 UTC and 18 UTC (ECMWF, 2015).

The NWP data from ERA Interim used in this study are provided by DMI. The dataset is spatially and temporally collocated to the IMB buoy data, with a temporal limit of ±1 h and a spatial of ±0.5 degree. The data contains information on time difference to the buoy data, age of each prediction, values for mean sea level pressure [hPa], 2m air temperature [K], wind speed [ms^{-1}], incoming shortwave and longwave radiation [$Jm^{-2}s^{-1}$], dew point temperature [K], 6h accumulated precipitation [mm], total cloud cover [kgm^{-2}], total column of ice water [kgm^{-2}] and total column of water vapour [kgm^{-2}].

3.3. Satellite data

There are a number of different satellite sensors measuring in different bands of the electromagnetic spectrum. The sensors used for this study are visible to thermal infrared and microwave radiometer sensors, a total of three sensors. The satellite data are collocated to the IMB buoys.

3.3.1. AMSR-2

Advanced Microwave Scanning Radiometer - 2 (AMSR2) is a passive radiometer sensor measuring in the microwave band. The sensor is boarded on the Japan Aerospace Exploration Agency's (JAXA) Global Change Observation Mission for Water "SHIZUKU" (GCOM-W1) spacecraft, launched May 2012 (JAXA, 2015). AMSR2 has a conical scan mechanism with a rotating 2 m antenna (remss, 2015). The sensor has 14 channels; 6.9, 7.3 10, 18, 23, 36 and 89 GHz for both vertical and horizontal polarization. It has a swath width of 1450 m and a varying resolution depending on frequency (WMO, 2015). The frequency channels 6.9-36 GHz have a sampling interval of 10 km and a spatial resolution varying from 35*62 km to 7*12 km. The 89 GHz channel has a sampling interval of 5 km and a resolution of 3*5 km (JAXA, 2015). The AMSR2 data for this study, containing all of the 14 channels, was provided by the Technical University of Denmark (DTU). The data are collocated to the buoy data at the exact location of the buoy with a spatial margin of ±0.02 degrees and a temporal limit of ±2 h.

3.3.2. SMOS

Aboard the European Space Agency's (ESA) Soil Moisture Ocean Salinity (SMOS) is the Microwave Imaging Radiometer using Aperture Synthesis (Miras) sensor. It was launched in 2009 as a part of ESA's Earth Explorer mission. Miras is of the same sensor type, microwave radiometer, as AMSR2. It measures the 1.413 GHz frequency with horizontal and vertical

polarization. The sensor has three available angels; 0° (nadir), 25-35° and 40-50°. With its Y-shaped pushbroom scan mechanism it has a swath width of 1000 m and a spatial resolution of 35 km (ESA, 2015). The data from the Miras sensor is henceforth referred to as SMOS data in this study. The data used contains 5 channels, due to the different incident angels, and are provided by the University of Bremen. The data are collocated to the buoy data with the same spatial and temporally limits as the AMSR2 data, i.e. a spatial limit of ±0.02 degrees and a temporal limit of ±2 h.

3.3.3. TIR

The fifth and last type of data used in this study is thermal infrared (TIR) measurements of the Earth's surface. The data comes from the Advanced Very High Resolution Radiometer (AVHRR) aboard EUMETSAT's MetOp satellite, and are provided by DMI (EUMETSAT, 2015). Thermal infrared radiation is sensitive to cloud cover, as discussed in Section 2.3, therefore the sensor is dependent on good weather conditions and clear skies. The provided data are collocated to the buoy data with a temporal difference of no more than ±1 h and a spatial difference of ±3 km. Due to cloud cover the collocated TIR data is sparse and contain gaps.

3.4. Match-Up dataset

The NWP and satellite data, i.e. AMSR2, SMOS and TIR, are collocated to the temporal and spatial location of the buoy data using Matlab (Mathworks, 2014). Only the data points with a matching time and date in all the data sources are included in the match-up dataset and subsequent analyses. During the processing several doublets for the buoy date were discovered and removed. The creation of the match-up dataset makes data handling easier as well as it makes certain that the satellite data matches the IMB buoy data in time and space. This is important since the satellites do not follow the drift tracks of the IMB buoys but circles the Earth in their own orbit, and it is essential to get satellite measurements as the sensors are above the location of the buoys.

3.5. Data analysis and empirical models

Several empirical models and relationships are used in this study to calculate values for the snow and ice parameters for the different levels studied in the snow and ice layers, i.e. the air-snow interface, the snow layer, the snow-ice interface and 0.1, 0.3 and 0.5 m into the ice. The data analysis in this study has mainly been performed using Excel (Microsoft, 2010), and occasionally Matlab (Mathworks, 2014).

3.5.1. Emissivity, spectral gradient ration and polarization ratio

As the actual temperature is dependent on the brightness temperature measured by the satellite sensors and the emissivity, it is interesting to calculate and look at the snow layer emissivity. In this study the approximate 89 GHz snow layer emissivity e is achieved by dividing the brightness temperature of the 89 GHz horizontal polarization channel Tb_{89H} with the mean snow layer temperature T.

$$e = Tb_{89H}/T \quad (1)$$

The spectral gradient ratio (GR) and polarization ratio (PR) are related to the emissivity. By using the brightness temperature in the form of the normalized GR or PR value the effects of the physical snow temperatures are removed. The variations in the GR or PR values are then only dependent on the emissivity. This form for the brightness temperature is used in many algorithms (Willmes et al., 2014). GR and PR can be used for many different frequencies (and combination of frequencies) but the most commonly used are channels 18 and 36 GHz horizontal polarization for GR and 18 GHz horizontal and vertical polarization for PR (Willmes et al., 2014; Tonboe, 2010), which are also used in this study.

$$GR_{18/36} = (Tb_{36V} - Tb_{18V})/(Tb_{36V} + Tb_{18V}) \quad (2)$$

$$PR_{18} = (Tb_{18V} - Tb_{18H})/(Tb_{18V} + Tb_{18H}) \quad (3)$$

3.5.2. Snow density and thickness

Snow densities p [kgm^{-3}] are calculated for every measuring point using density algorithms by Jordan et al. (1999), the International Organization for Standardization (ISO) (1998) and Pomeroy et al. (1998). The resulting snow densities are all for freshly fallen snow as there is no time dependency in the algorithms, and no consideration is taken to the already fallen snow.

The algorithm by Jordan et al.(1999) is based on measurements from drifting stations 5° latitude from the North Pole, operational from April 1956 to April 1957. It describes a relationship between the snow density p [kgm^{-3}], the air temperature T_{air} [K] and the wind speed u [ms^{-1}], though for colder temperatures the snow density is solely based on wind speed.

$$p = 500 * \left(1 - 0.951 * e^{-1.4*\left((278.15-T_{air})^{-1.15} - 0.008*u^{1.7}\right)}\right) \quad (4a)$$

for $260.15 < T_{air} \leq 275.65$ K and

$$p = 500 * \left(1 - 0.904 * e^{-0.008*u^{1.7}}\right) \quad (4b)$$

for $T_{air} \leq 260.15$ K, where T_{air} is buoy air temperature [K] and u is NWP 10 m wind speed [ms^{-1}] at any given time. The algorithm presented by ISO (1998) is based on measurements and formulas from the former Soviet Union, for estimation of snow density on roof tops.

$$p = \left(90 + 130 * \sqrt{ds}\right) * \left(1.5 + 0.17 * \sqrt[3]{T_{air}}\right) * \left(1 + 0.1 * \sqrt{u}\right) \quad (5)$$

where ds is the snow depth [m], T_{air} is the air temperature [°C] and u is the 10 m wind velocity [ms^{-1}] at any given time. The final snow density algorithm by Pomeroy et al. (1998) is developed from density measurements of snow drifts in Wyoming, USA, and in the Canadian Prairies. These areas are considered relatively dry and cold. The algorithm separates freshly fallen snow from aged and wind-blown snow by setting up a limit at 0.60 m snow thickness. For new and freshly fallen snow, with a snow thickness ≤ 0.60 m, the snow density is solely based on air temperature.

$$p = 67.9 + 51.3 * e^{T_{air}/2.6} \quad (6a)$$

where T_{air} is the temperature at any given point [°C]. For aged wind-blown snow > 0.60 m

$$p = 450 - \left(\frac{20470}{ds}\right) * \left(1 - e^{-(ds/67.8)}\right) \quad (6b)$$

where *ds* is snow depth [cm].

The calculated densities, from Equations 4-6, are applied to the summed NWP 6h accumulated precipitation to try and estimate the variations of the actual snow cover thickness. The initial density of the summed NWP 6h accumulated precipitation, i.e. 106 kgm^{-3}, is divided by the calculated density for each measuring point. The ratio of the densities is then multiplied with the NWP snow thickness, i.e. the summed 6h accumulated precipitation. The result is three new density weighted snow cover thicknesses for each measuring point.

3.5.3. Snow-ice interface temperature

The snow-ice interface temperature in this study is evaluated against the 6.9 GHz V channel, in line with the findings of Tonboe et al. (2011). The simulations conducted by Tonboe et al. (2011) indicated that a simple linear model could be used to derive the snow-ice interface temperature from AMSR2 6.9 GHz measurements.

$$T_{snow-ice} = 1.23 * Tb_{6.9V} - 57.81 \quad (7)$$

3.5.4. Ice thickness

In an attempt to estimate the measured sea ice thickness [m], empirical models from Lebedev (1938),

$$Ice\ thickness = 1.33 * fdd^{0.58} \quad (8)$$

Zubov (1943)

$$Ice\ thickness = \pm\sqrt{8 * fdd + 625} - 25 \quad (9)$$

and Maykut (1986) are used.

$$Ice\ thickness = ((1/10) * (\sqrt{1290 * fdd + 7056} - 84))/100 \quad (10)$$

$$Ice\ thickness = \left((1/20) * (\sqrt{17161 * (hs * 100)^2 + 44016 * (hs * 100) + 5160 * fdd + 28224} - 131 * (hs * 100) - 168)\right)/100 \quad (11)$$

where *hs* represents the thickness of the snow cover [m] and *fdd* cumulative freezing degree days. Maykut Equation 11, with snow thickness as a variable, is a development of Equation 10, since Equation 10 were seen to give higher values compared to observations.

The empirical models are based on freezing degree days (*fdd*), i.e. the difference between the freezing temperature of the ocean water set as 271.34 K and an approximation of the daily mean air temperature, median value of 4 adjacent measurements of buoy air temperature. The starting *fdd* are calculated using the reversed equations of Lebedev (1938), Zubov (1943) and Maykut (1986) respectively to get the accurate starting value for the ice thickness. The *fdd* for

each day are then summed up to a continous cumulative *fdd* which is used in the empirical models to get new theoretical values for the sea ice thickness.

3.6. Multiple regression analysis

The multiple regression analysis performed in this study, with the goal of estimating the temperature profile through the snow and ice layers, is performed on buoy 3, for the period 2012-10-01 to 2013-04-29. September has been omitted due to the relatively high observed temperatures and large fluctuations in the satellite data. The same applies to May, as the temperatures started to rise again. This is done to avoid contamination and unwanted errors in the dataset mainly due to water vapor. A wide range of combinations of channels is used to try and find the best fit for the measured temperature profile for buoy 3. In cases where TIR data are evaluated the period stretches from the end of November to the end of May, due to data availability.

The regression analyses are performed using the built in data analysis tools in Excel (Microsoft, 2010), where the variables are chosen manually. It is used with a confidence level of 95%, meaning that the coefficient values are within a standard deviation limit of 5%, 95% of the time.

3.6.1. Control

To evaluate the goodness of fit of the models the coefficients, retrieved in the regression analysis for buoy 3, are applied to buoy 4-6 as a control. Temperature values above 270 K are removed from the control analysis as the satellite measurements are sensitive to changes in emissivity, and thereby increased penetration depth, induced by melting process in the snow layer. New temperature values are calculated, using the derived multiple regression models, for all the depths through the snow and ice layer, for buoy 4-6. The correlation between measured and calculated temperature values is evaluated.

4. Results and Discussion

It is of great importance to be able to rely on the remote sensing and prediction data, such as the thermal and microwave radiation satellite data and NWP data, when concerning sea ice and snow cover in the remote Arctic region. Since the area is so vast and inaccessible, in situ measurements are scarce. Continuous confirmation of the remote sensing data and model predictions are therefore important.

The goal for this study is to reproduce the observed temperature profile for the snow and ice layers (see Figure 11) with the use of modelled NWP and measured satellite data. To be able to do this one level at the time in the snow and ice layers has to be studied and analyzed. Measurements from the IMB buoys have to be compared with the modelled NWP and the measured satellite data, to confirm the accuracy of the data and to find relationships and strong correlations. This is done, for all four IMB buoys (but not all of the results are presented here), to be able to choose adequate components for the multiple regression analysis, performed on buoy 3, and reproduce the measured temperature profile. The simple empirical models created from the multiple regression analysis will be validated with the use of a control dataset from buoys 4-6.

In general the air is much colder than the ocean during the winter in the Arctic and the temperature decreases down through the snow and ice layers, which can be seen in Figure 11 and Appendix B. As the air temperature increases significantly however, the ice is colder than the overlaying snow and air, and due to the insulating properties of the snow layer the heat flow travels slowly through the ice. This can be seen on the 27th of November and the 6th of January for buoy 3 in Figure 11. In the same way when the air temperature drops significantly the ice is isolated from the cold and the temperature difference between the snow and ice layers increases. Such significant drops in air temperature can be seen on the 14th of December for buoy 3 as well as at the minimum temperature on the 22nd of February and the drop at around the 25th of March.

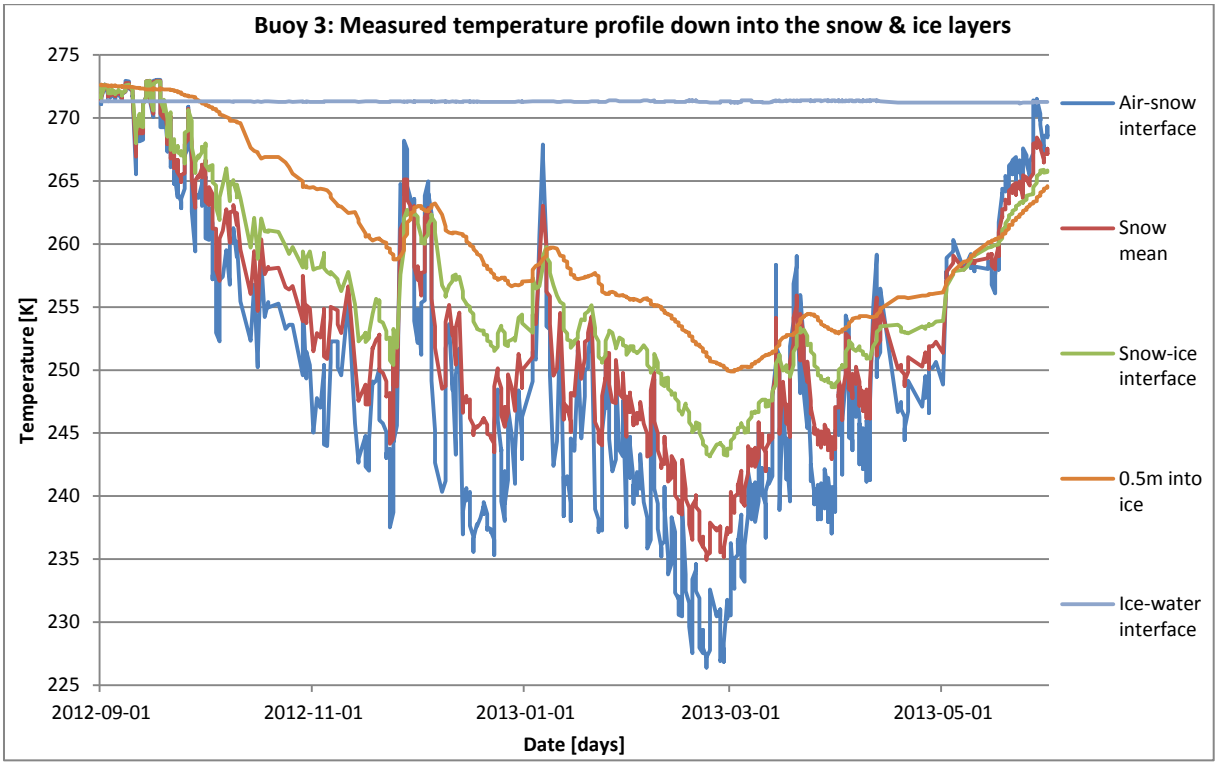

Figure 11. The measured temperature profile down into the snow and ice layers for buoy 3, 2012-09-01 until 2013-05-31; air-snow interface temperature (dark blue), snow mean (red), snow-ice interface (green), 0.5 m into the ice (orange) and the temperature at the ice-water interface (light blue). For full temperature profiles for all the buoys see Appendix B.

4.1. Air-snow interface

The top most layer of the snow and ice column, to be studied and analysed, is the surface, i.e. the air-snow interface. The modelled NWP 2m air temperature, the measured IMB buoy air and air-snow interface temperature and the TIR as well as AMSR2 channels of high and low frequencies are compared.

4.1.1. Air temperature and NWP

To confirm the accuracy of the NWP data the NWP 2m air temperature is compared to the actual air temperature measured by the IMB buoy. Figure 12 shows how the NWP 2m air temperature captures the natural fluctuations of the buoy air temperature. The two temperatures are correlated to each other with a R^2-value of 0.87. However, the NWP values seem to have less daily variability and a smoothening effect on the actual variation, as the modelled temperature values do not go as low or as high as the actual values. This is especially true for rapid and large temperature shifts, and can be explained by the fact that the spatial resolution of the NWP data (80 km) is larger than that of the buoy data, which is very precise and accurate.

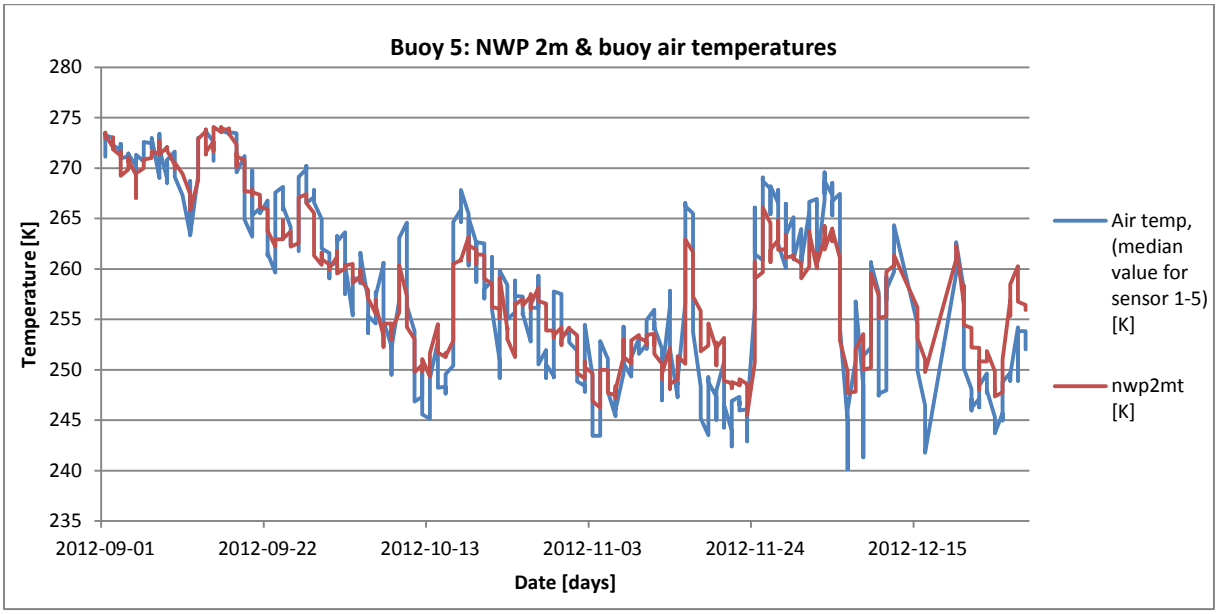

Figure 12. Buoy air temperature (median value for sensor 1-5) as a blue line and NWP 2m air temperature as a red line, both in Kelvin, for buoy 5 over the period 2012-09-01 to 2012-12-29.

The correlation between the two temperatures is higher in September and for warmer temperatures than later on into the colder winter season. There is a temperature difference of about 10 K for the minimum temperatures and a difference of less than 1 K for the maximum. The temperature fluctuations are also stronger during the stormy winter season, which can be seen in Figure 12 during November. To further study the temperature difference, and try to find physical explanations for the dissimilarities illustrated in Figure 12, the temperature difference between the buoy air temperature and the NWP 2m temperature is calculated by subtracting the NWP 2m air temperature from the buoy air temperature, see Figure 13. From the figure it is clear that November to December is also the time when the NWP temperature displays the largest difference to the buoy temperature.

The mean, i.e. the bias, and standard deviation of the temperature differences for buoy 5 in Figure 13 were calculated to be -0.27 K and 3.32 K respectively, marked with a green area in the figure. The non-zero mean for the temperature difference indicates a systematic error and since it is a negative value the NWP values are generally higher than the buoy values, i.e. the NWP is overestimating the actual air temperature. All the values of temperature difference exceeding the standard deviation (marked as red points in Figure 13), i.e. 31% of the data points, are named extreme events. Extreme points above the green area in Figure 13 indicates that the NWP temperature value is significantly lower than the buoy value and consequently points below the area indicates significantly higher NWP values. The maximum temperature difference between the buoy air temperature and the NWP 2m temperature is 8.31 K and the minimum is -9.35 K. Similar values are found for buoy 6.

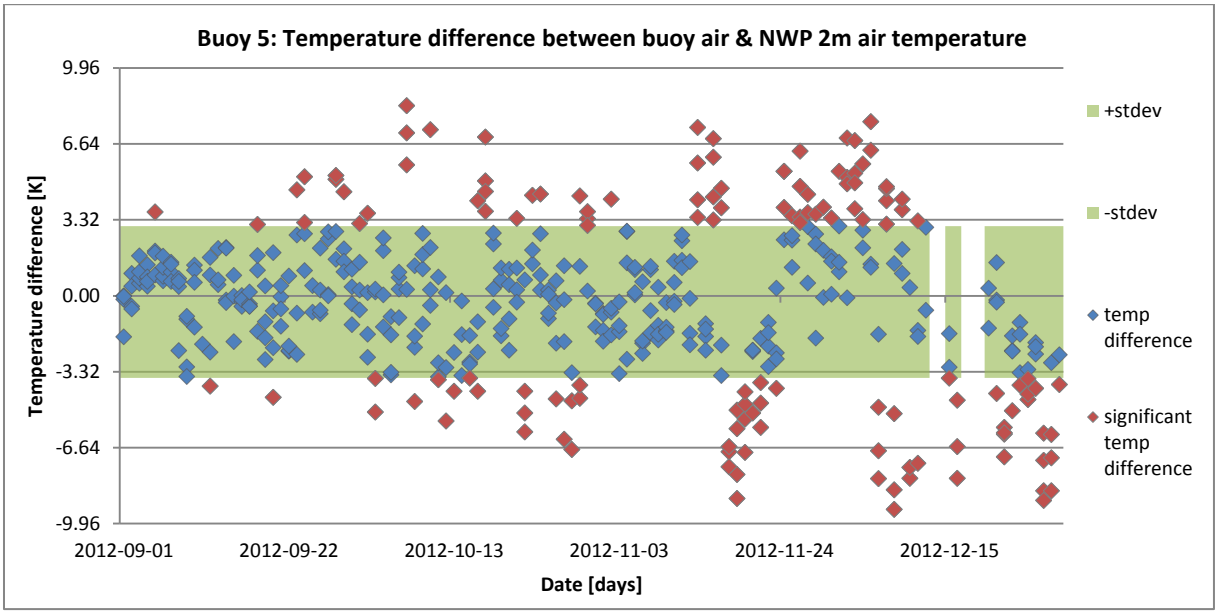

Figure 13. The temperature difference between the air temperature for buoy 5 and the NWP 2m air temperature during the period 2012-09-01 to 2012-12-29. The standard deviation (±3.32 K) from the mean temperature difference of -0.27 K is marked with a green band. The values within the standard deviation limit are marked blue while the extreme events, i.e. when the temperature difference exceeds 3.32 K, are marked red.

The temporal occurrence of the extreme events are compared to other external forces such as changes in snow cover thickness, buoy sensor height above ground, air temperature, wind speed, mean sea level pressure, cloud cover, etc. to try and find a pattern. A first thing to note is that the buoy air temperature is calculated by taking the median of the 5 sensors highest above ground level in the chain of sensors. These are not at 2m height but vary, depending mainly on the snow thickness. The height for the buoy 5 air temperature varies between 0.04-0.49 m ±0.05 m. This means that the height difference between the buoy temperature and the NWP temperature is never less than 1.5 m. This can cause differences in the measurements, especially during winter due to the negative radiation balance, i.e. when the ground surface could be colder than the air 2m above due to winds and outgoing longwave radiation (Maykut, 1986).

The extreme temperature difference events do not occur simultaneously with changes in height or snow cover. There is no clear explanation of why the modelled NWP temperature is deviating so much from the actual temperature at the extreme points, such as between the 13th-16th of November and 24th-28th of November in Figure 13, when comparing with other predicted physical parameters in the NWP dataset. There is however, a correlation between the significance of the temperature shifts and the offset of the NWP 2m air temperature to the buoy air temperature. The main reason for the significant differences is likely due to the course spatial resolution of the NWP and/or the NWP model: the NWP is based on modelling and the quality is dependent on the quality of the model, including sea ice and snow properties themselves, and the quality and amount of the assimilation data. It might be the case that the model is poor in the specific region or time period, either way the assimilated data is known to be sparse.

4.1.2. AMSR2 89 GHz

In this study it is expected to see a correlation between the surface temperature and the AMSR2 89 GHz channel which has a low penetration depth.

When comparing AMSR2 89 GHz horizontal (H) and vertical (V) polarization to the NWP 2m air temperature, buoy air temperature and air-snow interface temperature (see Appendix C1) it is clear that the horizontal polarization has an overall higher correlation, i.e. R^2-values of 0.37-0.51 versus 0.30-0.43. The correlation is also highest for the modelled NWP 2m air temperature (R^2=0.43-0.51) and decreases for the buoy air temperature (R^2=0.38-0.45) and the air-snow interface (R^2=0.30-0.37). This is in line with the theory that the 89 GHz has a low penetration depth, as it has a short wavelength and gets scattered and absorbed easier than the lower frequency channels (Lubin and Massom, 2006; Mathew et al., 2008; Tonboe, 2010).

The time series for the well correlated NWP 2m air temperature and the AMSR2 89 GHz H can be seen in Figure 14. The two curves seem to have similar fluctuations but are separated by a mean of 58.24±8.27 K, as the 89 GHz H brightness temperature is significantly colder than the NWP 2m air temperature. This is due to the fact that the satellite channels only measure the brightness temperature of the surface. The brightness temperature is dependent on both the actual, effective temperature, and the emissivity of the snow (Lubin and Massom, 2006). This leads to lower temperatures for satellite measurements such as the 89 GHz channel than the actual temperature values, or in this case the predicted temperature values.

The NWP and buoy temperature values are relative steady as they reach temperatures above 270 K, during September, at the same time the 89 GHz satellite measurements vary significantly (see Figure 14). This is due to the fact that as the temperature approaches the freezing temperature of 273.15 K for pure water and 271.29 K for the saline ocean. The high temperatures initiate melting processes in the snow and ice which affect the snow emissivity, significantly decreasing the penetration depth, and thereby alter the signal received by the sensors (Eicken, 2003; Lubin and Masson, 2006). An upper temperature threshold is therefore set at 270 K for the buoy and NWP temperature values (this is also done for the remaining analysis in this study as the behaviour is observed for the entire dataset). After the temperature threshold is set up the R^2-values are lowered for all the buoys and temperature correlations. The NWP 2m air temperature and 89 GHz H which had the highest correlation decreased its goodness of fit with about 0.24 units, to a resulting maximum R^2-value for buoy 3 of 0.55 and a minimum for buoy 4 of 0.17.

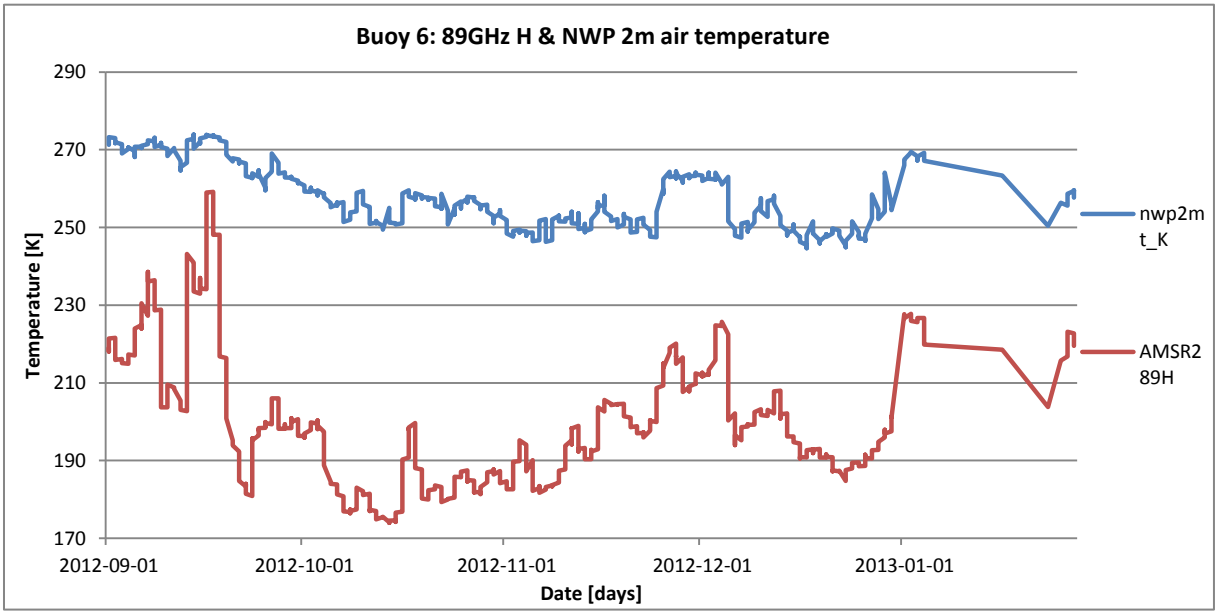

Figure 14. Time series of the NWP 2m air temperature (blue) and AMSR2 89 GHz H brightness temperature (red) for buoy 6 from 2012-09-01 until 2013-01-27.

The measured air-snow interface temperature are compared against other wavelengths as well, apart from the AMSR2 89GHz, such as AMSR2 7.3GHz. The level of correlation differs significantly between the buoys. When plotting the AMSR2 7.3 GHz V against the air-snow interface, with the applied temperature threshold, for buoy 5 it displays a R^2-value of 0.28 while buoy 6 gives a R^2-value of 0.59.

The results presented in this section show that the surface and air temperature are not always connected to the internal thermal microwave radiation. It is especially difficult for the satellite data to capture the high temperatures around the freezing point, due to melting processes that alters the emissivity.

4.1.3. TIR

The thermal infrared radiation is expected to show high correlation with the air-snow interface temperature, even more so than the 89 GHz channel, as the TIR is known to be emitted from the top surface and can only penetrate a few millimetres of the surface layer (Lubin and Massom, 2006).

To confirm the TIR temperature measurements they are compared with the NWP 2m air temperature, the IMB buoy air temperature, the buoy air-snow interface (Figure 15) and with the AMSR2 89 GHz H (Appendix C2). The linear goodnes of fit is highest for the air-snow interface and TIR which has a R^2-value of 0.59, see Figure 15. This is as expected since the TIR gives an accurate estimation of the surface temperature (Wan et al., 2002; Tonboe et al. 2010). The sparse data is due to cloud coverage, as the TIR wavelengths can't penetrate clouds. Clouds pose a great uncertainty to the measurements as the sensor may measure the much colder temperature of the cloud tops and lower the resulting temperature values. This can be seen in Figure 15 as the TIR temperature is generally lower than the temperature of the air-snow interface. However, it captures the natural variations of the air-snow temperature, especially in December where the TIR points are close to the air-snow temperature curve. The TIR better captures the temperature variations than the modelled NWP, which had difficulties following the significant fluctuations of the buoy temperature. At the beginning and end of the measuring period for buoy 4, i.e. during September-October and March-April, the correlation between the TIR and air-snow interface temperature is weaker, though the data is very sparse at the end of the period.

There are two deviating data points in the TIR dataset for buoy 4. The points can be seen in Figure 15 (and Appendix C2) as two significantly lower TIR points in January. On January 2nd and 6th 2013 the TIR temperature values drop with 30 K from one measuring point to the next after which it immediately increases with 20 K again. This indicates that the measurements are erroneous, possibly due to cloud cover interference. Indeed the NWP data does predict snowfall on both occasions; 1.88 mm 6h accumulated precipitation on January 2nd and 0.92 mm on the 6th. The IMB buoy does not register any change in snow cover thickness for the same period, which can be explained by the fact that the smallest change in snow thickness possible for the buoy sensors to register is 2 cm, due to the spacing of the sensors. The NWP data also predicts higher values for the total cloud cover, total column of ice water and total column of water vapor relative the surrounding measuring points, for the specific dates, than the buoy data. It is therefore possible that the TIR sensor has measured the temperature of the cloud tops instead of the surface temperature. There are only 1-2 TIR samples for these specific measuring points when the mean number of samples is 12. If the two erroneous points are removed the goodness of fit for the air-snow interface and TIR is increased, from a R^2-value of 0.59 to 0.69.

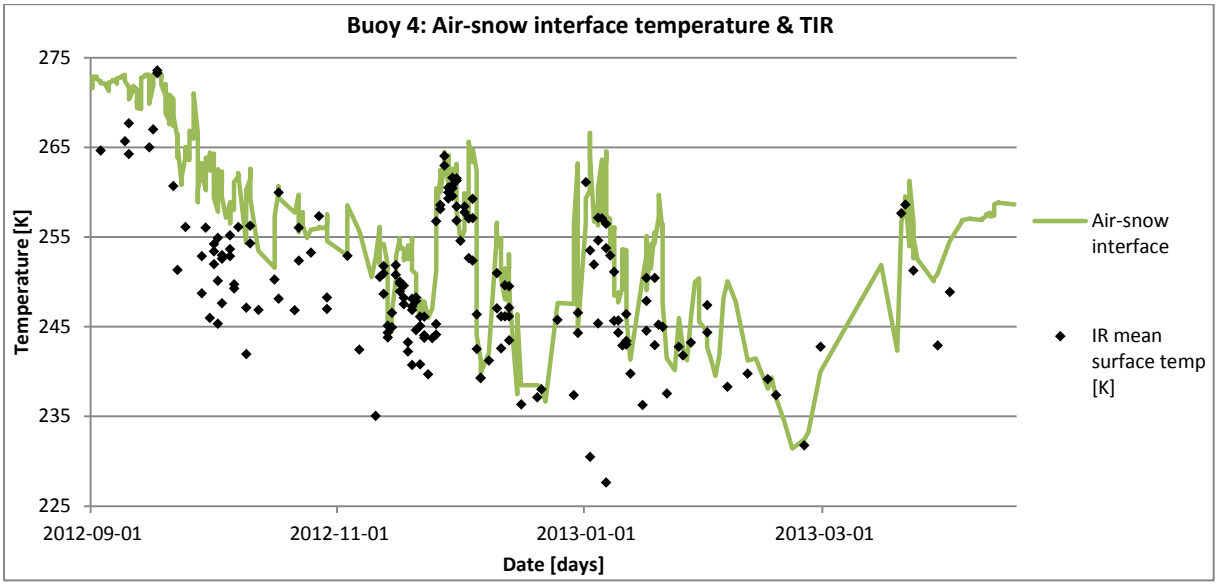

Figure 15. Buoy air-snow interface (green line) and TIR (black dots) temperature measurements for buoy 4, during the period 2012-09-01 to 2013-04-17.

When comparing the TIR data to the AMSR2 89GHz H data there is a remarkable difference between the values; the AMSR2 89 GHz H values are significantly lower than the TIR values all through the measuring period. The mean temperature difference is 49.20±10.01 K. It was expected that the TIR values would be lower as the air temperature is lower than the internal temperature of the ice and snow layer during the winter, and the TIR radiation is emitted from the top surface layer, i.e. no deeper than 1 mm. The 89 GHz H radiation, on the other hand may penetrate the snow layer differently depending on the conditions of the snow, whether it is warm/cold and wet/dry. It also measures the brightness temperature of the surface, as discussed earlier, and the effective temperature is dependent on both the brightness temperature and the emissivity of the snow. It is therefore clear and to be expected that the values for the two temperature measurements do not correlate exactly.

4.2. Snow layer

The properties of the insulating snow cover are of significant importance for the temperature profile all through the snow and ice column. In this section the snow layer mean temperature, emissivity, density and thickness are derived and discussed. Each of these snow parameters influence the brightness temperature measured by the satellite sensors, and therefore are important in the reconstruction of the temperature profile.

4.2.1. Snow layer temperature

In this study the average snow temperature is calculated by taking the mean of the air-snow interface and snow-ice interface temperatures. This should be equal to the mean snow temperature in the case of a linear temperature gradient through the snow, which is assumed in this study as a simplification based on the observed IMB buoy temperature profiles, see Figure 16. The temperature for buoy 5 in the figure is not varying but is steadily increasing from the mean air-snow interface down through the snow layer to the mean snow-ice interface. This approximated mean snow temperature is further referred to as the measured mean snow temperature in this study.

As is clear from Figure 16, the observed vertical temperature profile is not always linear. The thickness, as well as the vertical profile of the density of the snow cover determines the shape

of the temperature profile, due to the heat capacity and insulating properties. The effect of the snow thickness is to slow down the diffusive processes by which the temperature profile stabilizes to a given air temperature, i.e. thermodynamic equilibrium. When the air temperature changes rapidly it takes time for the temperature profile to adjust and during that time the profile is often nonlinear. This can clearly be seen for buoy 3 in Appendix D1, which has thicker snow and ice layers than buoy 5 in Figure 16 and a more exponential vertical temperature profile. When stability has been reached, the profile is again (piecewise) linear.

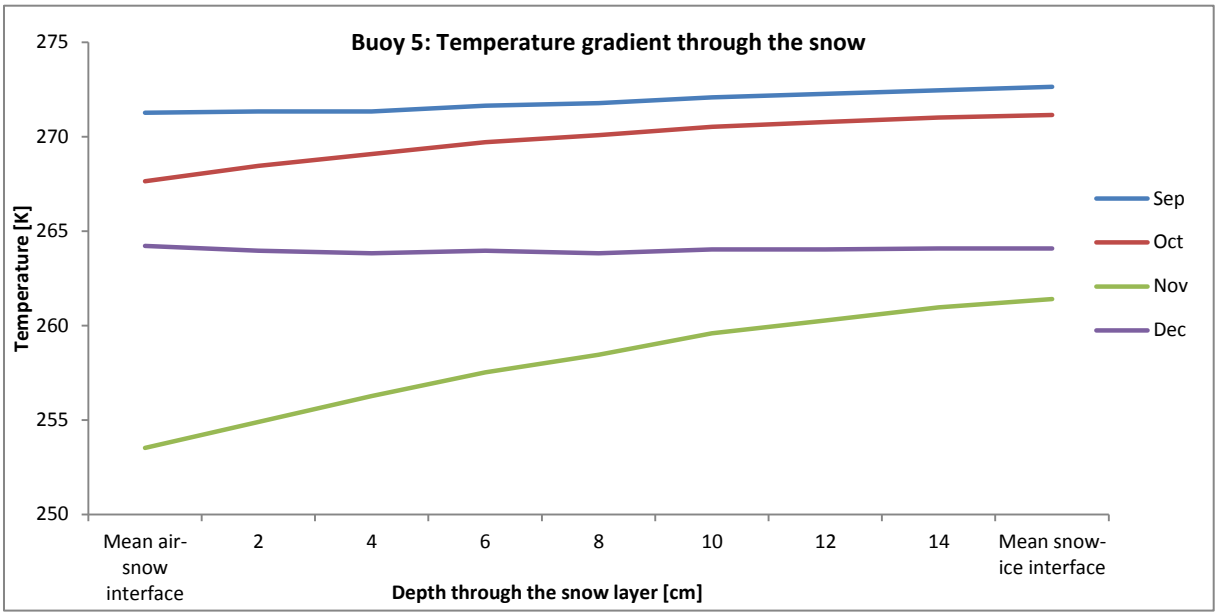

Figure 16. The measurements for buoy 5 show an approximate linear temperature gradient through the snow layer. The temperature gradient for the 1st each month is displayed in the figure; blue line for September, red for October, green for November and purple for December 2012.

4.2.2. Emissivity

As the brightness temperature measured by the satellite sensors is dependent on the actual temperature of the surface and the emissivity it is interesting to calculate and look at the snow and ice layer emissivity. During the freezing conditions of the winter period the emissivity of snow is very low at most microwave frequencies, but the emissivity of ice is high. This means that it is possible for most microwave frequencies to see through the snow and the emissivity is largly due to the ice properties, i.e. the emissivity is a combined measurement of the emission from the snow and ice layers (Lubin and Massom, 2006). The average snow and ice emissivity for the 89 GHz frequency channel for buoy 5, from Equation 1, is about 0.75-0.80, see Figure 17. This is in line with the studies by Mathew et al. (2008) which concluded that the 89 GHz emissivity for multiyear ice in the period November-May 2005 was constant at about 0.80. Similar results were obtained during the simulations studies by Tonboe (2010), where the average snow and ice layer emissivity for 89 GHz was about 0.75-0.80 during the simulation period September 1999 until May 2000 (Tonboe, 2010).

The emissivity has been compared to the measured snow thickness, see Figure 17. There is no correlation between the peaks in emissivity and snow cover thickness. This shows that the emissivity is independent of the snow cover thickness, but dependent on other snow parameters instead such as grain size, density and temperature.

There are large variations in the emissivity in September (see Figure 17) and it is clear that the emissivity for 89 GHz is particularly affected by surface reflection and scattering at the

beginning of the period. The same behaviour were seen in the study by Mathew et al. (2008) and could be due to relatively high air temperatures around the freezing point, melting processes and/or large grain size in the beginning of the winter season. The significant variations in the emissivity in September are a strong indicator that September should be excluded when studying the temperature gradient down through the snow and ice layers.

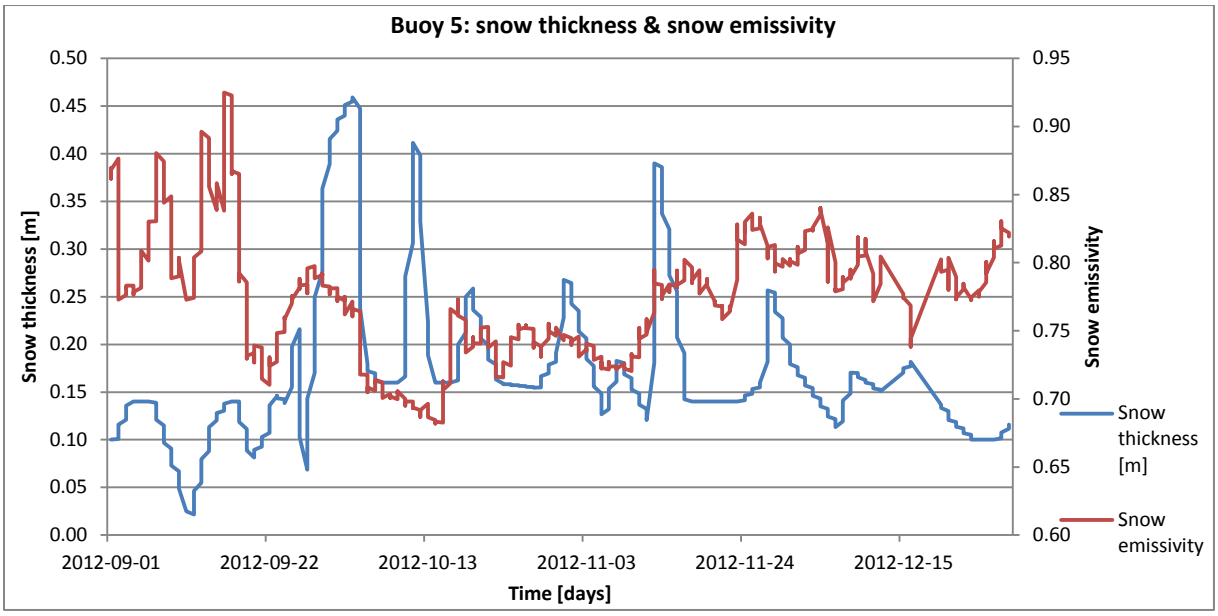

Figure 17. Measured snow thickness in meters for buoy 5 on the primary y-axis as a blue line and calculated emissivity for the snow layer Equation 1 (i.e. 89 GHz H divided by mean snow layer temperature) on the secondary y-axis as a red line. The time series is for the period 2012-09-01 to 2012-12-29.

The spectral gradient ratio (GR) and the polarization ratio (PR), which are both related to the emissivity, have been calculated for buoys 5 and 6 using Equations 2 and 3. The GR value, which is determined by the scatter in the snow, is dependent on the snow thickness and the grain size. Therefore the GR is compared to the measured snow cover thickness. In this study it was expected so see a negative dependence between the GR and the snow thickness, especially towards the end of the winter season as the grain size increases. The correlation is however very low and there is no clear dependency for buoy 5 (R^2-value of 0.05). A minor correlation can be seen for buoy 6 (R^2-value of 0.19) Appendix D2. The peaks in snow thickness seem to occur at the same time as the GR decreases and conversely, the GR peaks when the snow thickness decreases. From the analysis it is clear that in September, as the snow is relatively thin and constant at 0.12 m for buoy 6, the GR values fluctuate significantly, Appendix D2. After the variations in the beginning of the season the GR values steadily increase throughout the period, with some minor fluctuations. The mean GR value, for both buoys, of -0.05 is consistent with the results of Tonboe (2010). He found the GR seasonal mean (September-May, 1999-2000) in the Arctic Ocean to be -0.06 according to measurements and -0.05 according to his own simulations. The polarization ratio (PR), which is 0.07 for buoy 5 and 0.06 for buoy 6, is not coinciding with the simulations of Tonboe (2010) which resulted in a PR value of 0.03. The result in this study is however, in line with the measurements performed by Markus et al. (2006b) during the winter 2003 where the observed PR values ranged between 0.05 and 0.07.

4.2.3. Snow layer thickness

The measured delta snow thickness is compared to the modelled NWP 6h accumulated precipitation. It is clear that there is no correlation between the two variables. The R^2-value is 0.01 for buoy 5 (Figure 18) and 0.00 for buoy 6 (appendix D2). This is explained by the fact that the NWP precipitation is accumulated over a 6 hour period. In a similar manner the delta snow thickness is compared to the buoy air temperature and the NWP wind speed, with R^2-values equal to 0.00 (not shown).

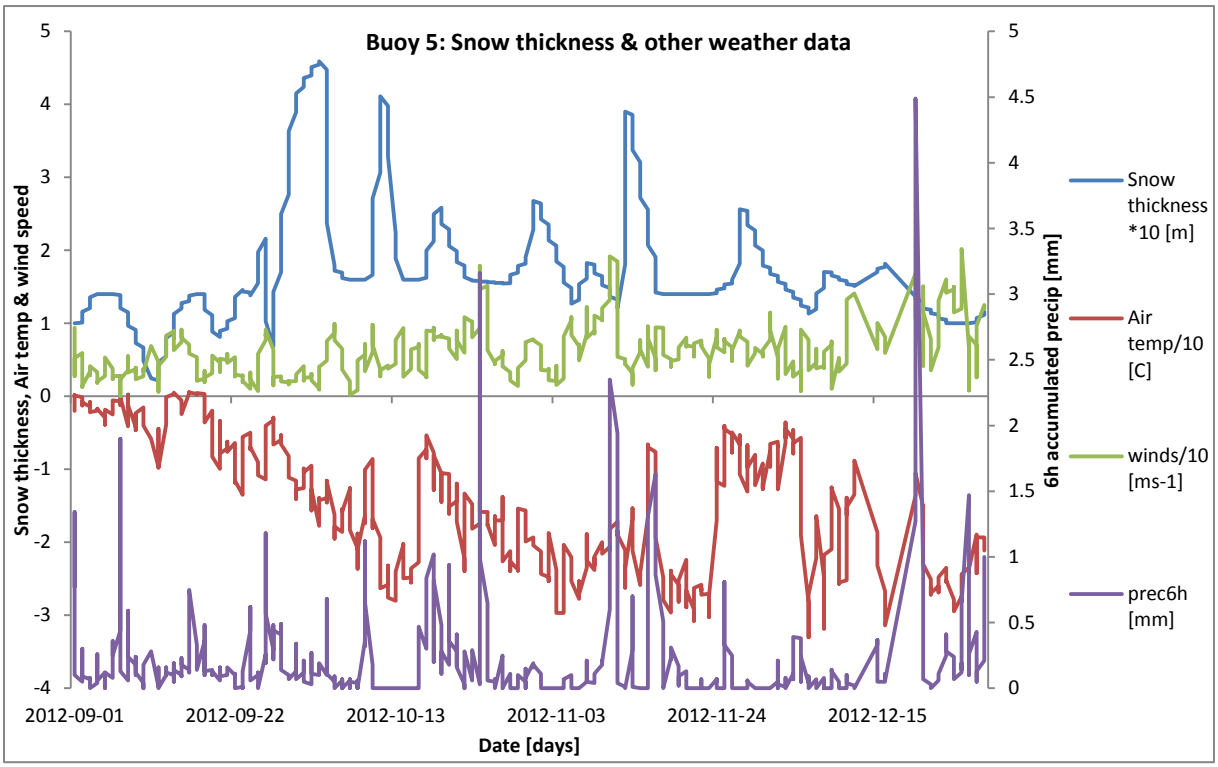

Figure 18. A time series describing the variations of the predicted and observed conditions at the location for buoy 5, 2012-09-01 until 2012-12-29; the measured snow thickness in meters times ten (blue line), buoy air temperature in Celsius divided by ten (red line), NWP wind speed in meters per second divided by ten (green line) and on the secondary y-axis NWP 6h accumulated precipitation in millimeters (purple line).

When further studying the snow thickness from buoy 5 it is evident that there are some very sharp changes in the snow cover, see Figures 18, 19 and Appendix D2. The snow thickness increases rapidly on multiple occasions, which is normal in combination with heavy snowfall events, but in this study it was expected to see a slow decrease of the snow thickness afterwards as the snow settles. In Figures 18 and 19 it is evident that the snow cover experiences an almost equally sharp drop in thickness after rapid increases. Some of the events, such as on the 4th and 12th of October for buoy 5 in Figure 18, are compared to the NWP data in an attempt to find plausible explanations for the rapid decline in snow thickness

The rapid drops in snow thickness after the extreme increases are remarkable. During the analysis it was discussed that the wind speed and the air temperature was the likely cause of these drastic drops, or possibly a combination of the two. With higher wind speeds the newly fallen snow can be moved around, towards or away from the buoy, or mixed with the older denser snow and packed. The latter process gives the snow layer a higher density, i.e. it gets a lower snow thickness. A storm would repack the entire snow layer and give the entire snow column a new density, while slightly lower but still strong winds would give a layer of newly

fallen snow approximately the same density as before the snowfall. Higher wind speeds might also transfer the snow away from the location and thereby decrease the snow thickness by removing it. Higher air temperature may also alter the density of the snow, making it wetter and heavier and thereby more dense. However this was not observed for the extreme snow events of buoy 5 (or 6, see Appendix D3), no clear explanation could be found for the sharp drops in snow thickness.

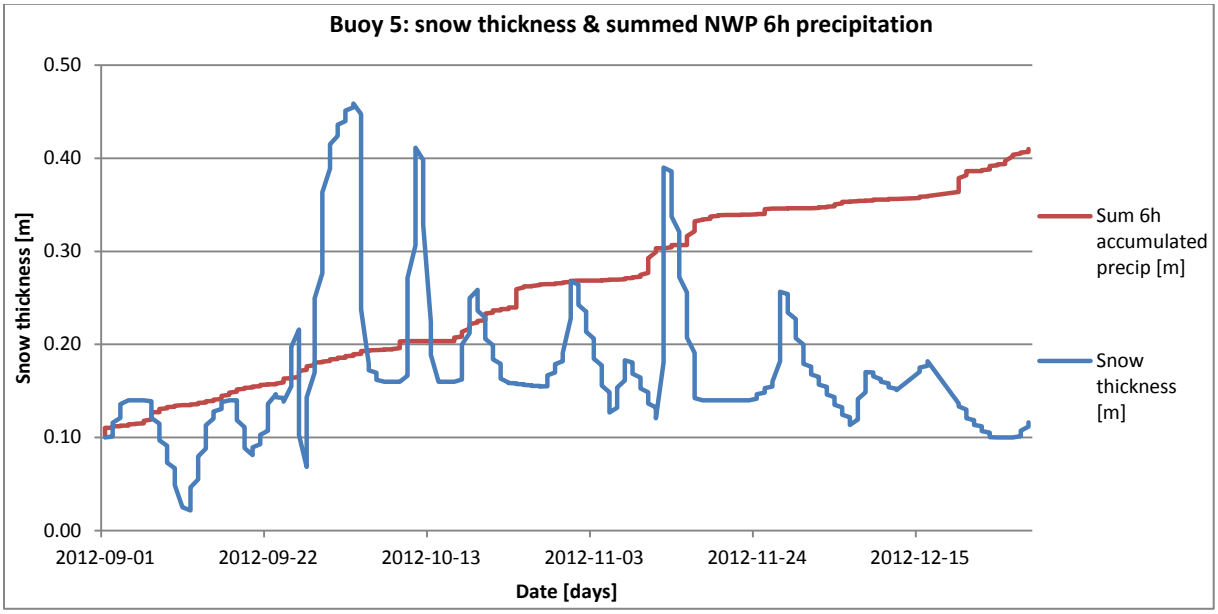

Figure 19. The snow thickness measured by buoy 5 (blue line) and the sum of the NWP 6h accumulated precipitation (red line), both in meters. The 6h accumulated precipitation has been multiplied with the ratio of the density of water (1000 kgm^{-3}) and the assumed average density of the snow layer (300 kgm^{-3}).

To be able to study the total variation of the snow cover the measured snow thickness have been compared with the sum of the modelled NWP 6h accumulated precipitation, with a fixed density of 300 kgm^{-3}, see Figure 19 and Appendix D4. The assumed average snow density of 300 kgm^{-3} is based on the observations by Warren et al. (1999) and Markus et al. (2006a). However, new snow generally has a lower density. This is difficult to model as it depends on many different factors and parameters in the snow. Therefore an average density of 300 kgm^{-3} is assumed in this study. After visual interpretation of Figure 19 it is concluded that there is no correlation between the measured snow thickness and the predicted and summed NWP precipitation. The NWP rarely captures the large snowfall events and when it does it seems to be one day ahead of the buoy data. The difference is likely due to the spatial, i.e. 80 km grid cells, and temporal resolution of the NWP data.

The resulting snow thickness at the end of the winter period is much higher for the summed NWP 6h accumulated precipitation than for the measured snow thickness; it differs by 0.30 m for buoy 5 and 0.35 m for buoy 6. This difference indicates that the accumulated snow is transformed or removed from the buoy location over time. This can be explained by different geophysical processes, such as drifting, i.e. the snow is blown away or pushed into cracks or crevasses in the ice, melting, new ice formation through snow-ice formation, snow crystal metamorphism or compacting of the snow so that it gets really dense and heavy (Pomeroy et al., 1998).

4.2.4. Snow layer density and density weighted thickness

The snow cover may experiences variations in density all through the winter and to be able to more accurately determine the snow cover thickness, it is of great importance to have density values as close as possible to the real density. Therefor a number of different empirical models for snow density are considered, Equations 4-6, to try and estimate the actual curve of the snow cover thickness from the density weighted NWP accumulated precipitation.

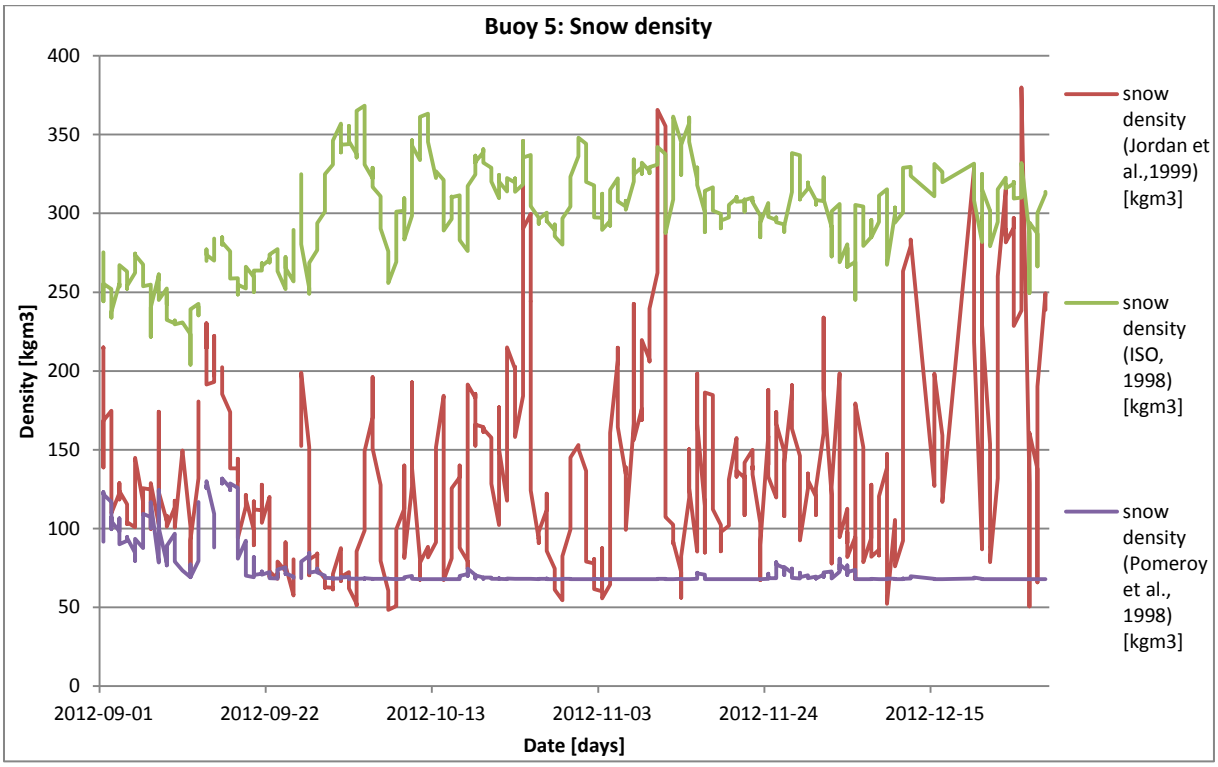

Figure 20. Calculated snow densities for buoy 5 for the period 2012-09-01 until 2012-12-29; Equation 4 Jordan et al. (1999) red line, Equation 5 International Organization for Standardization (ISO) (1998) green line and Equation 6 Pomeroy et al. (1998) purple line.

The densities by Jordan et al. (1999) (Equation 4) and ISO (1998) (Equation 5) are increasing throughout the measuring period for buoy 5, while the less varying and much lower density by Pomeroy et al. (1998) (Equation 6) decreasing (Figure 20). The mean density for Equation 6 is 74.24±14.31 kgm^{-3} while the mean value is 135.83±62.25 kgm^{-3} and 299.75±30.66 kgm^{-3} for Equations 4 and 5 respectively.

The algorithms used to calculate the snow densities in Figure 20 are developed on different basis, it is therefore clear that some are more accurate than others concerning calculations of snow density on sea ice. The density derived from Equation 4 is based on measurements from drifting stations within the Arctic and is therefore expected to show the most accurate snow density. The relationships in Equation 5 and 6 are based on measurements on land where the conditions are different to those at sea, and any correlation with the actual snow density is expected to be lower than for Equation 4. On top of the pack ice however, the weather conditions might be similar to those used as a base for Equations 6, i.e. the cold and dry Canadian Prairies.

According to the European Committee for Standardization (CEN) (2003) the mean snow density for freshly fallen snow is 100 kgm^{-3} while it is about 300 kgm^{-3} for aged snow. When comparing these standardized mean values with the mean values for the calculated densities it

is clear that the density from Equation 6 is not only significantly lower than the other two but also has a significantly lower density than the mean for freshly fallen snow. Since the snow thickness at the location for buoy 5 never exceeds the limit for Pomeroy et al. (1998) of 0.60 m, only Equation 6a is used during the calculations, i.e. the density calculation is solely based on changes in air temperature. This in combination with the significantly low density makes the calculated density values seem unrealistic.

The density values for Equation 4 in Figure 20 display the most significant fluctuations and have a mean value that is somewhere between the mean for freshly fallen snow and settled snow, i.e. 200 kgm^{-3} (CEN, 2003). The mean temperature for buoy 5 is below the threshold of 260.15 K set for Equation 4, meaning that the density is mainly governed by the wind speed. The wind speed is generally increasing through the winter, which is mirrored in the increasing calculated density. The same general increase can be seen in the density derived from Equation 5. The relationship in Equation 5 is also dependent on the snow thickness, which seems to oscillate around the mean of 0.17±0.8 m. The density values for Equation 5 are the highest all through the period. The mean, of close to 300 kgm^{-3}, agrees with the mean value for old snow according to CEN (2003), as well as with the assumed mean snow density for the snow cover in this study (Warren et al., 1999; Markus et al., 2006a).

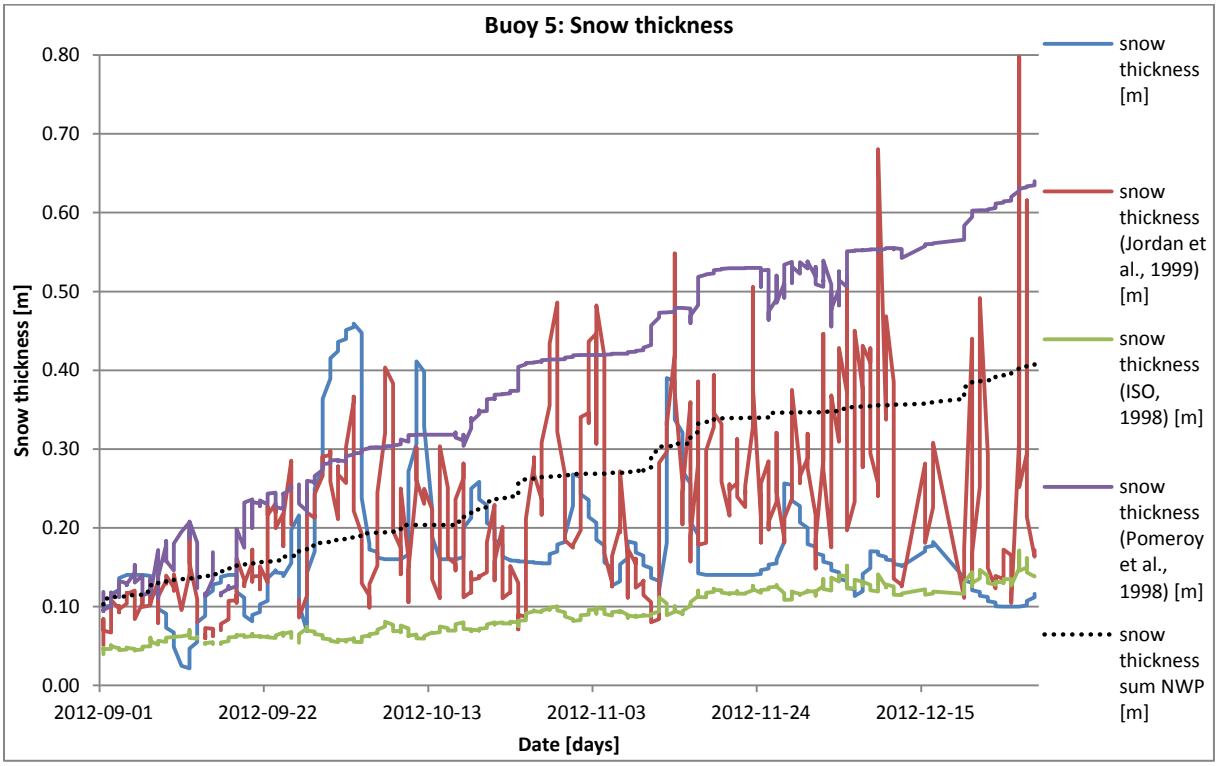

Figure 21. The measured snow thickness for buoy 5 is indicated by a blue line and the calculated and density weighted snow thicknesses based on the densities from Equation 4 Jordan et al. (1999), Equation 5 ISO (1998) and Equation 6 Pomeroy et al. (1998) are indicated by red, green and purple lines respectively. The dotted black line represents the unweighted summed NWP 6h accumulated precipitation.

The resulting snow cover thicknesses, based on the densities from Equations 4-6, are shown in Figure 21, where the measured snow thickness for buoy 5 is compared with the calculated values. The calculated snow cover thickness from Equation 4 in Figure 21 is still the most variable and at the end of the period it displays rapid variations between 0.10 and 0.80 m. Since the density for Equation 5 was so low and the density for Equation 6 so high, the curves

representing the respective snow thickness have now changed places. The snow thickness from Equation 5 is the lowest since, according to calculations, it is so dense and heavy. The snow thickness from Equation 6 on the other hand displays the thickest snow cover and a steady increase during the period due to the significantly low density and general decrease through the measuring period. At the end of the period the snow thickness based on the density calculations of Equation 5 is closest to the actual snow thickness measured by the buoy.

All the densities, in Figure 20, are calculated for the newly fallen snow and no consideration is taken to the already fallen snow or the time dependency of the snow density. Even as the snow is resting on the ground without impact from external forces such as the wind and air temperature the density is increasing as the snow is developing. "The bulk weight density of snow varies. In general it increases with the duration of the snow cover and depends on the site location, climate and altitude" (CEN, 2003). Most land surface models do not consider blowing snow redistribution and sublimation, processes which can alter the difference between accumulated snowfall and snow accumulation by between -40% to +100% in arctic regions (Pomeroy et al., 1998). For future work it would be interesting to study a model where the density calculations is time dependent and the density evolves with time and different geophysical processes.

4.3. Snow-ice interface

The snow-ice interface temperature is evaluated against the 6.9 GHz V channel, in line with the findings of Tonboe et al. (2011), see Figure 22. The theoretical relationship between the snow-ice interface and the 6.9 GHz V channel, Equation 7, is plotted as a straight red line in Figure 22. It differs from the measured values but is close to the one-to-one relationship. The snow-ice interface temperatures measured by the buoys display a high correlation with the low frequency channel, with R^2-values ranging from 0.64-0.94. The highest correlation can be seen for buoy 3. Both horizontal and vertical polarizations have been tested and the correlation for the vertical polarization is strong while it is significantly weak for the horizontal. The reason why the horizontal polarization shows such low correlation is that the horizontal radiation is at a higher rate influenced by horizontal layers in the snowpack, which act like disturbing noise and reduce the correlation. The same can be seen for all low frequencies available in the match-up dataset. The lower satellite frequencies penetrate the snow and ice layer more than the higher frequencies therefore it is expected to see a higher correlation with the brightness temperature from the lower frequencies, such as 6.9 and 7.3 GHz than for example 89 GHz. The 6.9 GHz V channel displays the best correlation with the snow-ice interface of all the available channels. The difference in correlation to 7.3 GHz V is however, very small, 0.01 unit for all the buoys. Since 6.9 and 7.3 GHz are similar in wavelength it was expected to see a strong correlation between the two channels in this study and a small difference when compared to the snow-ice interface temperature. The two channels are perfectly correlated with a R^2-value of 0.99-1, see Figure 23. In the light of this information it is clear that only one of the two channels is needed, at the time, in the upcoming multiple regression analysis.

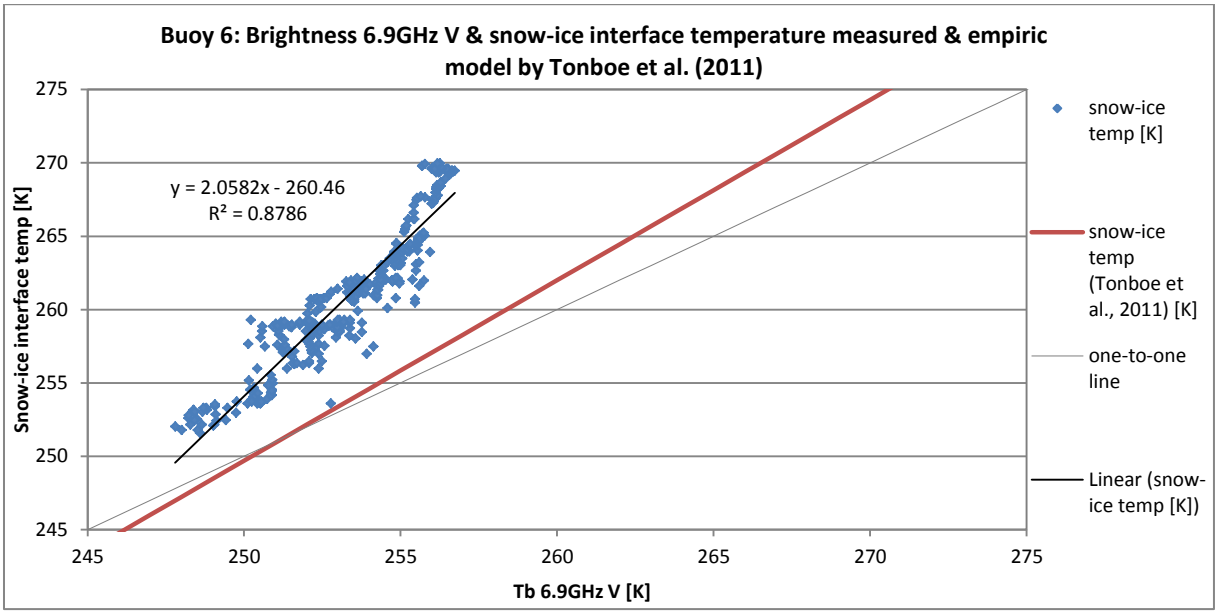

Figure 22. The observed relationship between the snow-ice interface temperature values below 270 K and the AMSR2 6.9 GHz V channel for buoy 6 (2012-09-01 until 2013-01-29) is marked with blue dots in the figure. The relationship has a linear fit (solid black) and the corresponding linear equation and R^2-value of 0.88. The theoretical relationship between the two variables in Equation 7, derived by Tonboe et al. (2011), is displayed as a solid red line. An additional one-to-one line (solid grey) has been inserted as a reference.

The correlation between the snow-ice surface and the 6.9 GHz V channel is low in September as the brightness temperature values vary significantly. This is especially clear when comparing the correlations for the first and second period for buoy 3. During the first winter period, 2012-09-01 until 2013-05-31, buoy 3 displays the highest correlation of all buoys of 0.94 while it for the second period, September-October 2013, does not show any correlation. The low correlation in the beginning of the winter period is likely due to the higher temperatures, i.e. close to the freezing temperature, discussed in Section 4.1.2.

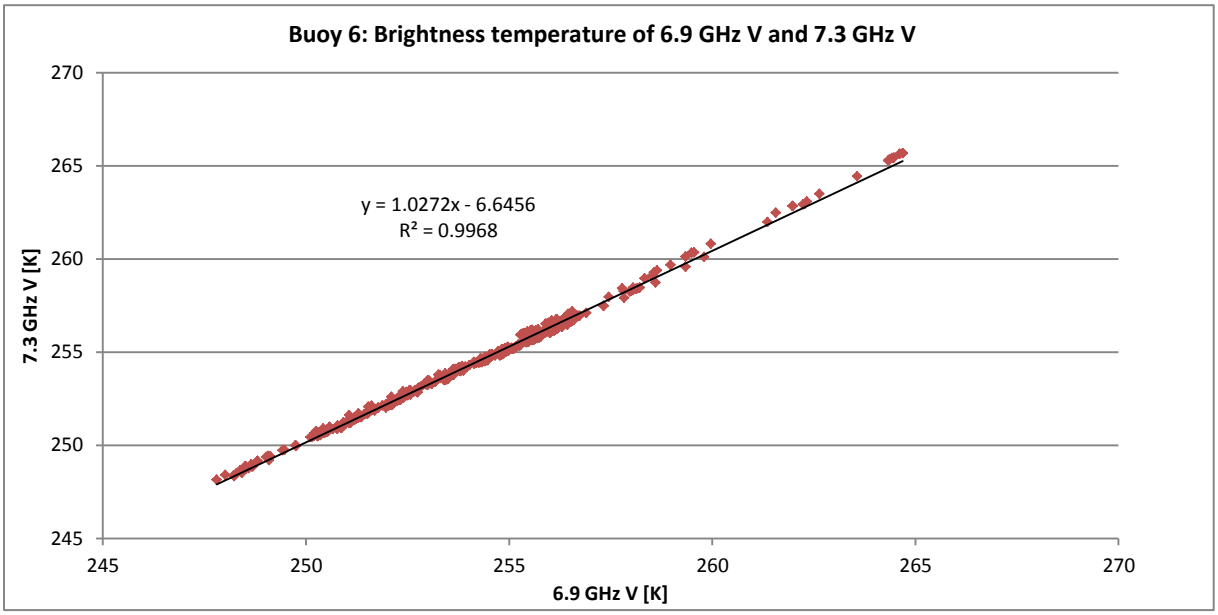

Figure 23. The brightness temperature from AMSR2 channels 6.9 and 7.3 GHz V for buoy 6, with a linear fit as well as linear equation and R^2-value of 1.

4.4. Ice layer

4.4.1. Ice thickness and growth

The ice thickness determines the temperature profile through the ice layer and the ice growth is governed by the air temperature, as well as snow depth and ice characteristics. There may be a time lag between the changes in air temperature and the response in the sea ice thickness. When comparing the buoy air temperatures and the ice thickness for all the buoys, as in Figure 24, there does not seem to be any correlation between cold temperatures and the onset or duration of the bottom sea ice growth and there is no visible time lag.

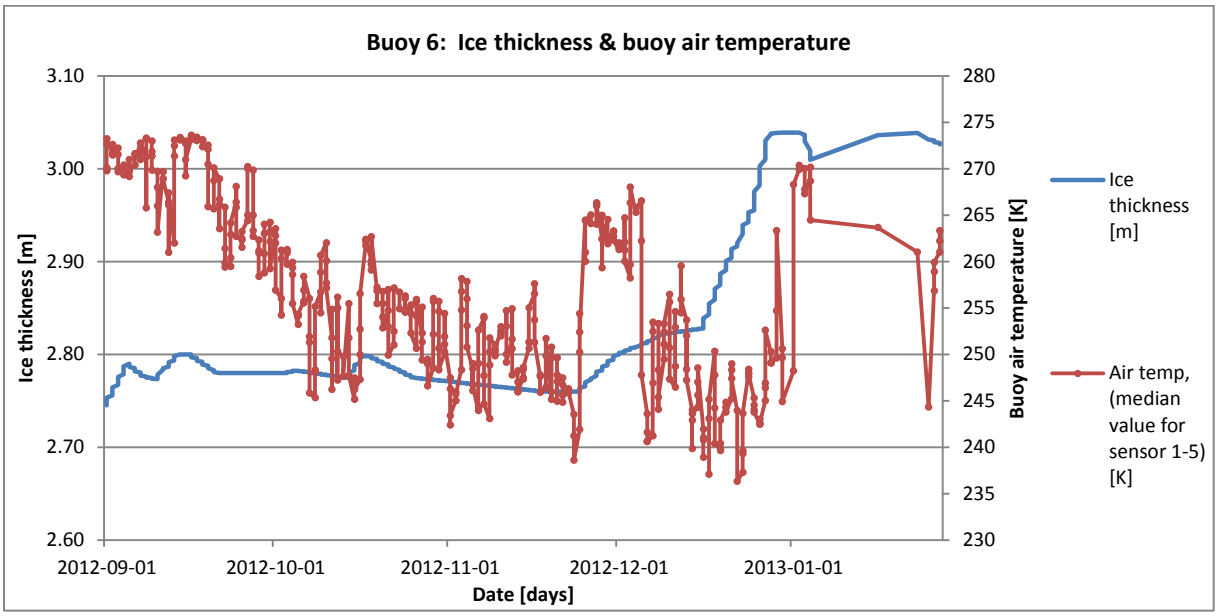

Figure 24. Measured ice thickness in meters (blue line) and air temperature (median value for sensor 1-5) in Kelvin (red line) for buoy 6, during the period 2012-09-01 to 2013-01-27.

The variations in the snow and ice layer thickness are both described by the fluctuations in the depth of the sensors representing the interfaces. It is clear from Figure 25 that the sea ice melt and growth is mainly controlled by the ocean; as the depth of the sensor representing the ice-water interface increases so does the ice thickness and conversely if the sensor depth decreases so does the ice thickness. On the 14th of September there is a possible snow-ice formation event for buoy 6, see Figure 25. As the sea ice thickness increases the sensor depth for the ice-water interface is constant while the sensor depth for the snow-ice interface decreases. Meaning that the sea ice layer expands at the expense of the snow layer. The event is followed by a slight bottom melt, where the sea ice thickness and sensor depth for the ice-water interface both decreases as the sensor depth for the snow-ice interface is constant.

The ocean is the dominant factor when concerning sea ice growth (Eicken, 2003); there is bottom growth on the 24th of November with a significant increase from December until 27th. After the 28th of Decmeber the bottom level is constant and there is some slight variations in the sea ice thickness induced by surface growth and melt. All the buoys show a similar, continuouse increase in sea ice thickness as for buoy 6 between the 16th and 27th of December, but for different periods and lengths of time. This is in line with the study by Perovich et al. (2003); after analysing the data from 135 installed gauges in the Arctic Ocean during 1997-1998, they found that the annual cycle of sea ice thickness was similar on all sites and there was a steady increase in thickness through the winter. The average peak in sea ice growth accourding to Peverich et al. (2003) was found to be around the same time as for buoy 5, at

the 25th of December, see Figure 25. The onset and duration of the periods of continuous ice growth observed in this study was not possible to explain with the available data in the match-up dataset. The most likely explanaition however, is changes in the air and/or water temperature as the ice formation depends on the energy balance and fluxes at the ice-water interface, but no such changes are observed.

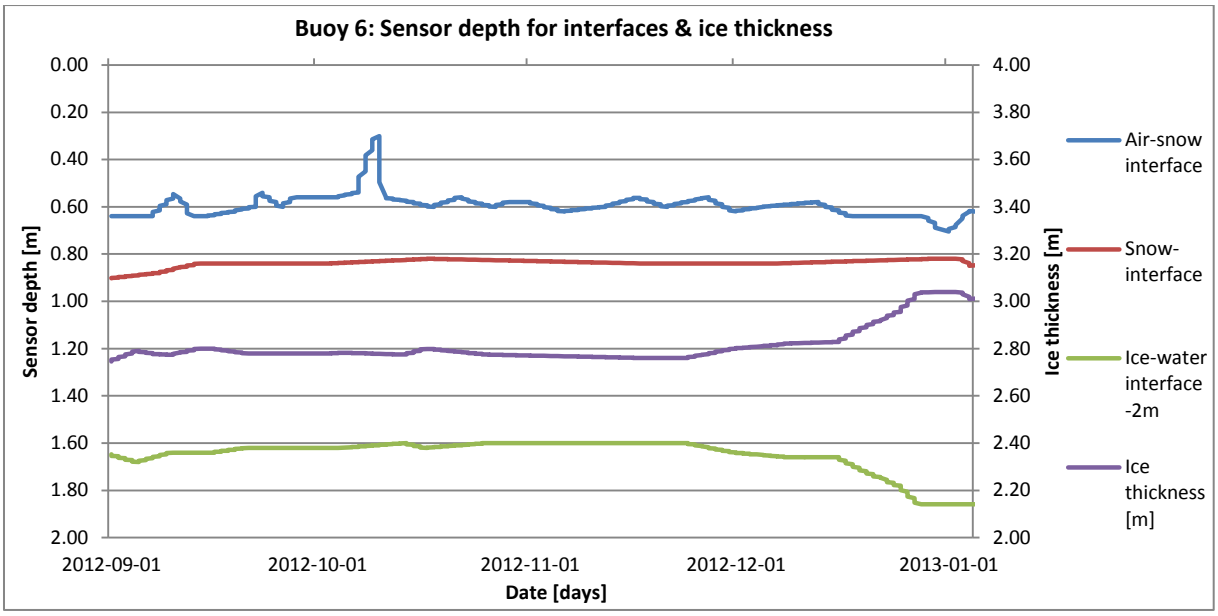

Figure 25. Sensor depths in meters for air-snow interface (blue line), snow-ice interface (red line) and ice-water interface (green line) where 2m have been subtracted to make it easier to visualize. The purple line indicates the measured ice thickness in meters for buoy 6 during the period 2012-09-01 to 2013-01-04.

4.4.2. Theoretical ice thickness

In an attempt of estimating the measured ice thickness, empirical models from Lebedev (1938) (Equation 8), Zubov (1943) (Equation 9) and Maykut (1986) (Equations 10 and 11) are used, see Figures 26 and 27 as well as Appendix E.

According to Maykut (1986) Equation 10 caused a higher sea ice growth than observed, the same conclusion can be drawn in this study as the ice thickness for Equation 10 gives the highest values all through the analysis compared to the measured and the values for Equations 8 and 9. The values for Equation 11 display significant fluctuations, reflecting the variations in the snow cover. The variations in the actual measured values for the sea ice thickness are much smoother. This difference can be explained by the fact that the equation is based on thin sea ice which is more susceptible to changes in snow cover and it is insulating properties. The buoys in this study are deployed on thick multiyear ice, which is not as sensitive to changes in snow cover as the thinner ice. Changes in air temperature and snow cover, at the surface, take time to reach down into the ice and effect the growth of the ice. However, a clear difference in the theoretical sea ice thickness from Equation 11 can be seen between buoy 3 and 6, Figures 26 and 27. The ice thickness for buoy 3 is significantly lower than the measured values and the values calculated from Equations 8 and 9, while as for buoy 6 the values are more similar. This is due to the fact that buoy 3 is deployed on thicker ice than buoy 6, i.e. 3.43-3.99 m versus 2.75-3.04 m, and it recognizes a more variating snow thickness as well as higher average of 0.36 m compared to 0.24 m for buoy 6. It is concluded that for ice as thick as the one at buoy 3 (3.43-3.99m) Equation 11 is inadequate, it does not at all follow the fluctuations

of the actual sea ice thickness and ends up with almost 2m thinner ice than the measured at the end of the season.

The thickness values calculated for Equations 8, 9 and 10 display a similar growing pattern as the actual values, but are unable to capture the full variation. Overall the values for Equation 9 seem to underestimate the sea ice growth at buoy 3, wheras Equation 10 overestimates it. At the end of the period the ice thickness from Equation 8 is the one closest to the real value of 3.95m, Figure 26. The relationship between the measured ice thickness and the Equation 8 prediction for buoy 3 displays a strong correlation of R^2=0.90. Over time for buoy 6 the values for Equation 9 are closest to the measured values as they are the lowest. At the end of the period however, the values for Equation 8 are closest to the actual sea ice thickness.

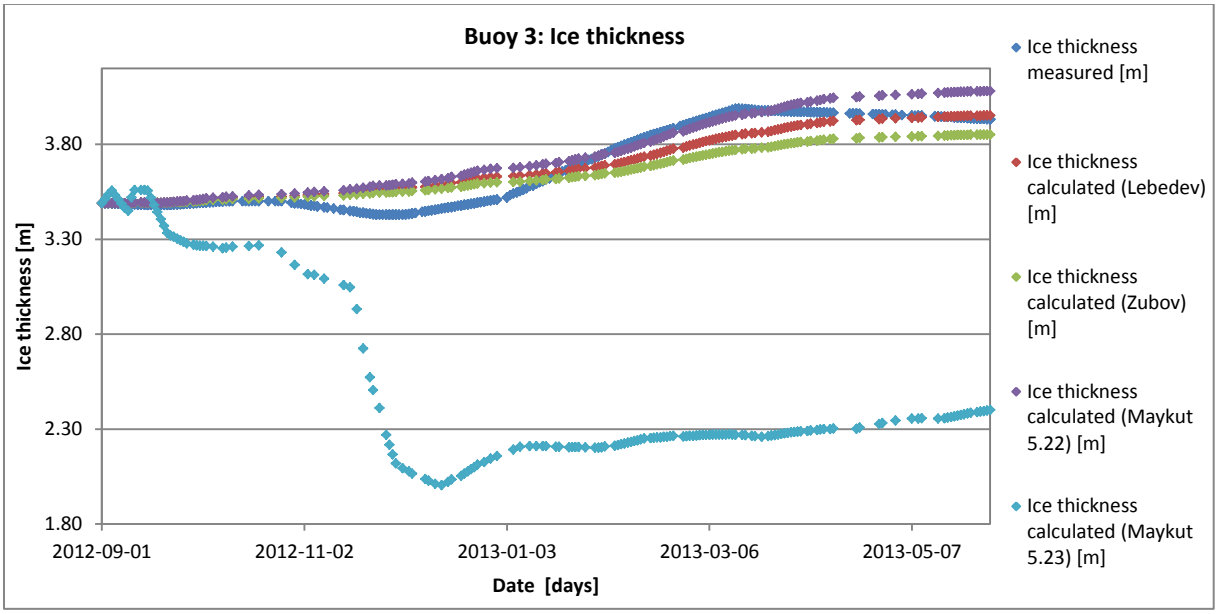

Figure 26. Measured and calculated ice thickness for buoy 3 in meters for the period 2012-09-01 to 2013-05-29. The measured ice thickness is indicated by dark blue dots, ice thickness calculated with the equation of Lebedev (1938) (Equation 8) is indicated with red dots, Zubov (1943) (Equation 9) with green dots, Maykut (1986) 5.22 (Equation 10) with purple dots and Maykut (1986) 5.23 (Equation 11) where the snow thickness is considered with light blue dots.

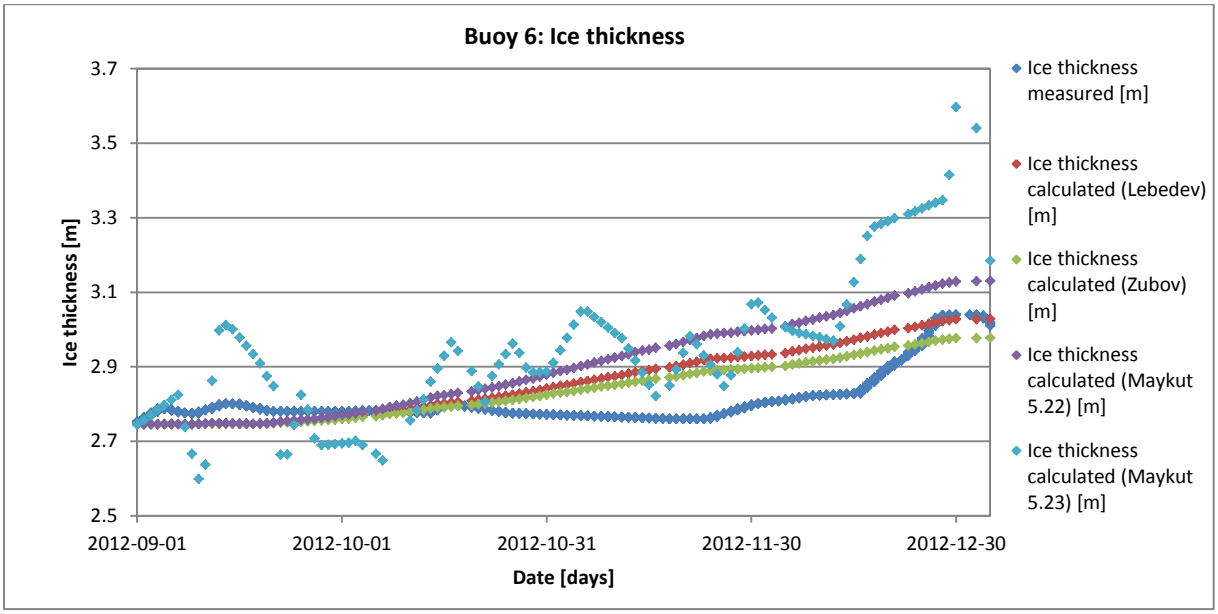

Figure 27. Measured and calculated ice thickness for buoy 6 in meters for the period 2012-09-01 to 2013-01-04. The measured ice thickness is indicated by dark blue dots, ice thickness calculated with the equation of Lebedev (1938) (Equation 8) is indicated with red dots, Zubov (1943) (Equation 9) with green dots, Maykut (1986) 5.22 (Equation 10) with purple dots and Maykut (1986) 5.23 (Equation 11) where the snow thickness is considered with light blue dots.

4.5. Ice-water interface

The ice-water interface has not been given much consideration in this study. The ocean surface temperature is relatively constant during the winter period as the pack ice isolates the water from the cold air above. At the ice-water interface there is a phase transition between solid and liquid phase of water, therefore the temperature will always be at the freezing point. If the temperature goes above the freezing point the ice will melt and if it goes below ice will form. The ice-water interface temperature is therefore set to a constant value of 271.35 K in this study, according to the observations at the location of the IMB buoys, see Figure 11.

4.6. Multiple regression analysis

To be able to reproduce the temperature profile through the snow and ice layers a multiple regression analysis is performed. As the physical parameters and the measured temperature profile down through the snow and ice are studied an important knowledge base is created, so that it is possible to accurately choose the variables for the analysis. The variables chosen are based on the previously obtained results in this study, a correlation analysis (see Appendix F) and direct visible changes in the statistics of the regression analysis. When manually choosing the variables it is important to consider the standard deviation and actively remove the variables exceeding it.

A wide range of combinations of channels are used to try and find the best fit for the measured temperature profile for buoy 3. Table 1 summarizes the chosen combinations of channels, resulting in Equations 12-19, for the different depths in the snow and ice layer. Two combinations are chosen for both the air-snow interface and the snow mean temperature depth, one with and one without TIR.

Depth	Channels	Number of measurements	R^2-value	Standard error [K]
Air-snow interface	7.3 GHz V 10 GHz V 89 GHz H	488	0.79	4.16
Air-snow interface	TIR 7.3 GHz V 89 GHz V	178	0.91	3.12
Snow mean	TIR 89GHz H SMOS 25-35 V SMOS 40-50 V	178	0.93	1.99
Snow mean	7.3 GHz V 10 GHz V 89 GHz H SMOS 40-50 V	488	0.89	2.36
Snow-ice	6.9 GHz V 10 GHz V SMOS 40-50 H	488	0.94	1.36
0.1 m into the ice	6.9 GHz V 10 GHz V SMOS 40-50 H	488	0.97	1.00
0.3 m into the ice	6.9 GHz V 10 GHz V SMOS 40-50 H	488	0.98	0.79
0.5 m into the ice	6.9 GHz V 10 GHz V SMOS 40-50 V	488	0.98	0.71

Table 1. Statistics summary of the chosen channel combinations derived through the multiple regression analysis.

$$T_{air-snow} = 2.93 * Tb_{7.3V} - 1.46 * Tb_{10V} + 0.58 * Tb_{89H} - 239.60 \quad (12)$$

$$T_{air-snow} = 0.60 * TIR + 0.53 * Tb_{7.3V} + 0.36 * Tb_{89V} - 106.22 \quad (13)$$

$$T_{snow} = 0.48 * TIR + 0.26 * Tb_{89H} + 0.24 * Tb_{SMOS\,25-35V} + 0.36 * Tb_{SMOS\,40-50H} - 64.70 \quad (14)$$

$$T_{snow} = 3.29 * Tb_{7.3V} - 1.77 * Tb_{10V} + 0.34 * Tb_{89H} - 0.29 * Tb_{SMOS\,40-50V} - 130.58 \quad (15)$$

$$T_{snow-ice} = 1.70 * Tb_{6.9V} - 0.32 * Tb_{10V} + 0.11 * Tb_{SMOS\,40-50H} - 118.75 \quad (16)$$

$$T_{0.1m\,ice} = 2.36 * Tb_{6.9V} - 1.13 * Tb_{10V} + 0.07 * Tb_{SMOS\,40-50H} - 74.32 \quad (17)$$

$$T_{0.3m\,ice} = 2.97 * Tb_{6.9V} - 1.90 * Tb_{10V} + 0.04 * Tb_{SMOS\,40-50H} - 27.10 \quad (18)$$

$$T_{0.5m\,ice} = 3.36 * Tb_{6.9V} - 2.35 * Tb_{10V} - 0.04 * Tb_{SMOS\,40-50V} + 5.49 \quad (19)$$

The equations are used to calculate new temperature values for each and every one of the chosen levels in the snow and ice layers, i.e. the air-snow interface, snow mean, snow-ice interface, 0.1 m, 0.3 m and 0.5 m into the ice. The equations based on TIR, i.e. Equations 13 and 14, have very few measurement points. The amount of data points are lowered even more when only considering temperature values below 270 K, which results in 276 comparable data points for Equation 13 and 178 for Equation 14. This can be compared to the number of available data points for Equations 12 and 15, without TIR, of about 600.

The measured and calculated values for the mean snow temperature (Equation 15) and 0.5 m into the ice (Equation 19) are shown in Figure 28 and 29 respectively. The relationship between the snow mean temperatures, in Figure 28, has a R^2-value of 0.93 while the relationship for the 0.5 m into the ice temperatures has a R^2-value of 0.94, Figure 29. The empirical model for 0.1 m into the ice displays the strongest correlation after which the goodness of fit for the models decreases both upwards and downwards in the snow and ice layers. The models are always close to the one-to-one relationship between measured and calculated, but with more or less spreading of the data points.

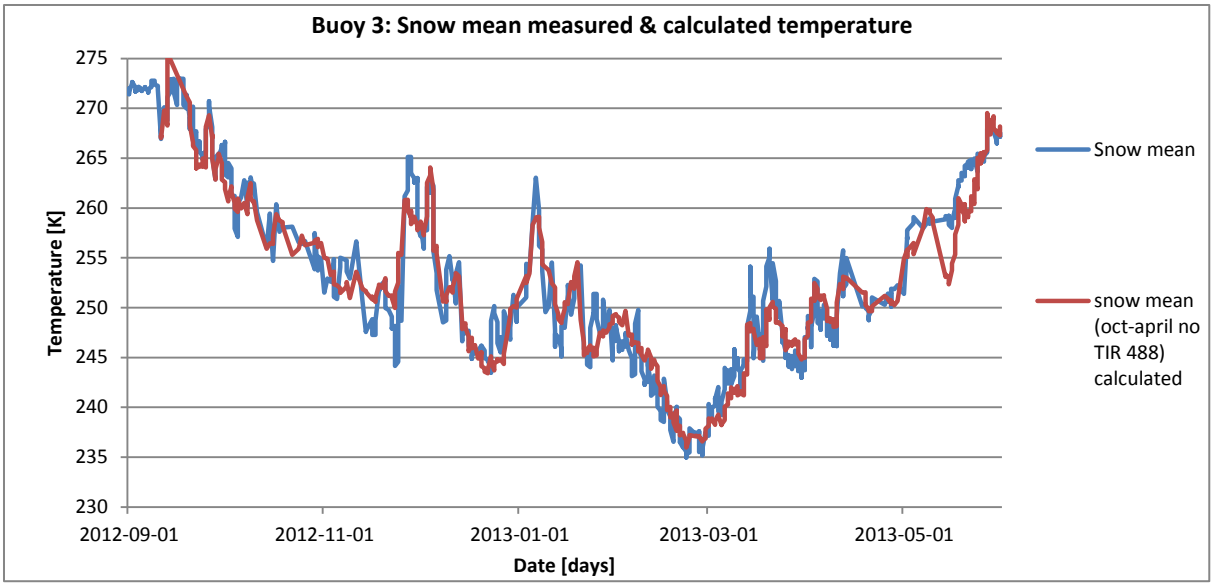

Figure 28. The measured (blue) and calculated (red) temperature values for the snow mean (Equation 15), for buoy 3, for the full winter period 2012-09-01 until 2013-05-31. For measured values exceeding 270 K no temperature calculations are made.

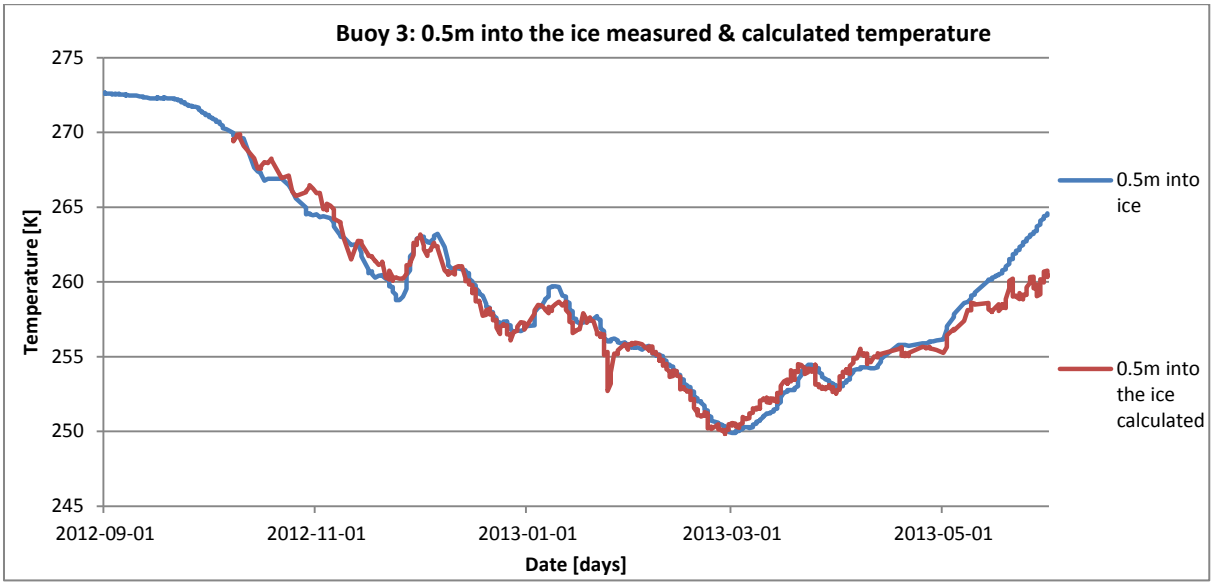

Figure 29. The measured (blue) and calculated (red) temperature values for 0.5 m into the ice (Equation 19), for buoy 3, for the full winter period 2012-09-01 until 2013-05-31. For measured values exceeding 270 K no temperature calculations are made.

4.7. Model comparison

Once again note that measurements above 270 K are removed from the control analysis due to the sensitivity of the satellites to changes in the snow emissivity associated with melting processes.

Level depth (Equation)	R^2-value buoy 4	R^2-value buoy 5	R^2-value buoy 6
Air-snow interface (12)	0.61	0.55	0.54
Air-snow interface (13)	0.51	0.46	0.43
Snow mean (14)	0.65	0.55	0.53
Snow mean (15)	0.77	0.74	0.69
Snow-ice interface (16)	0.76	0.54	0.86
0.1 into the ice (17)	0.79	0.51	0.90
0.3 into the ice (18)	0.75	0.45	0.90
0.5 into the ice (19)	0.81	0.45	0.90

Table 2. The R^2-values when comparing the measured and calculated temperature values, for all the chosen depths in the snow and ice layer for buoy 4-6. The calculated values are according to Equations 12-19.

To evaluate the goodness of fit of the models the coefficients, retrieved in the regression analysis, for buoy 3 are applied to buoy 4-6 as a control. New temperature values are calculated for all the depths through the snow and ice layer, for all the buoys. The measured

temperature values are then compared with the actual measurements see Figures 30-39, the resulting R^2-values can be seen in Table 2. The correlation is weaker for the top layers than for the lower layers deeper into the snow and ice. This can be explained by the higher standard error for the top most layers for buoy 3 in the regression analysis as well as the large temperature fluctuations on the surface by the significantly varying air temperature. The temperature changes are difficult to capture by the satellite sensors, which has been observed in this study (e.g. Figure 15). The satellites generally give a smoothened temperature curve. The empirical models from the regression analysis are based on the temperature variations of buoy 3 which may be significantly different to those of buoy 4-6. Therefor it is expected to see a lower correlation for the top most layers. The fact that the correlation for the snow mean temperature (Figures 32 and 33) is relatively low can also be due to the assumption, made in this study, of a linear temperature profile through the snow. This may not always be the case since the snow cover is insulating the sea ice, delaying the temperature shifts observed in the air temperature, and creating a nonlinear temperature profile.

Buoy 5 displays the overall weakest correlation. Buoy 4 displays the strongest correlation for the air-snow interface and snow mean (Figures 30-33), while buoy 6 displays the strongest correlation for the lower levels, i.e. snow-ice interface down to 0.5 m into the ice (Figures 34 and 35). The differences in correlation can be explained by the spatial distribution of the buoys, their individual drift tracks and the snow and ice thickness at the locations for buoy 4-6 compared to that of buoy 3. Buoy 5 is the last deployed buoy, of the chosen four, while buoy 3 is the first. This means that the geographical distance is greatest between buoy 3 and 5, see Figure 10, indicating that the models could have a spatial dependency. Buoy 5 is drifted rapidly through Fram Strait and reached the spatial limit of 80°N well before buoy 3, i.e. in December 2012 compared to October 2013. The ice located at the deployment site for buoy 5 is significantly thinner than that of buoy 3, and so is the snow cover, see Table 3 and Appendix A. The snow and ice thickness is thinnest for buoy 5, 0.17 m and 1.40 m respectively, while it is thickest for buoy 3, 0.36 m and 3.71 m respectively. This means that the heat flux between the ocean and atmosphere is significantly different at the two locations. The flux is much stronger for buoy 5 and weaker for buoy 3 as the thick snow and ice are insulating. As the models are created for the situation of a thick snow and ice cover and a low heat flux, they are likely to be less suitable for the conditions at the location for buoy 5 which explains the generally lower correlation.

The correlation for buoy 4 is generally high and it is the buoy deployed closest to buoy 3. Buoy 4 has a much shorter measuring period and has a higher drift velocity than buoy 3 but the two buoys took the same route as they rounded the north east corner of Greenland. This increases the confidence that the models have a spatial dependency. Buoy 4 displays however, a lower correlation for the deeper levels into the ice (Figure 37) than buoy 6. This is explained by the fact that the ice thickness for buoy 6 is over 1 m thicker than that of buoy 4, and closest to the thickness of buoy 3.

Buoy	3	4	5	6
End of measuring period	Oct 2013	April 2012	December 2012	January 2012
Average snow thickness	0.36	0.22	0.17	0.24
Average ice thickness	3.71	1.68	1.40	2.81

Table 3. An overview of the average snow and ice thicknesses at the deployment sites for the different buoys, as well as month and year when the buoy reached the spatial limit of 80°N.

The models using TIR has a weaker correlation with the actual values than the models not using TIR, this can be seen in Table 2 as well as Figures 30-33. The calculated values in

Figure 31 and 32 are more dispersed than the calculated temperature values in Figure 30 and 33. This is likely due to cloud errors; is it difficult to detect clouds and as a result the TIR dataset contains measurements where the surface temperature has been mixed with the temperature of the cloud tops. This gives a much colder temperature of the surface than the actual temperature value. The calculated values for the snow-ice interface in Figure 34 capture the variations in the actual temperature very well. The strongest correlation can be seen in Figure 35 at a depth of 0.1 m into the ice calculated for buoy 6, which has a R^2-value of 0.90. The calculated values for buoy 5 are less accurate, see Table 2 and Figure 36. Although there is an increasing gap between the measured and calculated temperature values for buoy 4 as the depth into the ice increases, the correlation is high. The calculated values are able to capture the fluctuations in the measured temperature, see Figures 37-39.

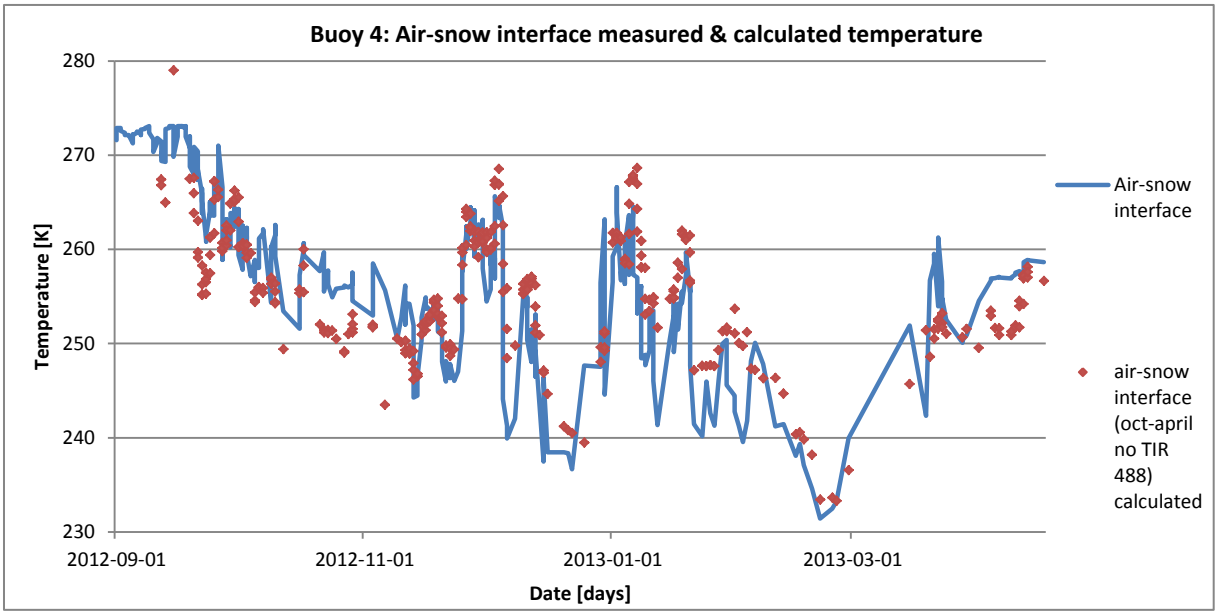

Figure 30. The measured (blue line) and calculated (red dots) temperature values for the air-snow interface (Equation 12), for buoy 4 over the period 2012-09-01 until 2013-04-17.

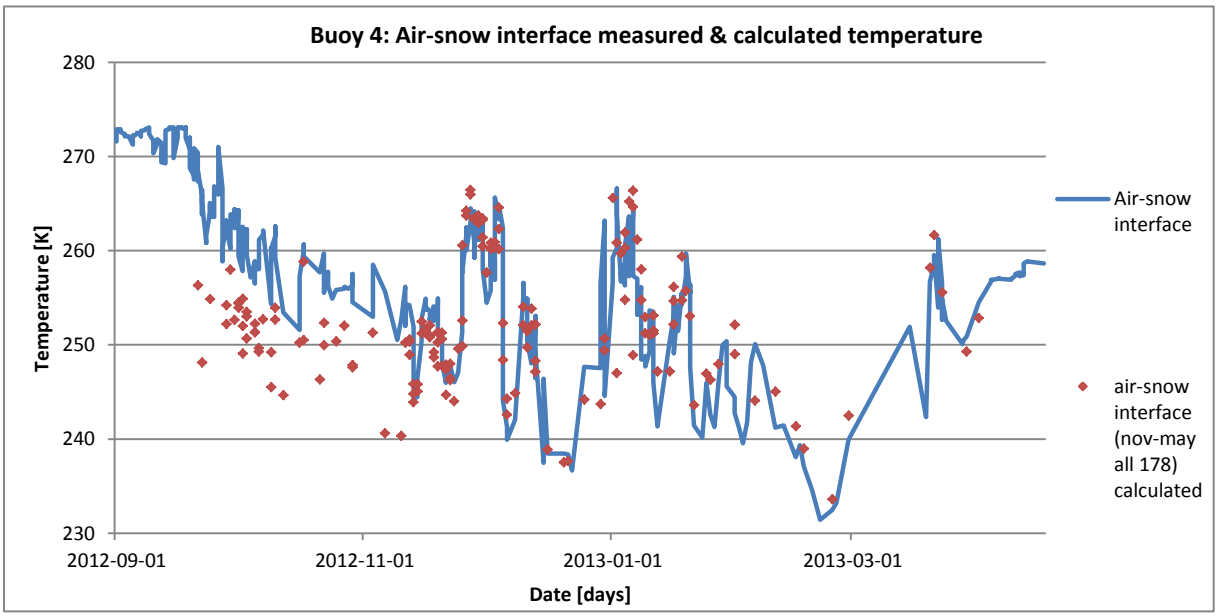

Figure 31. The measured (blue line) and calculated (red dots) temperature values for the air-snow interface (Equation 13), for buoy 4 over the period 2012-09-01 until 2013-04-17.

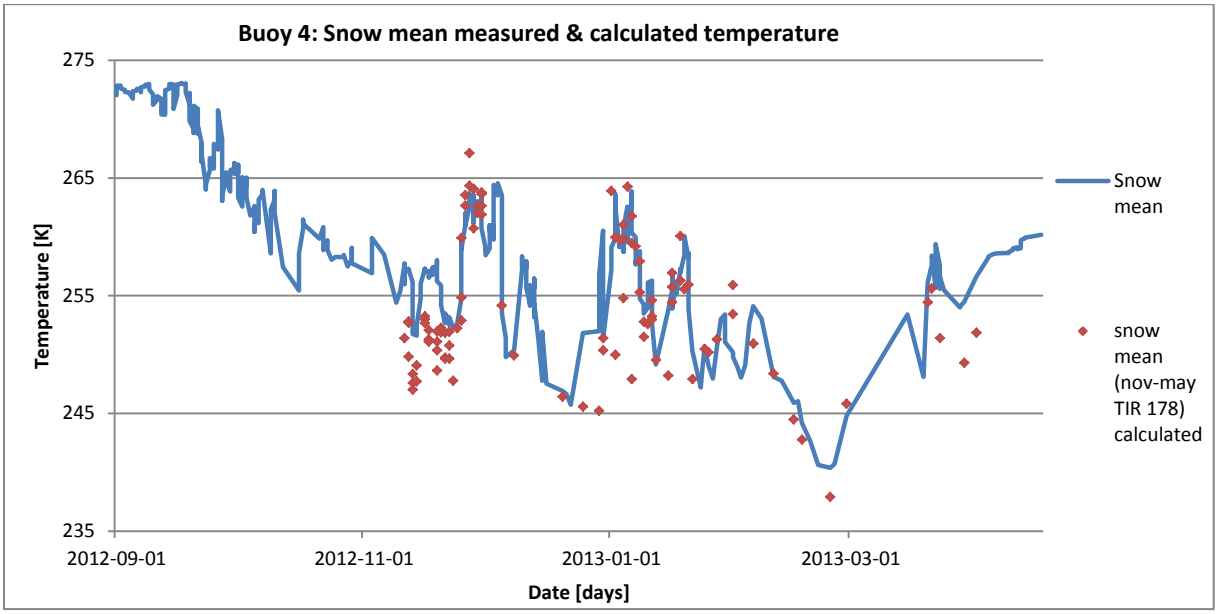

Figure 32. The measured (blue line) and calculated (red dots) temperature values for the snow mean (Equation 14), for buoy 4 over the period 2012-09-01 until 2013-04-17.

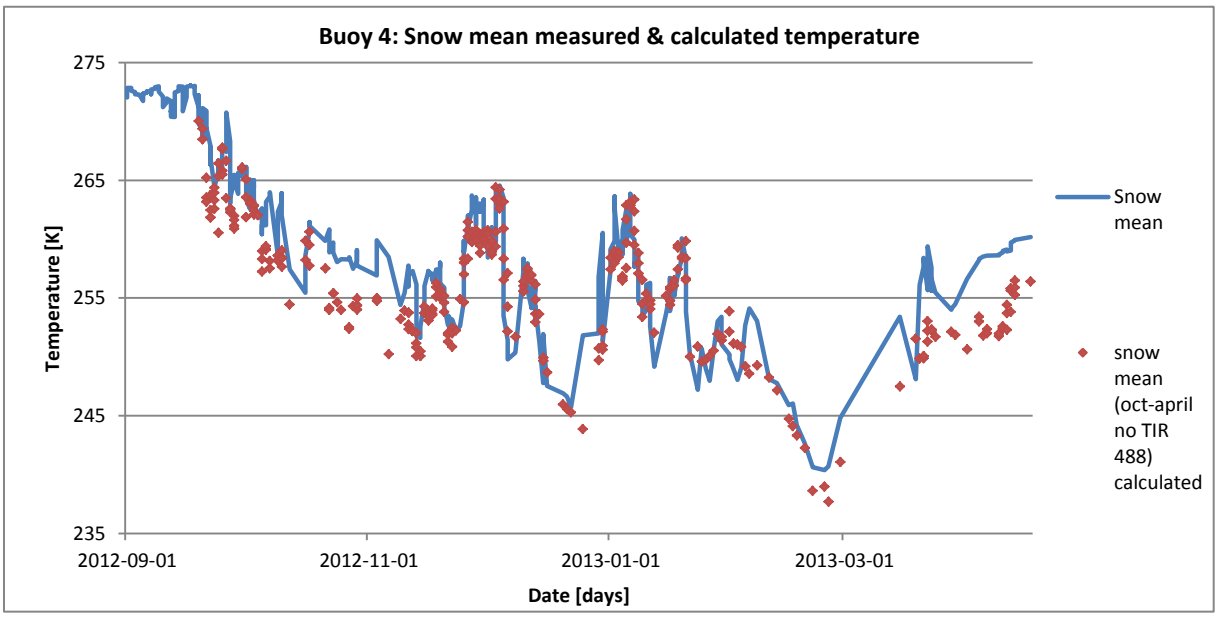

Figure 33. The measured (blue line) and calculated (red dots) temperature values for the snow mean (Equation 15), for buoy 4 over the period 2012-09-01 until 2013-04-17.

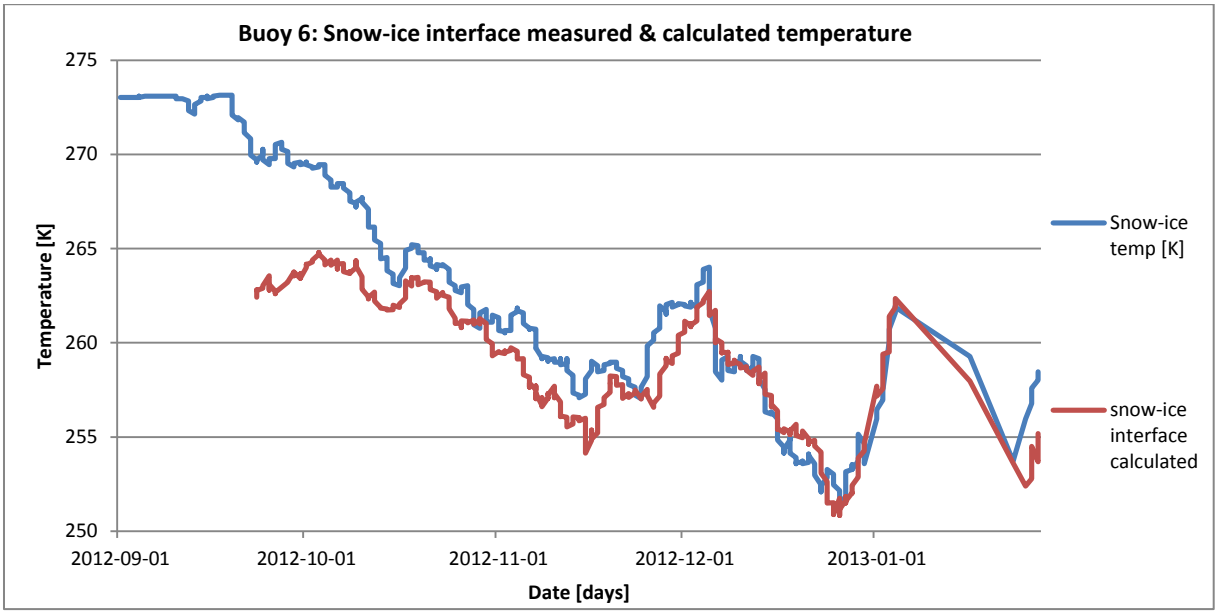

Figure 34. The measured (blue) and calculated (red) temperature values for the snow-ice interface (Equation 16), for buoy 6 over the period 2012-09-01 until 2013-01-27.

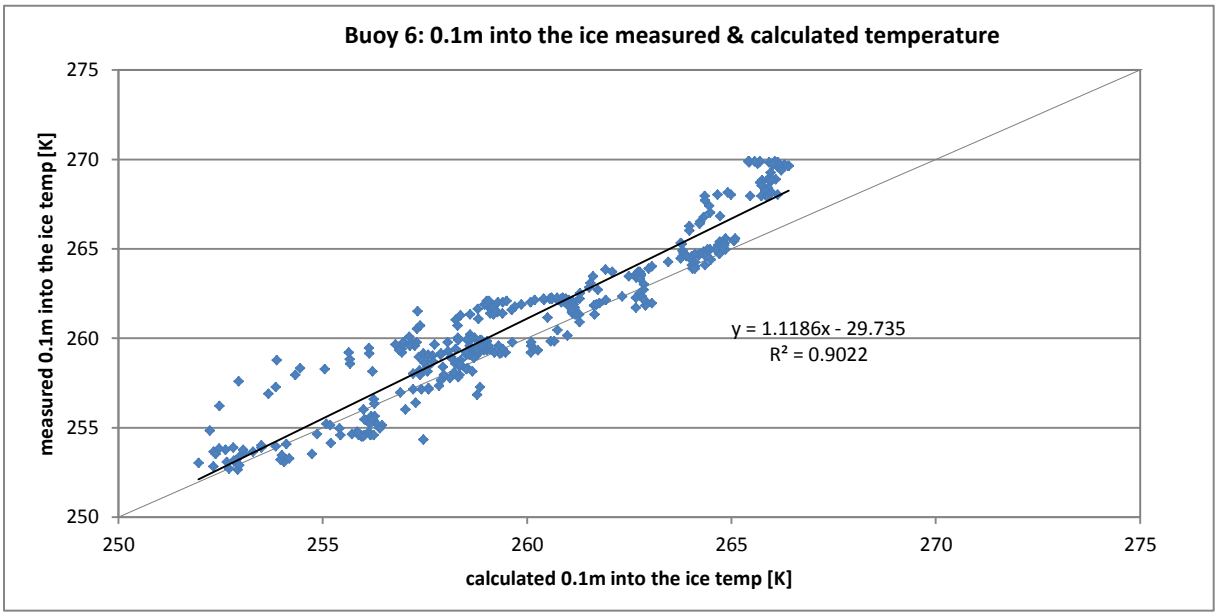

Figure 35. The measured and calculated (Equation 17) temperature values for 0.1 m into the ice, for buoy 6 from 2012-09-01 until 2013-01-27. In the figure a one-to-one reference line (grey) are inserted as well as a linear fit (black) with the corresponding linear equation and R^2-value of 0.90.

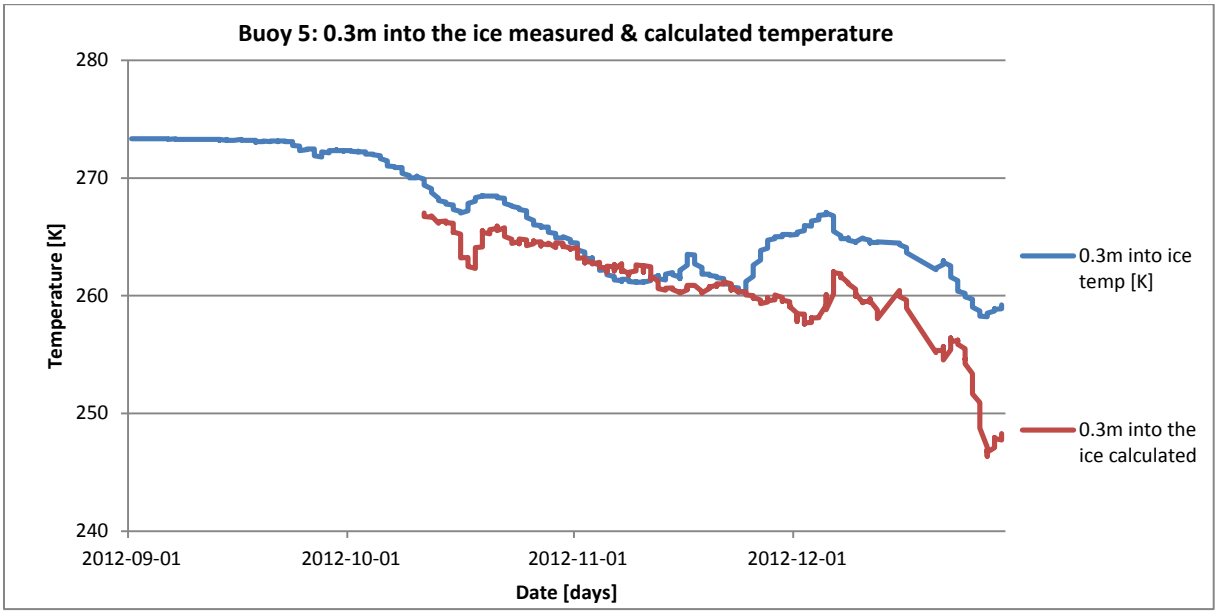

Figure 36. The measured (blue) and calculated (red) temperature values for 0.3 m into the ice (Equation 18), for buoy 5 over the period 2012-09-01 until 2013-12-29.

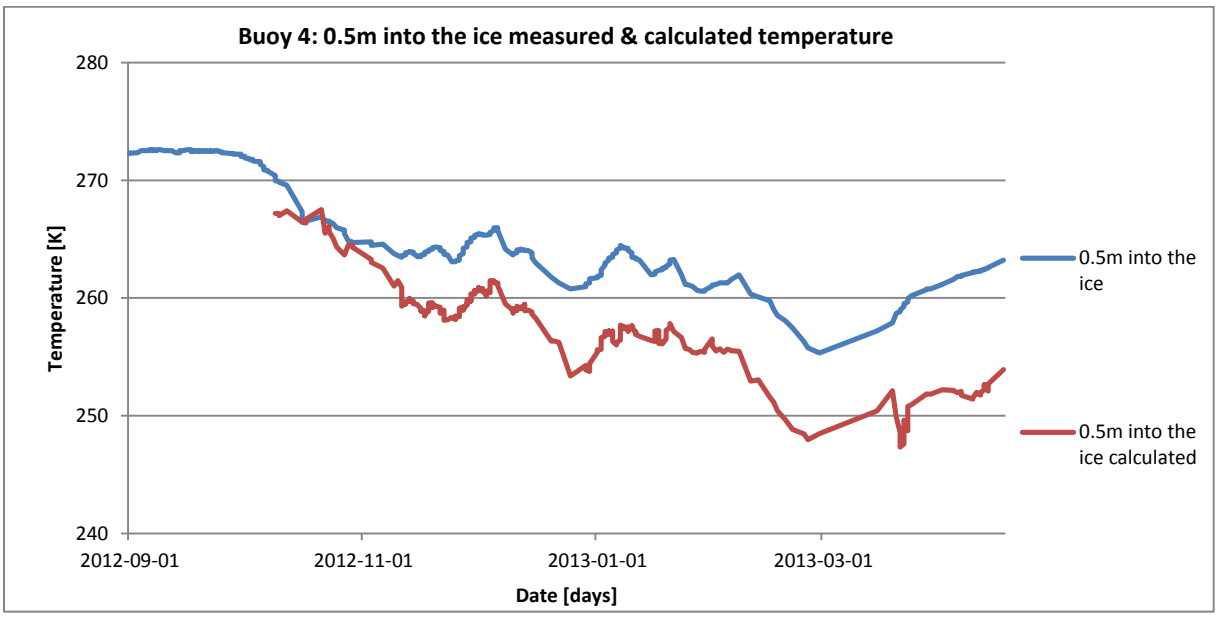

Figure 37. The measured (blue) and calculated (red) temperature values for 0.5 m into the ice (Equation 19), for buoy 4 over the period 2012-09-01 until 2013-04-17.

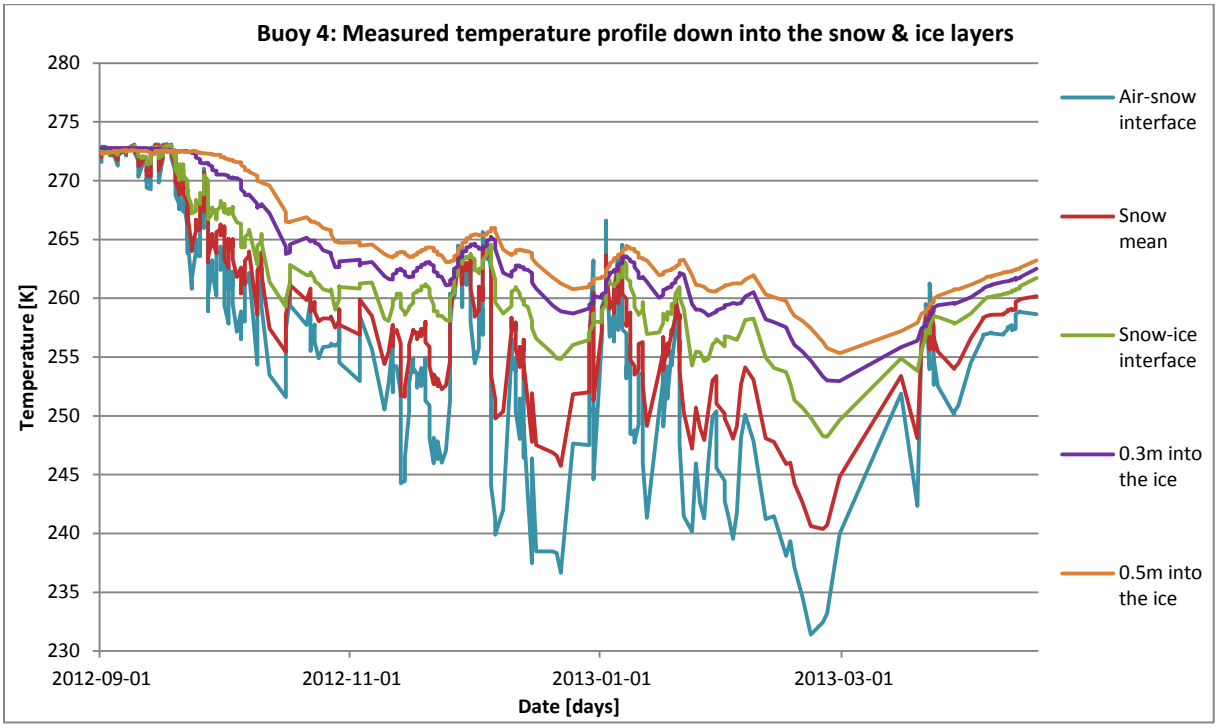

Figure 38. The measured temperature profile down into the snow and ice layers for buoy 4 over the period 2012-09-01 until 2013-04-17.

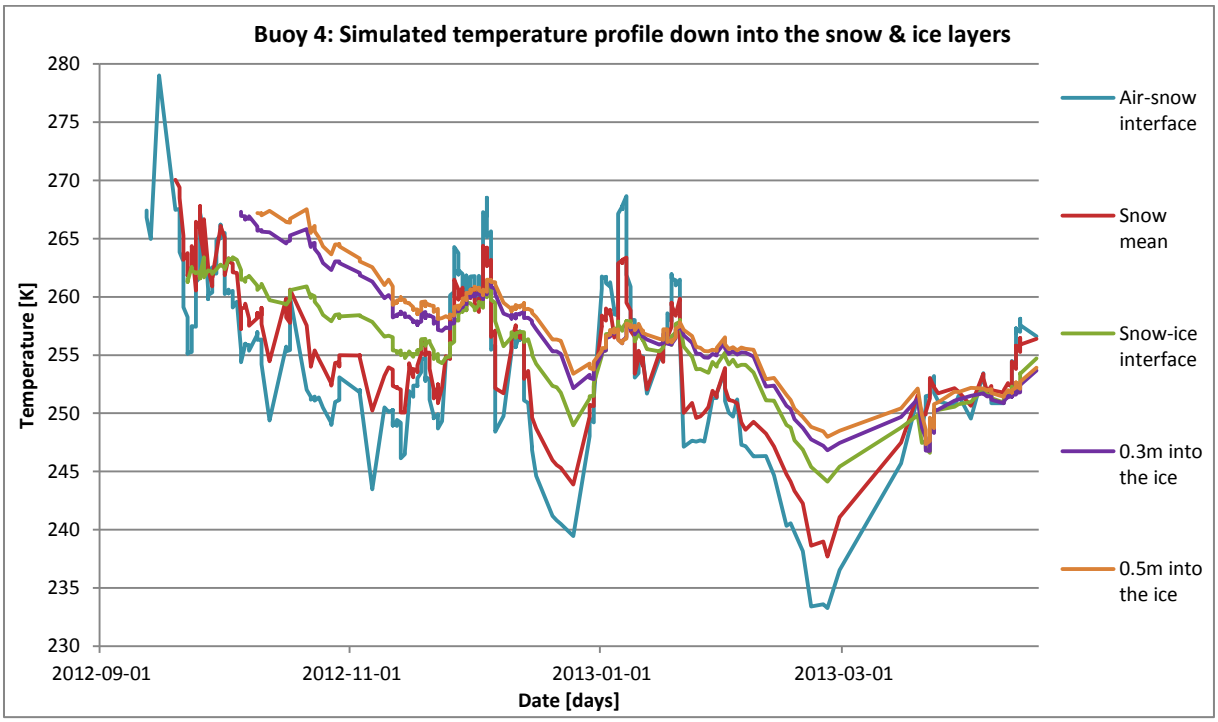

Figure 39. The simulated temperature profile down into the snow and ice layers for buoy 4 over the period 2012-09-01 until 2013-04-17.

5. Summary and Conclusions

The objective of this project is to examine the possibility to derive the temperature profile through the snow and ice layers (see Figure 1) from a combination of available satellite data, such as thermal infrared and microwave radiation at different wavelengths and polarisations. The combined dataset, of IMB, NWP and satellite data, are analysed for possible and theoretically derived relationships between the satellite measurements and different snow and ice parameters.

The accuracy of the modelled NWP data is confirmed as the 2m air temperature is compared with the IMB measured air temperature and shows a significant however smoothening, correlation. The correlation gets weaker as the temperature fluctuations increases in strength during the winter period. The major fluctuations are also difficult for the satellite sensors to capture. It is shown that the surface and air temperatures are not always connected to the thermal microwave radiation. The correlation is generally significantly weaker for the satellite data during periods of high temperatures, close to the freezing temperature. The TIR data displays the highest correlation to the surface temperature, of all the satellite channels, with an R^2-value of about 0.69, though data is sparse due to cloud cover.

The properties of the snow layer govern the heat flux between the ocean and atmosphere, determining the penetration depth for the satellite sensors and thereby altering the brightness temperature. In this study the temperature profile through the snow is assumed to be linear, as a simplification based on the result of the observed buoy profiles. To get the, so called, measured mean snow temperature the mean value of the air-snow and snow-ice interface is calculated. The calculated snow emissivity, of 0.75-0.80, is in line with the findings of Mathew et al. (2008) and Tonboe (2010), as are the calculated values for spectral gradient ratio and polarization ratio. Future work would include improved calculations of snow emissivity, to better capture the natural variations, and to be able to get the actual temperature from the satellites.

When studying the measured snow thickness significant drops are observed right after periods of heavy snowfall and increases in snow thickness, which are likely due to some form of wind driven metamorphosis. As the events are compared to the NWP data however, no clear explanation can be found. There is no observed correlation between the measured snow events and periods of predicted precipitation. This is likely due to the fact that the NWP precipitation data is accumulated over 6h as well as the large spatial resolution of the NWP model, i.e. 80 km. When summing the NWP 6h accumulated precipitation it is about 0.30 m higher than the thickness measured by the buoy at the end of the measuring period. This indicates that there are external or internal forces working on the snow so that it is transformed or removed from the buoy location over time. In an attempt to reproduce the measured snow thickness values, from the summed NWP 6h accumulated precipitation, empirical models for snow density are used, Equations 4-6. The result closest to the actual average value is given by ISO (1998), Equation 5, with a density of about 300 kgm^{-3}. For future work it would be interesting to study a model where the snow density calculations are time dependent, and the density evolves with time and different geophysical processes, to better estimate the actual snow thickness. The expectation is that this will assist in the explanation of the sharp drops in the snow thickness.

Comparisons of the snow-ice interface temperature with satellite brightness temperatures shows that the low frequency channels have a stronger correlation than the high frequencies. The overall strongest correlation can be found for AMSR2 6.9 GHz vertical polarization, with R^2-values of 0.64-0.94. The difference to AMSR2 7.3 GHz V is however, very small and the two channels displays a near perfect one-to-one relationship.

For all the buoys, though a period of continuous sea ice growth is observed during the winter period, the onset and duration of the growth periods vary and can not be explained by the available data in the match-up dataset. In an attempt to estimate the measured sea ice thickness, empirical models from Lebedev (1938), Zubov (1943) and Maykut (1986) are used, see Equations 8-11 and Figures 26 and 27. It is concluded that Equation 11 is unsuited for thick ice, such as for buoy 3, as it underestimates the actual ice thickness by almost 2m. The remaining three equations give similar values of sea ice thickness, though Equation 8 is closest to the actual value for the majority of the buoys. It is however, concluded that the relationship for the sea ice thickness is more complex than can be described by the simple relationships in Equations 8-11. If more time would have been assigned for this thesis, further studies would include more advanced models for sea ice thickness. It would also include a study of the empirical model by Tonboe (2003) for thickness calculations through the distinct heat capacity of the snow and ice layers (Equation 3.4, Tonboe, 2003).

After analysing all the levels down through the snow and ice layers it is possible to choose satellite variables suitable for the multiple regression analysis on buoy 3, for the period 2012-10-01 to 2013-04-29. The temperatures above 270 K are removed from the analysis and control due to the sensitivity of the satellite sensors to changes in snow emissivity caused by melting processes in the snow and ice layers. The manual variable selection is additionally based on a correlation analysis, see Appendix F, and visual interpretation of the regression statistics. One equation for each level in the snow and ice layers is derived, except for the air-snow interface and mean snow where there are two models, one with and one without TIR, Equations 12-19. The certainty is greater for the lower levels in the ice and best for the 0.5 m into the ice level with a R^2-value of 0.98 and standard error of 0.71, see Table 1.

The derived empirical models are tested in a control run conducted on buoys 4-6, Figures 30-37, and display R^2-values ranging from 0.43 to 0.90, see Table 2. It is evident that the models without TIR are superior to those including TIR measurements. This is likely due to cloud errors; is it difficult to detect clouds and as a result the TIR dataset contains measurements where the surface temperature has been mixed with the temperature of the cloud tops. It is also seen that the correlation for the top most layers in the snow and ice column are weaker than for the lower levels. This is a result of the higher standard error for the models for the upper levels in the regression analysis as well as the significant fluctuating surface air temperature, which is difficult for the satellite sensors to capture. The relatively low correlation for the mean snow temperature may also be as a response to the assumption of a linear temperature profile through the snow layer. Buoy 5 displays the overall weakest correlation. While buoy 4 displays the strongest correlation for the air-snow interface and snow mean (see Figures 38-39), buoy 6 displays the strongest correlation for the lower levels in the ice. The differences in correlation can be explained by the spatial distribution of the buoys, their individual drift tracks and the snow and ice thickness at the locations for buoys 4-6 compared to that of buoy 3. The models are created for the conditions similar to those at the buoy 3 location, i.e. relatively thick snow and ice layers.

The empirical models derived in the regression analysis, in this study, show a large variation in certainty. Buoy 5 is significantly decreasing the reliability of the models. It is however, the

buoy deployed furthest away from buoy 3 and the buoy displaying the largest difference concerning snow and sea ice thickness, as it is relatively thin. It is debated whether the models developed in this study are sufficiently robust to use for evaluation of, and possibly assimilation in, sea ice models, replacing climatological data, since the correlation is not yet high enough. To further improve the models and increase the reliability, future studies would include a larger spatial area and time frame for evaluating the models. To be able to generalize it would be necessary to look at information from more IMB buoys separated by both time and space. It would be of interest to look at different climatological datasets and evaluate the models for the entire Arctic region. Future work would also include the usage of a more advanced regression analysis. To better evaluate which variables to use in the analysis a stepwise regression model would be used, where the choice of variables were automated. It would also be of interest to perform the regression analysis on buoys 4-6 as well, both independently of the analysis already performed and for the specific channels already chosen for buoy 3. The coefficients of the different buoys would then be compared to see how much they deviate from each other.

Acknowledgements

This master thesis was conducted at the department of Physical Geography and Ecosystem Science at Lund University in collaboration with the section for Climate and Arctic at Danish Meteorological Institute. The data in this study was provided by the Danish Meteorological Institute, the Technical University of Denmark and the University of Bremen.

I take this opportunity to express my gratitude to my external supervisors at Danish Meteorological Institute, Gorm Dybkjær, Leif Toudal Pedersen and Rasmus Tonboe from the section for Climate and Arctic, at DMI. I am extremely thankful to them for letting me conduct this project and for guiding me through it. I am indebted to them for sharing expertise and providing me with valuable comments and inspiration.

A special thanks to my supervisor Paul Miller at the department of Physical Geography and Ecosystem Science, Lund University, for the constructive criticism, valuable discussions and encouragement along the way.

I am also grateful to all of those who otherwise directly or indirectly have helped and supported in the process of this thesis.

6. References

Andersen S., Tonboe R., Kaleschke L., Heygster G., and Pedersen L. T.; Intercomparison of passive microwave sea ice concentration retrievals over the high-concentration Arctic sea ice, 2007. *Journal of Geophysical Research*, vol.112, C08004, doi:10.1029/2006JC003543.

Arctic Monitoring and Assessment Programme (AMAP). 1998. AMAP Assessment Report: Arctic Pollution Issues. xii+859 pp. Oslo, Norway.

Arctic Monitoring and Assessment Programme (AMAP). 2012. Arctic Climate Issues 2011: Changes in Arctic Snow, Water, Ice and Permafrost. SWIPA 2011 Overview Report. xi + 97pp. Arctic Monitoring and Assessment Programme (AMAP), Oslo.

Bitz, C. 2009. Numerical modeling of sea ice in the climate system. Draft lecture notes. Atmospheric Sciences, University of Washington, US.

Bitz, C. 2013. Annual September Arctic Sea ice extent 1979-2012. Presentation, at congressional briefing. Atmospheric Sciences, Washington University, US.

Brandt Jensen, M. 2011. Arctic Sea Ice Variability and Trends 1979-2007. Master Thesis in Geophysics. Niels Bohr Institute, Faculty of Science, University of Copenhagen, Denmark.

Buizza, R. 2000. Chaos and weather prediction. *Meteorological Training Course Lecture Series*. European Centre for Medium-Range Weather (ECMWF).

Danish Meteorology Institute (DMI). 2012. BA Education Powerpoint, 4-5: Havis leksikon. Presentation. Copenhagen, Denmark.

Danish Meteorological Institute (DMI), Centre for Ocean and Ice. 2015. Arctic. (electronic) http://ocean.dmi.dk (2015-05-18)

Drusch, M. 2014. SMOS ICE: 6000 km of the Arctic Ocean covered. Blog. *European Space Agency's (ESA) Blog, Campaigns at work*. (electronic) http://blogs.esa.int (2015-05-24)

Dybkjær, G. 2015. Sea Ice Mass Balance Buoys and satellite data - in situ measurements for many purposes. Presentation, Remote Sensing Seminar at the Danish Meteorological Institute (DMI), Copenhagen, Denmark.

Eicken, H. 2003. From the Microscopic, to the Macroscopic, to the Regional Scale: Growth, Microstructure and Properties of Sea Ice. *Sea Ice*. p.22-81. Oxford, UK: Blackwell Science.

EUMETSAT. 2015. Metop. (electronic) http://www.eumetsat.int (2015-05-27)

European Centre for Medium-Range Weather (ECMWF). 2015. Climate reanalysis. (electronic) http://www.ecmwf.int (2015-05-17)

European Committee for Standardization (CEN). 2003. EN 1991-1-3:2003: Eurocode 1: Actions on structures - Part 1-3: General actions - Snow loads.

European Space Agency (ESA). 2011. New ice thickness map of the Arctic unveiled. (electronic)
http://www.esa.int (2015-05-19)

European Space Agency (ESA). 2015. ESA's Water Mission SMOS. (electronic)
http://www.esa.int (2015-05-17)

Haas, C. 2003. Dynamics versus Thermodynamics: The Sea Ice Thickness Distribution. *Sea Ice*. p.82-111. Oxford, UK: Blackwell Science.

International Organization for Standardization (ISO). 1998. Revised International Standard ISO 4355:2013(E) Bases for design on structures - Determination of snow loads on roofs. *International Organization for Standardization*, Geneva.

Jackson, K., J. Wilkinson, T. Maksym, D. Meldrum, J. Beckers, C. Haas, and D. Mackenzie. 2013. A Novel and Low-Cost Sea Ice Mass Balance Buoy. *Journal of Atmospheric and Oceanic Technology* 30: 2676-2688. American Meteorological Society. doi:10.1175/jtech-d-13-00058.1.

Japan Aerospace Exploration Agency (JAXA). 2015. GCOM-W. (electronic)
http://suzaku.eorc.jaxa.jp (2015-05-17)

Jordan, R., E. Andreas, and A. Makshtas. 1999. Heat budget of snow-covered sea ice at North Pole 4. *J. Geophys. Res.* 104: 7785. Wiley-Blackwell. doi:10.1029/1999jc900011.

Lebedev, V1. V. 1938. The dependency between growth of ice in Arctic rivers and seas and negative air temperatures. *Rost l'da v arkticheskikh rekakh i moriakh v zavisimosti ot otritsatel'nykh temperatur vozdukha*. (in Russian) Problemy arktiki 5-6: 9-25.

Laxon, S., N. Peacock, and D. Smith. 2003. High interannual variability of sea ice thickness in the Arctic region. *Nature* 425: 947-950. Nature Publishing Group. doi:10.1038/nature02050.

Lecomte, O., T. Fichefet, F. Massonnet, and M. Vancoppenolle. 2015. Benefits from representing snow properties and related processes in coupled ocean–sea ice models. *Ocean Modelling* 87: 81-85. Elsevier BV. doi:10.1016/j.ocemod.2014.11.005.

Lubin, D. and R. Massom. 2006. *Polar Remote Sensing - Atmosphere and Oceans*. vol.1. Springer Praxis Publishing Ltd, Chichester, U.K.

Markus, T., Cavalieri, D., Gasiewski, A., Klein, M., Maslanik, J., Powell, D., Stankov, B., Stroeve, J. and Sturm, M. 2006a. Microwave Signatures of Snow on Sea Ice: Observations. *IEEE Trans. Geosci. Remote Sensing*, 44: 3081-3090. doi: 10.1109/TGRS.2006.883134

Markus, T., Powell, D. and Wang, J. 2006b. Sensitivity of passive microwave snow depth retrievals to weather effects and snow evolution. *IEEE Trans. Geosci. Remote Sensing*. 44: 68-77. doi: 10.1109/TGRS.2005.860208

Massom, R., Eicken, H., Haas C., Jeffries M., Drinkwater M., Sturm, M., Worby A., Wu X., Lytle V., Ushio S., Morris K., Reid P., Warren S. and Allison I. 2001. Snow on Antarctic sea ice. *Reviews of Geophysics*, vol.39, no.3, 413-45. doi: 10.1029/2000RG000085

Mathew, N., Heygster, G., Melsheimer, C. and Kaleschke, L. 2008. Surface Emissivity of Arctic Sea Ice at AMSU Window Frequencies. *IEEE Trans. Geosci. Remote Sensing*. 46: 2298-2306. doi: 10.1109/TGRS.2008.916630

Mathworks. 2014. Matlab R2014b. Natick, MA, USA.

Maykut, G. 1986. *The surface heat and mass balance*. p.395-463. Seattle, Wash: Univ. of Washington. doi:10.1007/978-1-4899-5352-0_6

Microsoft. 2010. Office, Microsoft Excel Professional Plus 2010. Redmond, WA, USA.

National Oceanic and Atmospheric Administration (NOAA), National Centers for Environmental Information (NCEI). 2015. Numerical Weather Prediction. (electronic) https://www.ncdc.noaa.gov (2015-05-17)

National Oceanic and Atmospheric Administration (NOAA). Visualize CDC Derived NCEP Reanalysis Products - Surface Level Data. Earth System Research Laboratory, Physical Science Division, U.S. Commerce. (electronic) http://www.esrl.noaa.gov (2013-05-22)

National Snow and Ice Data Centre (NSIDC). 2015. Cryosphere. (electronic) http://nsidc.org (2015-05-18)

Norwegian Polar Institute. 2015. Norwegian young sea ICE cruise (N-ICE2015). (electronic) http://www.npolar.no (2015-05-24)

Perovich, D., T. Grenfell, J. Richter-Menge, B. Light, W. Tucker and H. Eicken. 2003. Thin and thinner: Sea ice mass balance measurements during SHEBA. *J. Geophys. Res.* 108. Wiley-Blackwell. doi:10.1029/2001jc001079.

Polarforskningssekretariatet. 2012. Polarforskningssekretariatet - LOMROG III. (electronic) http://polar.se/expedition/lomrog-iii (2015-05-12)

Pomeroy, J., D. Gray, K. Shook, B. Toth, R. Essery, A. Pietroniro, and N. Hedstrom. 1998. An evaluation of snow accumulation and ablation processes for land surface modelling. *Hydrol. Process.* 12: 2339-2367. Wiley-Blackwell. doi:10.1002/(sici)1099-1085(199812)12:15<2339::aid-hyp800>3.0.co;2-l.

Powell, D., T. Markus, D. Cavalieri, A. Gasiewski, M. Klein, J. Maslanik, J. Stroeve, and M. Sturm. 2006. Microwave Signatures of Snow on Sea Ice: Modeling. *IEEE Transactions on Geoscience and Remote Sensing* 44: 3091-3102. Institute of Electrical & Electronics Engineers (IEEE). doi:10.1109/tgrs.2006.882139.

Remote Sensing Systems (remss). 2015. AMSR2/AMSRE. (electronic) http://www.remss.com (2015-05-17)

Rudels, B., L. Anderson, and E. Jones. 1996. Formation and evolution of the surface mixed layer and halocline of the Arctic Ocean. *J. Geophys. Res.* 101: 8807. Wiley-Blackwell. doi:10.1029/96jc00143.

Sandven, S. and O.M. Johannessen. 2006. Sea Ice Monitoring by Remote Sensing. *Manual of Remote Sensing: Remote Sensing of the Marine Environment*. Editor J. Gower. 3rd ed. vol.6. p.241-283.

Scottish Association for Marine Science (SAMS). 2012. SAMS Ice Mass Balance Array Buoys (SIMBA) - Design and Deployment Description. Technology Development Group Version No. V5.0.

Solomon, S., D. Qin, M. Manning, Z. Chen, M. Marquis, K.B. Averyt, M. Tignor and H.L. Miller. 2007. *The Physical Science Basis*. Contribution of Working Group I to the Fourth Assessment Report of the Intergovernmental Panel on Climate Change (IPCC), Cambridge University Press, Cambridge, United Kingdom and New York, NY, USA.

Technical University of Denmark (DTU). 2013. North Atlantic - Arctic coupling in a changing climate: impacts on ocean circulation, carbon cycling and sea-ice (NAACOS). *Scientific interim report.* NAACOS Science Report.

Tedesco, M., and E. Kim. 2006. Retrieval of dry-snow parameters from microwave radiometric data using a dense-medium model and genetic algorithms. *IEEE Trans. Geosci. Remote Sensing* 44: 2143-2151. Institute of Electrical & Electronics Engineers (IEEE). doi:10.1109/tgrs.2006.872087.

The International Bathymetric Chart of the Arctic Ocean (IBCAO). 2008. IBCAO. (electronic)
http://www.ibcao.org (2015-05-18)

Tonboe, R. 2003. Remote sensing of the sea ice around Greenland using multiple microwave sensors. PhD Thesis in Geophysics. University of Copenhagen, Denmark.

Tonboe, R. 2010. The simulated sea ice thermal microwave emission at window and sounding frequencies. *Tellus A*. Co-Action Publishing. doi:10.3402/tellusa.v62i3.15683.

Tonboe, R., G. Dybkjær, and J. Høyer. 2011. Simulations of the snow covered sea ice surface temperature and microwave effective temperature. *Tellus A* 63: 1028-1037. Co-Action Publishing. doi:10.1111/j.1600-0870.2011.00530.x.

Toudal Pedersen, L. 2004. A sea ice model for the marginal ice zone with an application to the Greenland Sea. *J. Geophys. Res.* 109. Wiley-Blackwell. doi:10.1029/2003jc001827.

Toudal Pedersen, L., R.T. Tonboe, M. Brandt Jensen, G. Dybkjær, M. Nissen, J. Rasmussen, S.M. Olsen, H. Skourup, R. Saldo and R. Forsberg. 2011. KANUMAS MET/ICE/OCEAN Overview Report 2011 - East Greenland. Bureau of Mineral and Petrol, Greenland.

Ukita, J. 2015. Mid-latitudes atmospheric impacts from the Arctic sea-ice reduction. GRENE Arctic Climate Change Research Project. Niigata University, Japan. Presentation. Danish Meteorological Institute (DMI), Copenhagen, Denmark.

University College London (UCL). 2011. CryoSat-2 satellite redraws Arctic sea-ice map. (electronic)
https://www.ucl.ac.uk (2015-05-29)

Wadhams, P. 2000. *Ice in the ocean*. Australia: Gordon and Breach.

Wan, Z., Zhang, Y., Zhang, Q. and Li, Z. 2002. Validation of the land-surface temperature products retrieved from Terra Moderate Resolution Imaging Spectroradiometer data. *Remote Sensing of Environment*, 83(1-2): 163-180. doi:10.1016/S0034-4257(02)00093-7

Warren, S., I. Rigor, N. Untersteiner, V. Radionov, N. Bryazgin, Y. Aleksandrov, and R. Colony. 1999. Snow Depth on Arctic Sea Ice. *Journal of Climate* 12: 1814-1829. American Meteorological Society. doi:10.1175/1520-0442(1999)012<1814:sdoasi>2.0.co;2.

Willmes, S., M. Nicolaus, and C. Haas. 2014. The microwave emissivity variability of snow covered first-year sea ice from late winter to early summer: a model study. *The Cryosphere* 8: 891-904. Copernicus GmbH. doi:10.5194/tc-8-891-2014.

World Meteorological Organization (WMO). 2015. Observing Systems Capability Analysis and Review Tool (OSCAR) – Instrument: AMSR-2. (electronic)
http://www.wmo-sat.info (2015-05-17)

Zubov, N. N. 1943. *Arctic Ice*. Translation, National Service (AD426972), USA. 491 pp.

Appendix A

Statistics for IMB buoys 3-6 including measuring period, position, temperature measurements, snow and ice thickness as well as modelled NWP weather data.

Buoy 3

Period	**2012-09-01 to 2013-05-31**				
2n period*(no statistics)	**2013-09-01 to 2013-10-25**				
	max	**mean**	**min**	**variation**	**stdev**
Latitude	87.53	85.72	84.79	2.74	0.76
Longitude	-34.14	-53.29	-67.20	33.07	7.47
Air-snow interface [K]	273.03	250.65	226.40	46.63	13.04
Snow mean [K]	272.96	253.58	234.96	38.00	10.53
Snow-ice interface [K]	272.96	256.51	243.15	29.81	8.38
0.1m into ice [K]	273.03	257.82	245.78	27.25	7.97
0.3m into ice [K]	272.78	259.01	248.21	24.56	7.53
0.5m into ice [K]	272.65	259.91	249.90	22.75	7.22
Ice-water interface [K]	271.40	271.31	271.15	0.25	0.06
Snow thickness [m]	0.49	0.36	0.06	0.43	0.16
Delta snow thickness [m]	0.03	0.00	-0.01	0.04	0.00
Ice thickness [m]	3.99	3.71	3.43	0.56	0.22
Delta ice thickness [m]	0.01	0.00	-0.01	0.02	0.00
Air temp, (median value for sensor 1-5) [K]	273.46	250.31	226.71	46.75	12.63
Water temp, (median value for sensor 230-240) [K]	271.40	271.35	271.28	0.13	0.03
Mean sea level pressure [hPa]	1056	1020	986	70	12
2 m air temperature [K]	273.50	253.78	236.45	37.05	9.82
Wind speed [ms^{-1}]	20.51	5.53	0.45	20.06	3.38
Short wave radiation in [Jm^{-2}]	17551144	1683247	0	17551144	3451771
Long wave radiation in [Jm^{-2}]	15860931	6925118	2443526	13417406	3249321
Dew point temperature [K]	0.06	-21.80	-40.11	40.17	10.47
6h accumulated precipitation [mm]	3.71	0.15	0.00	3.71	0.39
Total cover liquid water [kgm^{-2}]	0.29	0.02	0.00	0.29	0.04
Total cover ice water [kgm^{-2}]	0.24	0.02	0.00	0.24	0.03
Total cover water vapour [kgm^{-2}]	17.72	3.68	0.68	17.04	3.07

A1. Table containing statistics for buoy 3.

Buoy 4

Period	2012-09-01 to 2013-04-17				
	max	mean	min	variation	stdev
Latitude	87.79	85.78	81.96	5.84	1.56
Longitude	-10.97	-25.80	-44.27	33.30	9.64
Air-snow interface [K]	273.09	258.22	231.40	41.69	9.41
Snow mean [K]	273.06	260.76	240.37	32.69	7.34
Snow-ice interface [K]	273.03	263.30	248.21	24.81	5.63
0.1m into ice [K]	272.90	264.41	250.71	22.19	5.38
0.3m into ice [K]	272.78	265.26	252.96	19.81	5.13
0.5m into ice [K]	272.59	266.31	255.34	17.25	4.60
Ice-water interface [K]	271.40	271.16	269.21	2.19	0.58
Snow thickness [m]	0.36	0.22	0.05	0.31	0.11
Delta snow thickness [m]	0.02	0.00	-0.02	0.04	0.00
Ice thickness [m]	2.04	1.68	1.49	0.55	0.17
Delta ice thickness [m]	0.03	0.00	-0.01	0.04	0.00
Air temp, (median value for sensor 1-5) [K]	273.46	257.08	231.21	42.25	9.66
Water temp, (median value for sensor 230-240) [K]	271.40	271.27	270.34	1.06	0.21
Mean sea level pressure [hPa]	1062	1015	984	78	11
2 m air temperature [K]	273.81	258.66	239.12	34.69	7.87
Wind speed [ms^{-1}]	16.35	6.35	0.24	16.11	3.62
Short wave radiation in [Jm^{-2}]	9116615	572393	0	9116615	1278655
Long wave radiation in [Jm^{-2}]	18136066	9763464	3796414	14339652	3584121
Dew point temperature [K]	273.49	256.64	236.10	37.39	8.65
6h accumulated precipitation [mm]	278.75	273.40	273.15	5.60	0.49
Total cover liquid water [kgm^{-2}]	273.49	273.18	273.15	0.34	0.05
Total cover ice water [kgm^{-2}]	273.42	273.18	273.15	0.27	0.04
Total cover water vapour [kgm^{-2}]	290.58	278.00	273.94	16.64	3.44

A2. Statistics for buoy 4.

Buoy 5

Period	2012-09-01 to 2012-12-29				
	max	mean	min	variation	stdev
Latitude	86.30	84.18	80.02	6.29	1.84
Longitude	-0.01	-6.88	-13.71	13.71	4.18
Air-snow interface [K]	273.46	260.33	246.03	27.44	7.89
Snow mean [K]	273.34	262.73	250.37	22.97	6.50
Snow-ice interface [K]	273.21	265.12	254.09	19.12	5.59
0.1m into ice [K]	273.21	265.90	255.84	17.37	5.26
0.3m into ice [K]	273.34	267.01	258.21	15.13	4.76
0.5m into ice [K]	273.03	268.05	260.65	12.38	4.07
Ice-water interface [K]	271.65	271.36	271.09	0.56	0.10
Snow thickness [m]	0.46	0.17	0.02	0.44	0.08
Delta snow thickness [m]	0.07	0.00	-0.11	0.18	0.01
Ice thickness [m]	1.63	1.40	1.30	0.32	0.10
Delta ice thickness [m]	0.03	0.00	-0.02	0.05	0.00
Air temp, (median value for sensor 1-5) [K]	273.71	258.31	240.15	33.56	8.99
Water temp, (median value for sensor 230-240) [K]	271.53	271.42	271.34	0.19	0.06
Mean sea level pressure [hPa]	1036	1014	980	55.88	9.78
2 m air temperature [K]	274.09	258.66	245.51	28.58	7.55
Wind speed [ms^{-1}]	20.21	6.14	0.05	20.16	3.55
Short wave radiation in [Jm^{-2}]	3915299	265559	0	3915299	657229
Long wave radiation in [Jm^{-2}]	16673874	9396657	3837490	12836384	2925570
Dew point temperature [K]	273.74	256.58	242.55	31.19	8.37
6h accumulated precipitation [mm]	4.49	0.21	0.00	4.49	0.40
Total cover liquid water [kgm^{-2}]	0.27	0.02	0.00	0.27	0.04
Total cover ice water [kgm^{-2}]	0.39	0.02	0.00	0.39	0.04
Total cover water vapour [kgm^{-2}]	18.57	4.87	0.97	17.60	3.25

A3. Statistics for buoy 5.

Buoy 6

Period	2012-09-01 to 2013-01-27				
	max	mean	min	variation	stdev
Latitude	87.06	85.35	80.53	6.54	1.39
Longitude	-6.75	-17.97	-31.03	24.28	7.30
Air-snow interface [K]	273.28	258.41	244.03	29.25	8.03
Snow mean [K]	273.18	260.82	248.34	24.84	6.95
Snow-ice interface [K]	273.15	263.24	251.59	21.56	6.33
0.1m into ice [K]	273.15	263.72	252.65	20.50	6.14
0.3m into ice [K]	273.09	264.69	254.59	18.50	5.72
0.5m into ice [K]	272.84	265.49	256.15	16.69	5.32
Ice-water interface [K]	271.53	271.37	271.21	0.31	0.06
Snow thickness [m]	0.53	0.24	0.12	0.41	0.05
Delta snow thickness [m]	0.03	0.00	-0.07	0.10	0.01
Ice thickness [m]	3.04	2.81	2.75	0.29	0.07
Delta ice thickness [m]	0.03	0.00	-0.01	0.04	0.00
Air temp, (median value for sensor 1-5) [K]	273.59	256.23	236.34	37.25	9.53
Water temp, (median value for sensor 230-240) [K]	273.80	273.69	273.40	0.40	0.05
Mean sea level pressure [hPa]	1034	1014	989	44.44	10
2 m air temperature [K]	273.89	257.68	244.66	29.23	8.00
Wind speed [ms^{-1}]	20.75	6.23	0.30	20.45	3.44
Short wave radiation in [Jm^{-2}]	4182734	250662	0	4182734	664405
Long wave radiation in [Jm^{-2}]	16816250	7915175	2864002	13952248	3345456
Dew point temperature [K]	273.57	255.60	241.83	31.74	8.77
6h accumulated precipitation [mm]	3.80	0.21	0.00	3.80	0.44
Total cover liquid water [kgm^{-2}]	0.33	0.02	0.00	0.33	0.05
Total cover ice water [kgm^{-2}]	0.39	0.02	0.00	0.39	0.04
Total cover water vapour [kgm^{-2}]	17.08	4.61	1.01	16.07	3.27

A4. Statistics for buoy 6.

Appendix B

Temperature profiles measured by the IMB buoys down through the snow and ice layers, i.e. the air-snow interface, snow mean, snow-ice interface, 0.1, 0.3 and 0.5 m into the ice as well as the ice-water interface. Note the different ranges on the temperature y-axis.

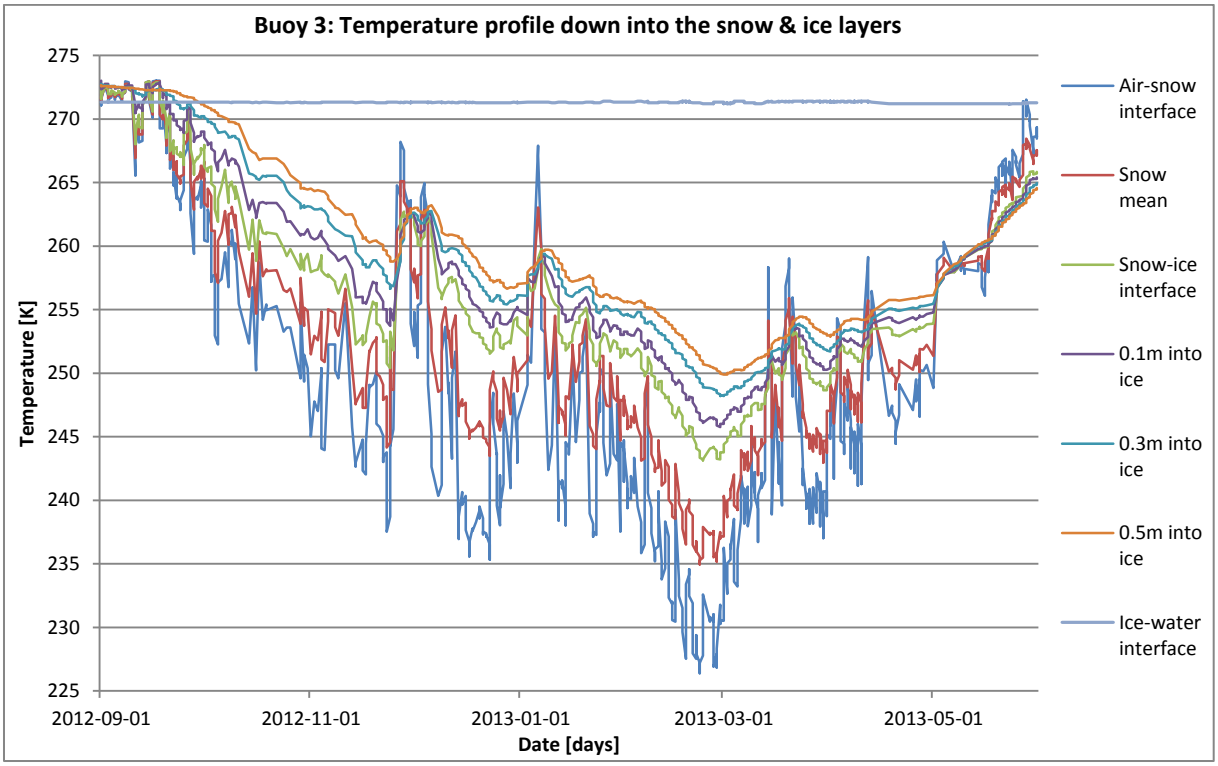

B1. The measured temperature profile down into the snow and ice layers for buoy 3, 2012-09-01 until 2013-05-31; air-snow interface temperature (dark blue), snow mean (red), snow-ice interface (green), 0.1 m into the ice (purple), 0.3 m into the ice (cerulean blue), 0.5 m into the ice (orange) and the temperature at the ice-water interface (light blue).

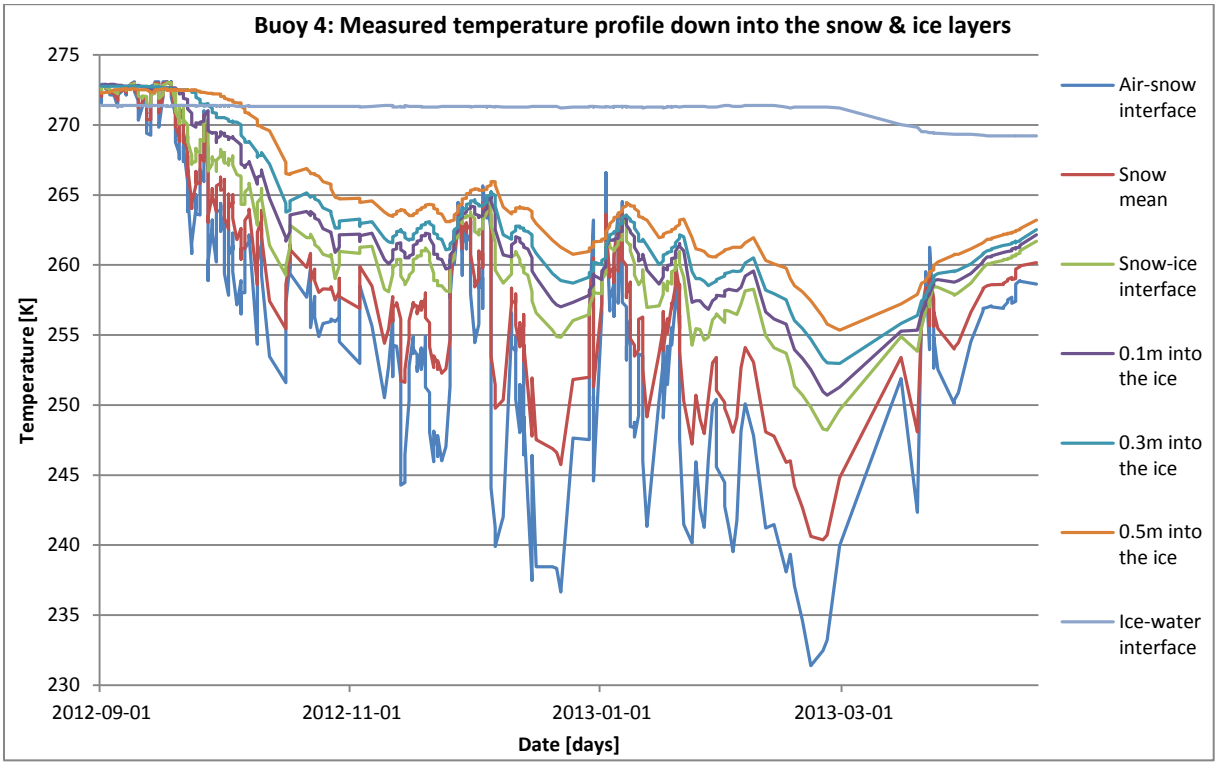

B2. The measured temperature profile down into the snow and ice layers for buoy 3, 2012-09-01 until 2013-04-17; air-snow interface temperature (dark blue), snow mean (red), snow-ice interface (green), 0.1 m into the ice (purple), 0.3 m into the ice (cerulean blue), 0.5 m into the ice (orange) and the temperature at the ice-water interface (light blue).

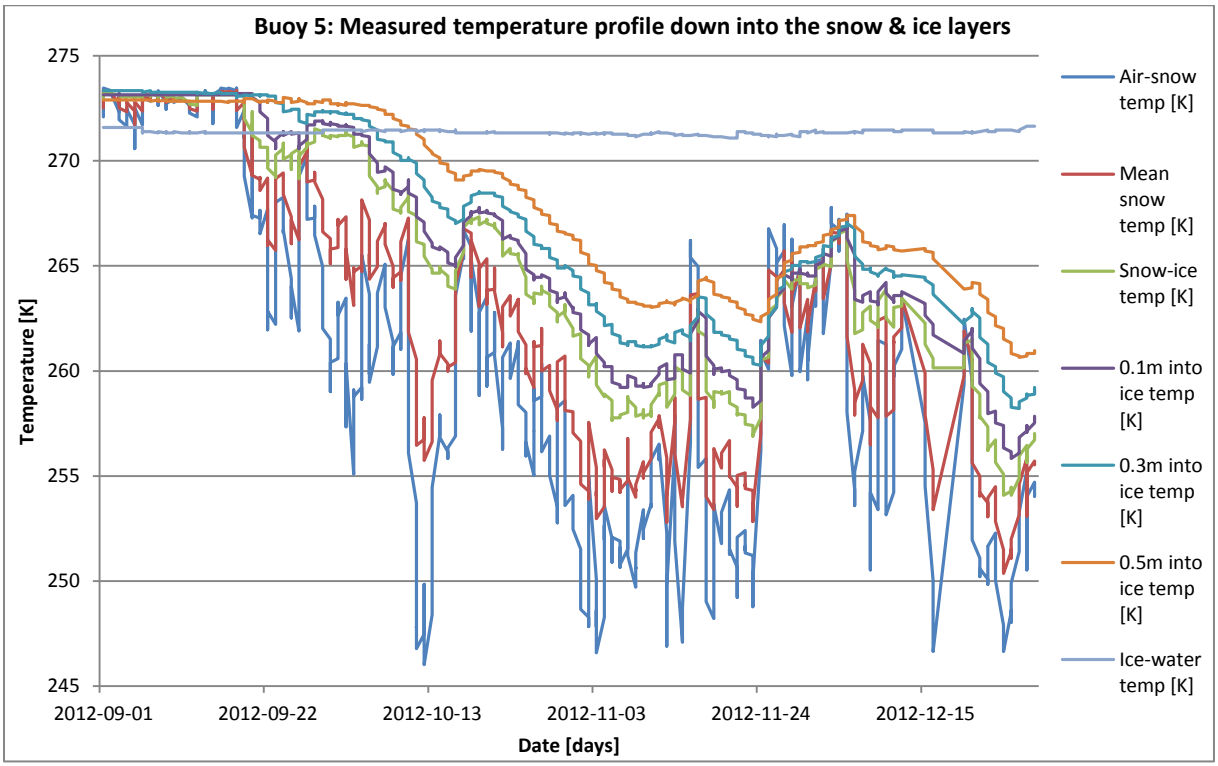

B3. The measured temperature profile down into the snow and ice layers for buoy 3, 2012-09-01 until 2013-12-29; air-snow interface temperature (dark blue), snow mean (red), snow-ice interface (green), 0.1 m into the ice (purple), 0.3 m into the ice (cerulean blue), 0.5 m into the ice (orange) and the temperature at the ice-water interface (light blue).

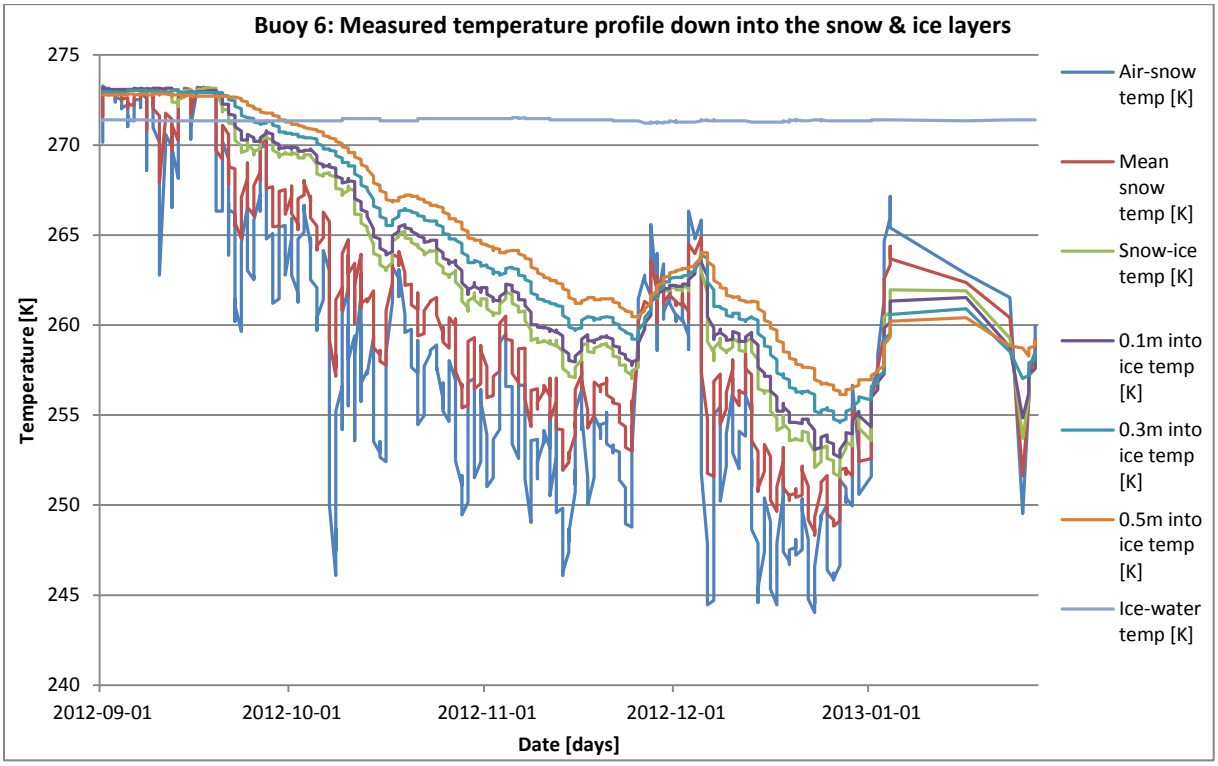

B4. The measured temperature profile down into the snow and ice layers for buoy 3, 2012-09-01 until 2013-01-27; air-snow interface temperature (dark blue), snow mean (red), snow-ice interface (green), 0.1 m into the ice (purple), 0.3 m into the ice (cerulean blue), 0.5 m into the ice (orange) and the temperature at the ice-water interface (light blue).

Appendix C

Comparisons of AMSR2 89 GHz, H and V, as well as TIR against the surface and air temperatures.

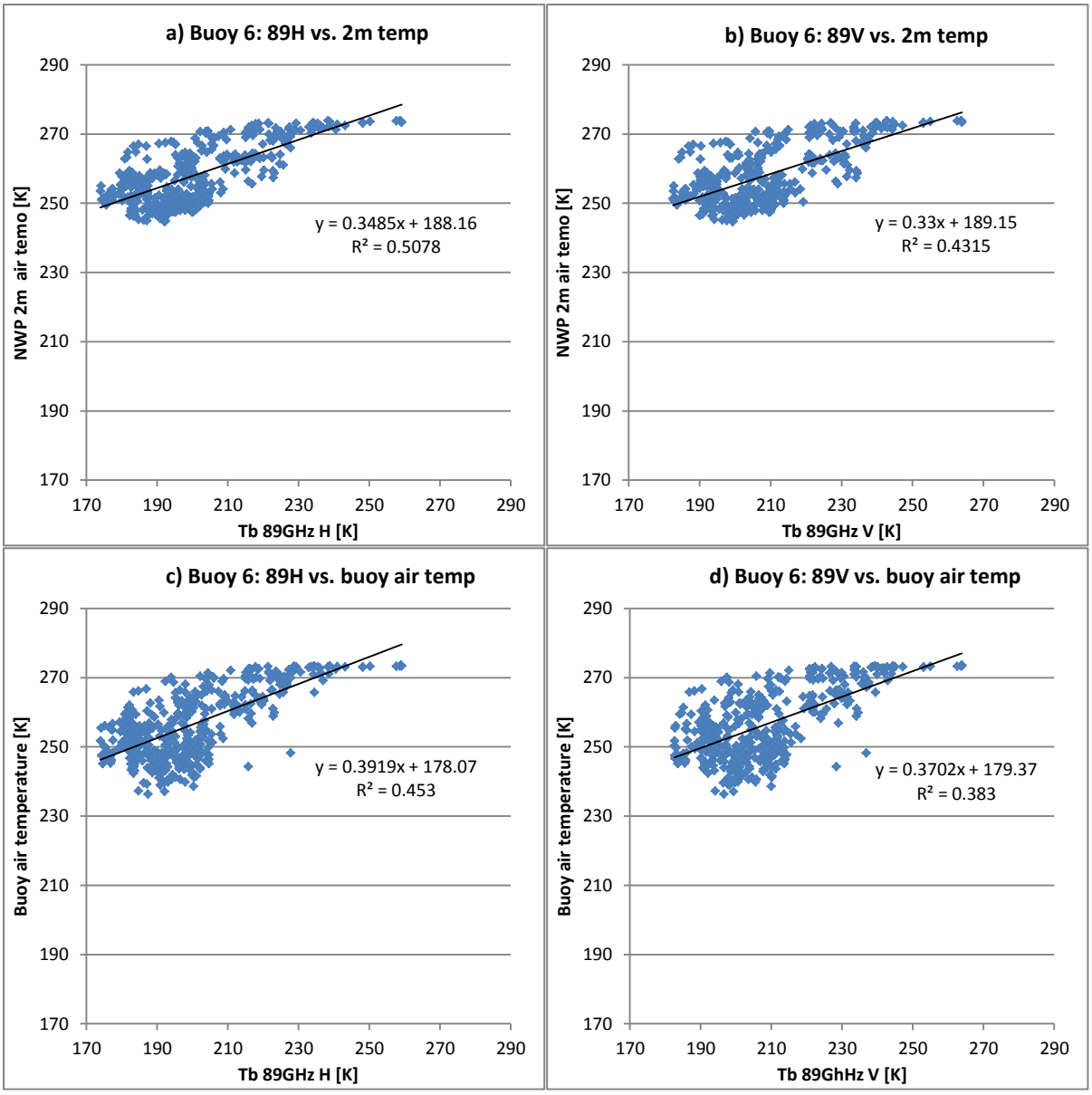

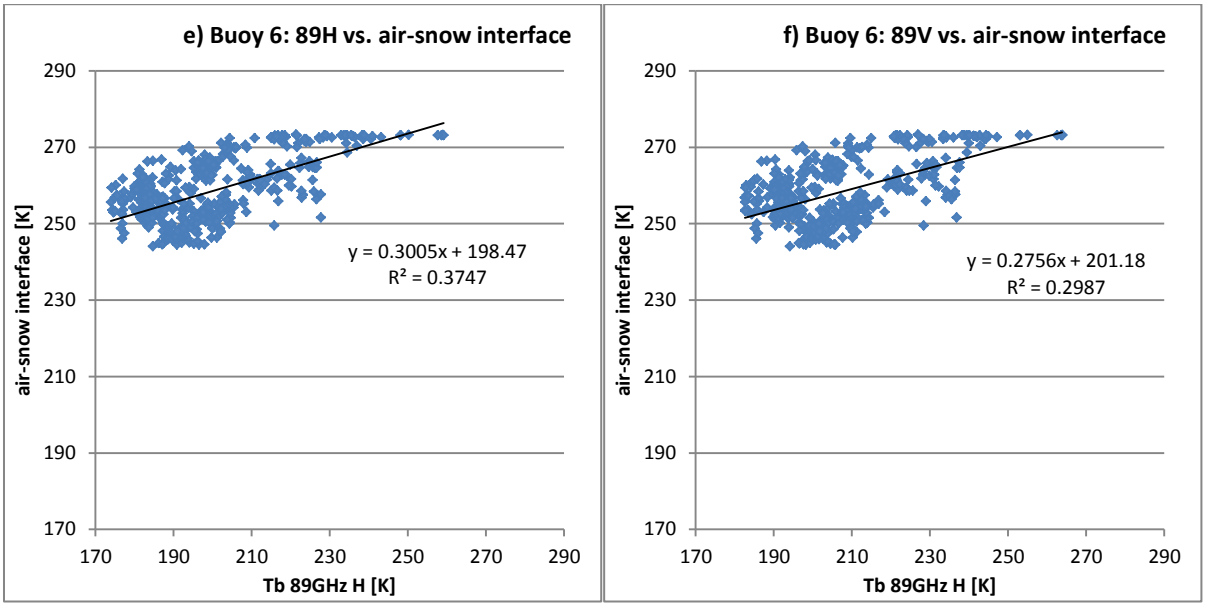

C1. Comparison between horizontal H (left) and vertical V (right) polarization of AMSR2 89 GHz as it is plotted against; a-b) NWP 2m air temperature, c-d) buoy air temperature and e-f) air-snow interface temperature for buoy 6 during the period 2012-09-01 until 2013-01-27. A linear fit is added to every plot and the corresponding linear equation and R^2-value can be seen in the figures.

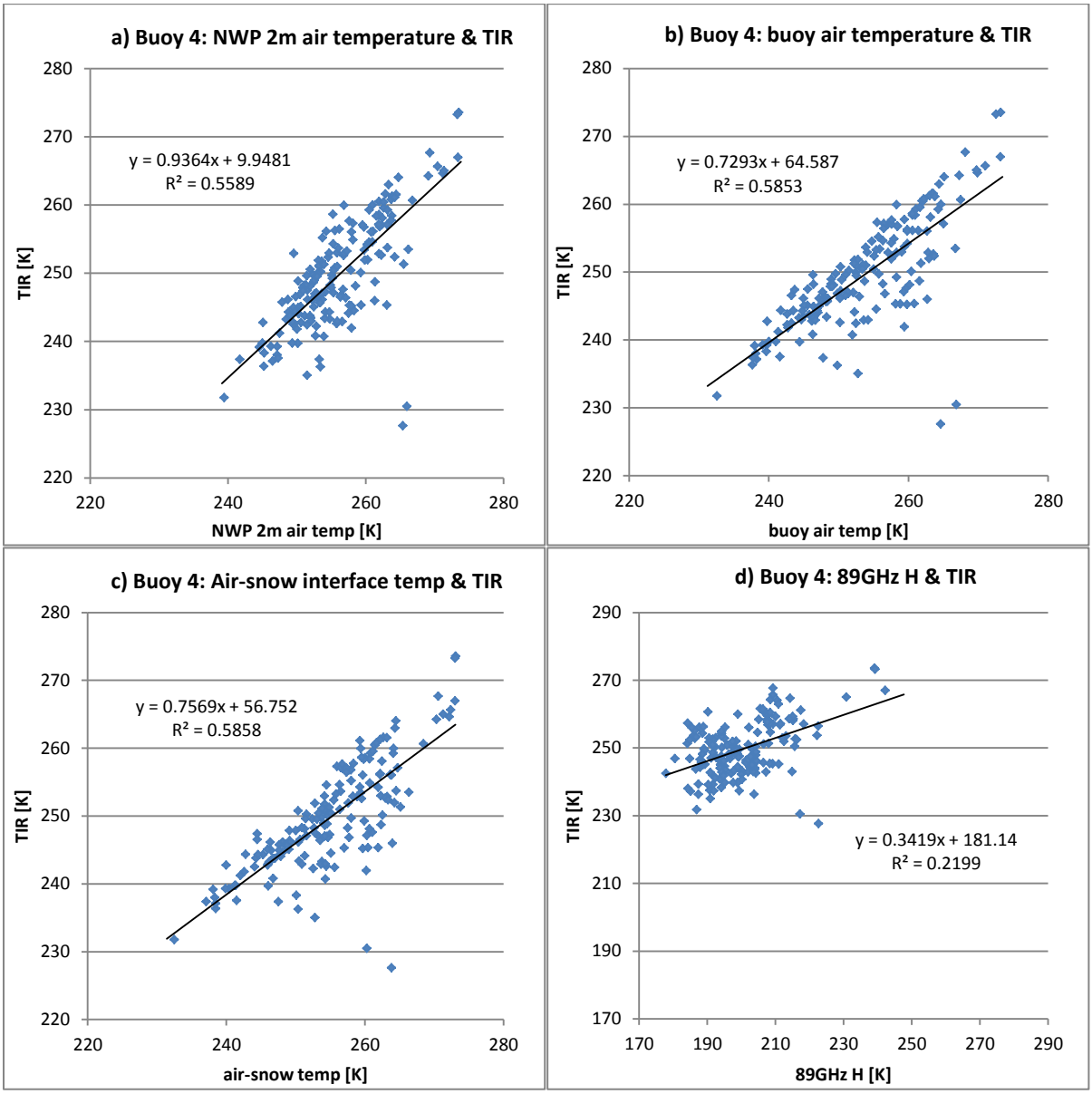

C2. Scatterplots of TIR plotted against a) NWP 2m air temperature, b) buoy air temperature (median value of sensor 1-5), c) buoy air-snow interface temperature and d) AMSR2 89 GHz H brightness temperature for buoy 4, during the period 2012-09-01 to 2013-04-17. In every figure a linear fit has been inserted and the linear equation and R^2-values are displayed.

Appendix D

Graphs describing different snow parameters, such as the temperature gradient, spectral gradient ratio and thickness compared to NWP data.

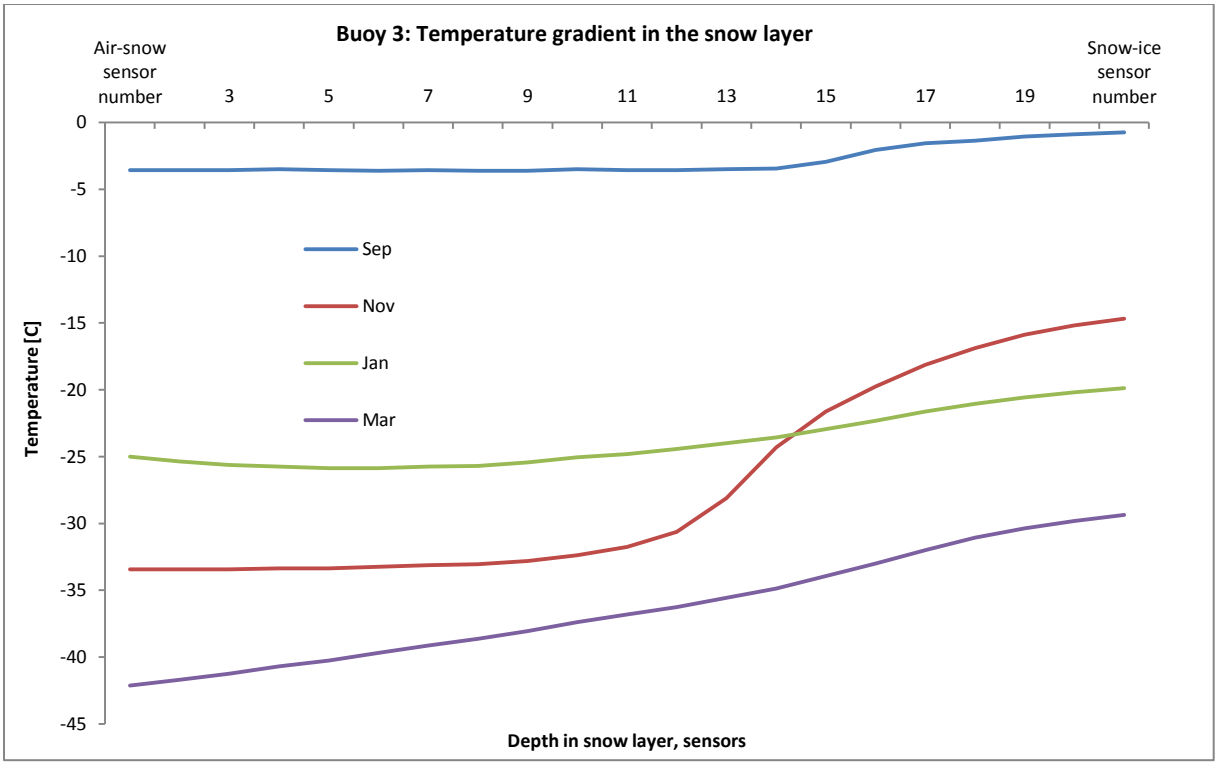

D1. The observed temperature gradient through the snow layer from buoy 3. The temperature gradient (in degree Celsius) for the 1st each month is displayed in the figure; blue line for September, red for November, green for January and purple for March in the winter period 201-2013.

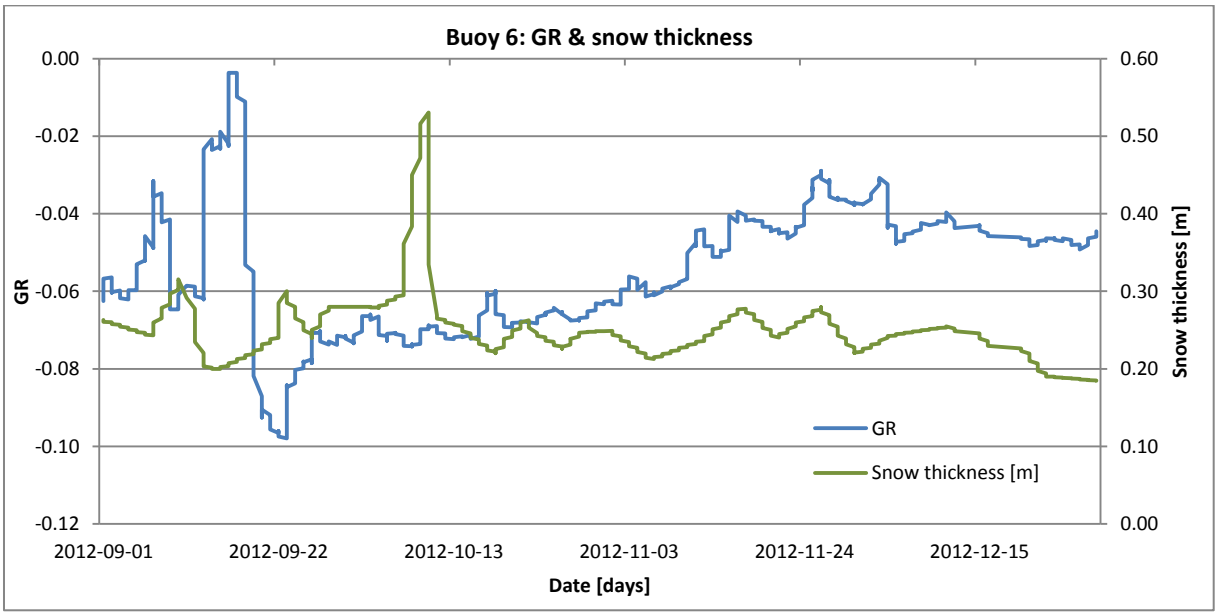

D2. Spectral gradient ratio (GR) and snow thickness for buoy 6 during the period 2012-09-01 to 2013-01-29.

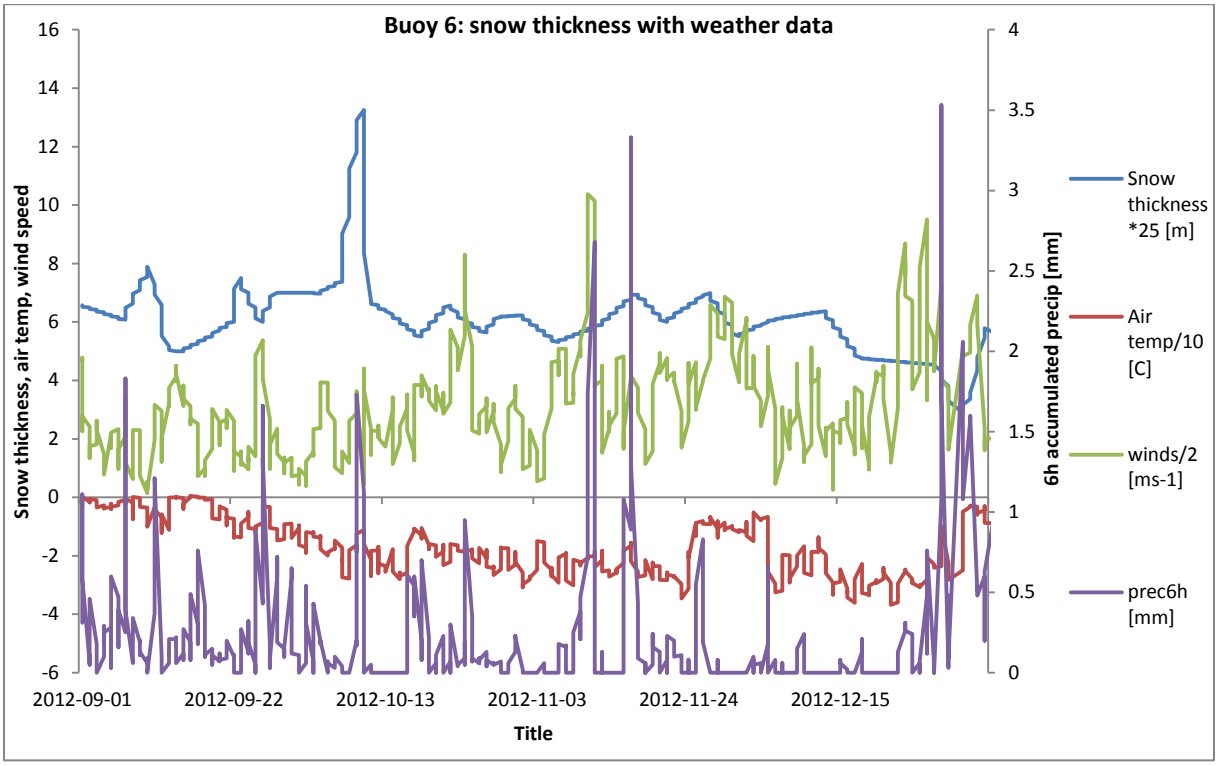

D3. A time series describing the variations of the predicted and observed conditions at the location for buoy 6, 2012-09-01 until 2012-01-27; the measured snow thickness in meters times ten (blue line), buoy air temperature in degree Celsius divided by ten (red line), NWP wind speed in meters per second divided by ten (green line) and on the secondary y-axis NWP 6h accumulated precipitation in millimeters (purple line).

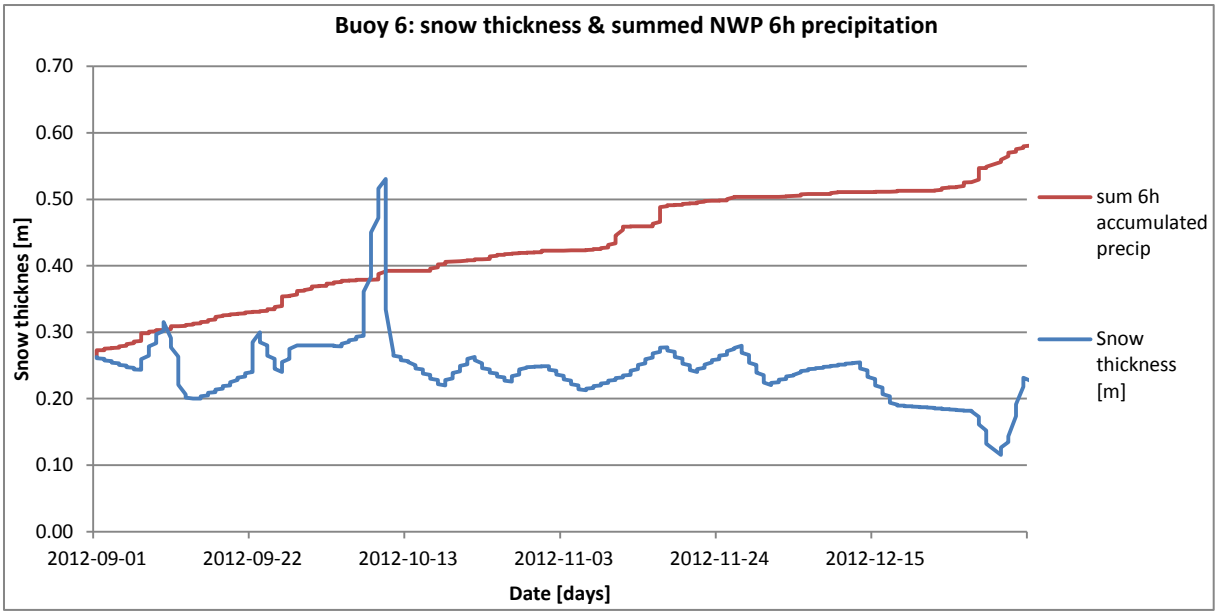

D4. The snow thickness measured by buoy 6 (blue line) and the sum of the NWP 6h accumulated precipitation (red line), both in meters. The 6h accumulated precipitation has been multiplied with the ratio of the density of water (1000 kgm^{-3}) and the assumed average density of the snow layer of 300 kgm^{-3}.

Appendix E

Sea ice thickness calculated according to the empirical models by Lebedev (1938), Zubov (1943) and Maykut (1986), Equations 8-11.

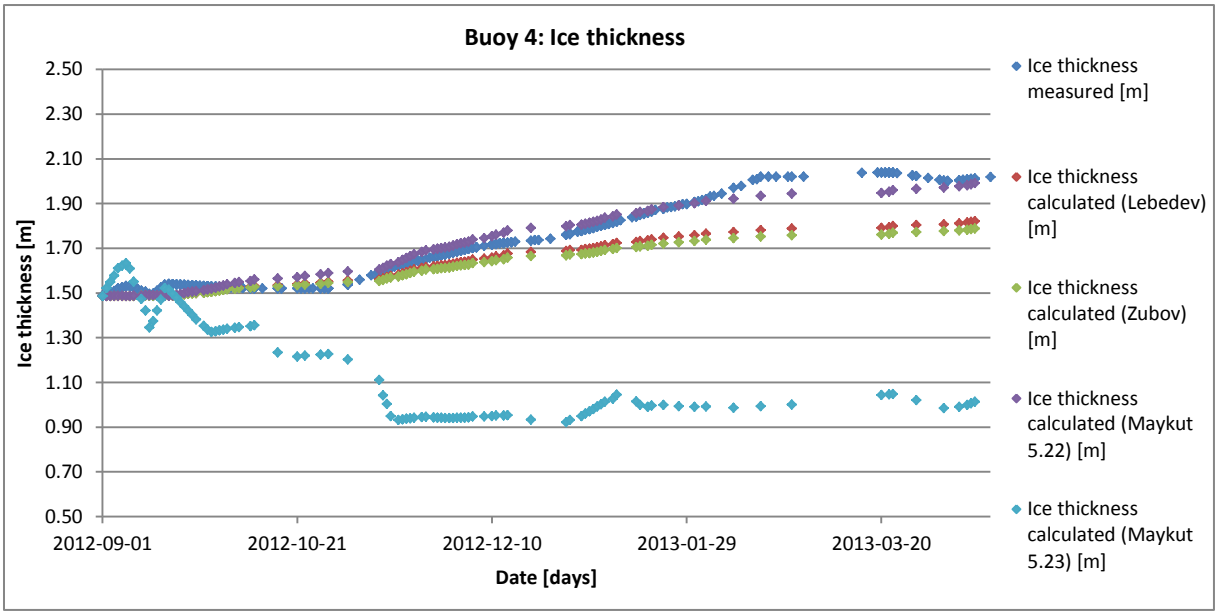

E1. Measured and calculated ice thickness for buoy 4 in meters for the period 2012-09-01 to 2013-04-17. The measured ice thickness is indicated by dark blue dots, ice thickness calculated with the equation of Lebedev (1938) is indicated with red dots, Zubov (1943) with green dots, Maykut (1986) equation 5.22 with purple dots and Maykut (1986) equation 5.23 where the snow thickness is considered with light blue dots.

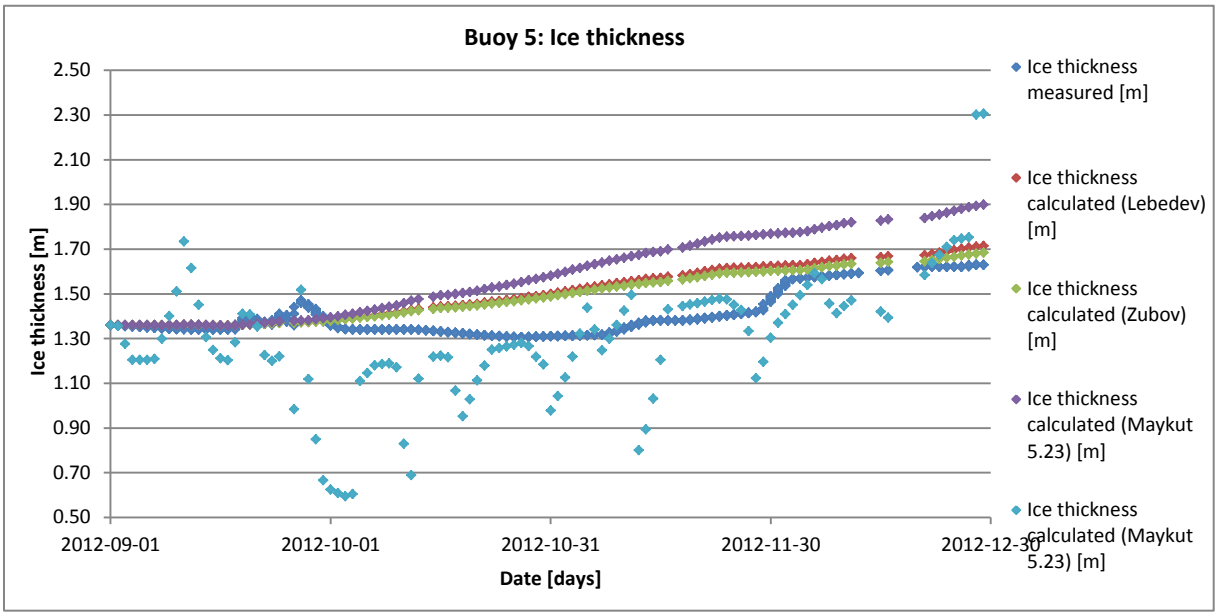

E2. Measured and calculated ice thickness for buoy 5 in meters for the period 2012-09-01 to 2013-12-29. The measured ice thickness is indicated by dark blue dots, ice thickness calculated with the equation of Lebedev (1938) is indicated with red dots, Zubov (1943) with green dots, Maykut (1986) equation 5.22 with purple dots and Maykut (1986) equation 5.23 where the snow thickness is considered with light blue dots.

Appendix F

Parts of the correlation matrices used as a basis for choosing suitable variables in the regression analysis.

	Air temp [K]	Air-snow interface	Snow median	Snow-ice interface	0.1m into ice	0.3m into ice	0.5m into ice	Ice-water interface
Air temp [K]	1.00							
Air-snow interface	1.00	1.00						
Snow median	0.99	0.99	1.00					
Snow-ice interface	0.91	0.92	0.96	1.00				
0.1m into ice	0.87	0.88	0.93	0.99	1.00			
0.3m into ice	0.80	0.81	0.88	0.96	0.99	1.00		
0.5m into ice	0.75	0.77	0.84	0.93	0.97	0.99	1.00	
Ice-water interface	-0.23	-0.25	-0.25	-0.26	-0.26	-0.25	-0.24	1.00
Water temp [K]	-0.23	-0.23	-0.23	-0.22	-0.21	-0.20	-0.18	0.06
nwp2mt [K]	0.96	0.97	0.97	0.92	0.89	0.83	0.79	-0.27
TIR_stmean [K]	0.92	0.93	0.93	0.88	0.84	0.77	0.72	-0.26
AMSR2 6.9H	0.72	0.73	0.74	0.72	0.67	0.60	0.54	-0.28
AMSR2 6.9V	0.88	0.89	0.94	0.98	0.98	0.96	0.93	-0.28
AMSR2 7.3H	0.73	0.73	0.74	0.72	0.67	0.60	0.54	-0.28
AMSR2 7.3V	0.89	0.90	0.94	0.98	0.98	0.96	0.93	-0.28
AMSR2 10H	0.73	0.74	0.74	0.70	0.66	0.57	0.51	-0.29
AMSR2 10V	0.90	0.91	0.95	0.97	0.96	0.92	0.89	-0.30
AMSR2 18H	0.78	0.79	0.79	0.76	0.71	0.63	0.57	-0.29
AMSR2 18V	0.91	0.92	0.95	0.95	0.93	0.87	0.82	-0.30
AMSR2 23H	0.84	0.85	0.86	0.83	0.80	0.73	0.67	-0.31
AMSR2 23V	0.92	0.93	0.95	0.95	0.92	0.86	0.81	-0.28
AMSR2 36H	0.84	0.84	0.85	0.83	0.79	0.71	0.65	-0.23
AMSR2 36V	0.92	0.93	0.95	0.94	0.91	0.85	0.79	-0.27
AMSR2 89H	0.87	0.87	0.88	0.84	0.81	0.75	0.70	-0.10
AMSR2 89V	0.88	0.88	0.89	0.87	0.84	0.79	0.74	-0.10
tbh2535	0.36	0.38	0.44	0.54	0.57	0.60	0.60	-0.15
tbv2535	0.59	0.60	0.64	0.69	0.71	0.72	0.72	-0.21
tbh4050	0.59	0.61	0.66	0.73	0.75	0.75	0.74	-0.25
tbv4050	0.55	0.57	0.64	0.73	0.76	0.78	0.78	-0.23

F1. Correlation matrix for buoy 3 including TIR measurements, November 2012 until May 2013, where the air and water temperature are median value for sensor 1-5 and sensor 230-240 respectively.

	Air temp [K]	Air-snow interface	Snow median	Snow-ice interface	0.1m into ice	0.3m into ice	0.5m into ice	Ice-water interface
Air temp [K]	1.00							
Air-snow interface	0.99	1.00						
Snow median	0.95	0.98	1.00					
Snow-ice interface	0.78	0.83	0.93	1.00				
0.1m into ice	0.71	0.77	0.89	0.99	1.00			
0.3m into ice	0.63	0.70	0.83	0.96	0.99	1.00		
0.5m into ice	0.59	0.66	0.79	0.93	0.98	1.00	1.00	
Ice-water interface	0.13	0.12	0.10	0.05	0.03	0.01	0.00	1.00
Water temp [K]	0.07	0.09	0.10	0.11	0.12	0.13	0.13	0.05
nwp2mt [K]	0.94	0.94	0.91	0.77	0.69	0.61	0.56	0.11
AMSR2 6.9H	0.34	0.34	0.34	0.31	0.26	0.21	0.18	0.07
AMSR2 6.9V	0.76	0.81	0.91	0.97	0.97	0.95	0.93	0.07
AMSR2 7.3H	0.33	0.33	0.33	0.29	0.24	0.18	0.15	0.07
AMSR2 7.3V	0.77	0.82	0.91	0.97	0.96	0.94	0.92	0.08
AMSR2 10H	0.12	0.07	-0.01	-0.13	-0.22	-0.30	-0.34	0.07
AMSR2 10V	0.82	0.85	0.91	0.92	0.89	0.84	0.81	0.12
AMSR2 18H	0.05	-0.01	-0.12	-0.29	-0.39	-0.47	-0.51	0.11
AMSR2 18V	0.74	0.72	0.69	0.57	0.47	0.37	0.31	0.19
AMSR2 23H	0.20	0.13	0.03	-0.15	-0.26	-0.36	-0.41	0.13
AMSR2 23V	0.72	0.68	0.63	0.47	0.37	0.25	0.19	0.21
AMSR2 36H	0.25	0.18	0.08	-0.10	-0.21	-0.31	-0.37	0.23
AMSR2 36V	0.55	0.49	0.40	0.20	0.08	-0.04	-0.11	0.21
AMSR2 89H	0.63	0.59	0.50	0.30	0.19	0.08	0.02	0.27
AMSR2 89V	0.60	055	0.44	0.23	0.11	0.00	-0.06	0.23
tbh4050	0.51	0.55	0.64	0.72	0.73	0.73	0.71	-0.10
tbv4050	0.52	0.58	0.69	0.80	0.83	0.84	0.84	0.04

F2. Correlation matrix for buoy 5 excluding TIR measurements, October 2012 until April 2013, where the air and water temperature are median value for sensor 1-5 and sensor 230-240 respectively.

Department of Physical Geography and Ecosystem Science, Lund University

The student thesis reports are available at the Geo-Library, Department of Physical Geography and Ecosystem Science, University of Lund, Sölvegatan 12, S-223 62 Lund, Sweden. Report series started 1985. The complete list and electronic versions are also electronic available at the LUP student papers (https://lup.lub.lu.se/student-papers/search/) and through the Geo-library (www.geobib.lu.se)

335 Fei Lu (2015) Compute a Crowdedness Index on Historical GIS Data- A Case Study of Hög Parish, Sweden, 1812-1920
336 Lina Allesson (2015) Impact of photo-chemical processing of dissolved organic carbon on the bacterial respiratory quotient in aquatic ecosystems
337 Andreas Kiik (2015) Cartographic design of thematic polygons: a comparison using eye-movement metrics analysis
338 Iain Lednor (2015) Testing the robustness of the Plant Phenology Index to changes in temperature
339 Louise Bradshaw (2015) Submerged Landscapes - Locating Mesolithic settlements in Blekinge, Sweden
340 Elisabeth Maria Farrington (2015) The water crisis in Gaborone: Investigating the underlying factors resulting in the 'failure' of the Gaborone Dam, Botswana
341 Annie Forssblad (2015) Utvärdering av miljöersättning för odlingslandskapets värdefulla träd
342 Iris Behrens, Linn Gardell (2015) Water quality in Apac-, Mbale- & Lira district, Uganda - A field study evaluating problems and suitable solutions
343 Linnéa Larsson (2015) Analys av framtida översvämningsrisker i Malmö - En fallstudie av Castellums fastigheter
344 Ida Pettersson (2015) Comparing Ips Typographus and Dendroctonus ponderosas response to climate change with the use of phenology models
345 Frida Ulfves (2015) Classifying and Localizing Areas of Forest at Risk of Storm Damage in Kronoberg County
346 Alexander Nordström (2015) Förslag på dammar och skyddsområde med hjälp av GIS: En studie om löv- och klockgroda i Ystad kommun, Skåne
347 Samanah Seyedi-Shandiz (2015) Automatic Creation of Schematic Maps - A Case Study of the Railway Network at the Swedish Transport Administration
348 Johanna Andersson (2015) Heat Waves and their Impacts on Outdoor Workers – A Case Study in Northern and Eastern Uganda
349 Jimmie Carpman (2015) Spatially varying parameters in observed new particle formation events
350 Mihaela – Mariana Tudoran (2015) Occurrences of insect outbreaks in Sweden in relation to climatic parameters since 1850
351 Maria Gatzouras (2015) Assessment of trampling impact in Icelandic natural areas in experimental plots with focus on image analysis of digital photographs
352 Gustav Wallner (2015) Estimating and evaluating GPP in the Sahel using MSG/SEVIRI and MODIS satellite data
353 Luisa Teixeira (2015) Exploring the relationships between biodiversity and benthic habitat in the Primeiras and Segundas Protected Area, Mozambique
354 Iris Behrens & Linn Gardell (2015) Water quality in Apac-, Mbale- & Lira district, Uganda - A field study evaluating problems and suitable solutions
355 Viktoria Björklund (2015) Water quality in rivers affected by urbanization: A Case Study in Minas Gerais, Brazil
356 Tara Mellquist (2015) Hållbar dagvattenhantering i Stockholms stad - En

riskhanteringsanalys med avseende på långsiktig hållbarhet av Stockholms stads
dagvattenhantering i urban miljö

357 Jenny Hansson (2015) Trafikrelaterade luftföroreningar vid förskolor – En studie om kvävedioxidhalter vid förskolor i Malmö

358 Laura Reinelt (2015) Modelling vegetation dynamics and carbon fluxes in a high Arctic mire

359 Emelie Linnéa Graham (2015) Atmospheric reactivity of cyclic ethers of relevance to biofuel combustion

360 Filippo Gualla (2015) Sun position and PV panels: a model to determine the best orientation

361 Joakim Lindberg (2015) Locating potential flood areas in an urban environment using remote sensing and GIS, case study Lund, Sweden

362 Georgios-Konstantinos Lagkas (2015) Analysis of NDVI variation and snowmelt around Zackenberg station, Greenland with comparison of ground data and remote sensing.

363 Carlos Arellano (2015) Production and Biodegradability of Dissolved Organic Carbon from Different Litter Sources

364 Sofia Valentin (2015) Do-It-Yourself Helium Balloon Aerial Photography - Developing a method in an agroforestry plantation, Lao PDR

365 Shirin Danehpash (2015) Evaluation of Standards and Techniques for Retrieval of Geospatial Raster Data - A study for the ICOS Carbon Portal

366 Linnea Jonsson (2015) Evaluation of pixel based and object based classification methods for land cover mapping with high spatial resolution satellite imagery, in the Amazonas, Brazil.

367 Johan Westin (2015) Quantification of a continuous-cover forest in Sweden using remote sensing techniques

368 Dahlia Mudzaffar Ali (2015) Quantifying Terrain Factor Using GIS Applications for
Real Estate Property Valuation

369 Ulrika Belsing (2015)The survival of moth larvae feeding on different plant species in northern Fennoscandia

370 Isabella Grönfeldt (2015) Snow and sea ice temperature profiles from satellite data and ice mass balance buoys